

Computational Intelligence for Abdominal Aortic Aneurysm Imaging Analysis

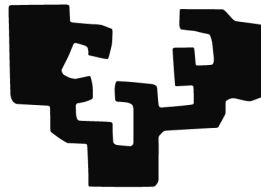
By

Josu Maiora Oria

<http://www.ehu.es/ccwintco>

Dissertation presented to the Department of Computer Science and Artificial Intelligence
in partial fulfillment of the requirements for the degree of

Doctor of Philosophy



PhD Advisor:

Prof. Manuel Graña Romay

At

The University of the Basque Country
Donostia - San Sebastián
2012

Dedication, cite from a famous person, or whatever you like (optional)

**AUTORIZACION DEL/LA DIRECTOR/A DE TESIS
PARA SU PRESENTACION**

Dr/a. _____ con N.I.F. _____

como Director/a de la Tesis Doctoral: _____

realizada en el Departamento _____

por el Doctorando Don/ña. _____ ,

autorizo la presentación de la citada Tesis Doctoral, dado que reúne las condiciones necesarias para su defensa.

En _____ a _____ de _____ de _____

EL/LA DIRECTOR/A DE LA TESIS

Fdo.: _____

CONFORMIDAD DEL DEPARTAMENTO

El Consejo del Departamento de _____

en reunión celebrada el día ____ de _____ de ____ ha acordado dar la
conformidad a la admisión a trámite de presentación de la Tesis Doctoral titulada: _____

dirigida por el/la Dr/a. _____

y presentada por Don/ña. _____

ante este Departamento.

En _____ a ____ de _____ de ____

Vº Bº DIRECTOR/A DEL DEPARTAMENTO SECRETARIO/A DEL DEPARTAMENTO

Fdo.: _____

Fdo.: _____

ACTA DE GRADO DE DOCTOR
ACTA DE DEFENSA DE TESIS DOCTORAL

DOCTORANDO DON/ÑA. _____

TITULO DE LA TESIS: _____

El Tribunal designado por la Subcomisión de Doctorado de la UPV/EHU para calificar la Tesis Doctoral arriba indicada y reunido en el día de la fecha, una vez efectuada la defensa por el doctorando y contestadas las objeciones y/o sugerencias que se le han formulado, ha otorgado por _____ la calificación de:

unanimidad ó mayoría

Idioma/s defensa: _____

En _____ a _____ de _____ de _____

EL/LA PRESIDENTE/A,

EL/LA SECRETARIO/A,

Fdo.:

Fdo.:

Dr/a: _____

Dr/a: _____

VOCAL 1º,

VOCAL 2º,

VOCAL 3º,

Fdo.:

Fdo.:

Fdo.:

Dr/a: _____ Dr/a: _____ Dr/a: _____

EL/LA DOCTORANDO/A,

Fdo.: _____

Contents

Nomenclature	1
1. Introduction	3
1.1. Introduction and motivation	3
1.2. General description of the contents of the Thesis	3
1.2.1. Segmentation by Active Learning	5
1.2.2. Registration for visual assessment	6
1.2.3. Computer Aided Diagnosis	7
1.3. Contributions	7
1.4. Publications obtained	8
1.5. Structure of the Thesis	9
2. Medical Background: Abdominal Aortic Aneurysm	11
2.1. Abdominal Aortic Aneurysm and Treatment	11
2.2. Computed Tomography Angiography	12
2.3. Application of CTA to AAA	14
2.3.1. Preoperative Imaging	14
2.3.2. Postoperative Imaging	14
3. Medical Image Visualization for AAA	21
3.1. Introduction	21
3.2. Definitions	22
3.3. Visualization Methods	22
3.3.1. 2-D image generation and display	23
3.3.2. 3-D image generation and display	26
3.4. 3D Vascular Segmentation	29
3.4.1. Thresholding Algorithms	30
3.4.2. Algorithms Based on Pattern Recognition Techniques	31
3.4.3. Algorithms Based on Deformable Models	31
3.5. AAA segmentation	33
3.5.1. Lumen Segmentation	33
3.5.2. Thrombus Segmentation	33
3.6. Discussion	34

4. Machine Learning for Medical Image Analysis	37
4.1. Introduction	37
4.1.1. Learning algorithm categories	38
4.1.2. Classifier models	39
4.1.3. Feature extraction	40
4.1.4. Validation	40
4.1.5. General problem statement	41
4.2. Active Learning	41
4.2.1. Introduction	41
4.2.2. Query Strategy	42
4.2.3. Active Learning Canonical Algorithm	43
4.3. Artificial Neural Networks	44
4.3.1. Neuron Model	44
4.3.2. Perceptron	45
4.3.3. Linear Networks	47
4.3.4. Backpropagation	47
4.3.5. Radial Basis Function	49
4.3.6. Learning Vector Quantization Neural Network	51
4.4. Statistical Classification Algorithms	52
4.4.1. Support Vector Machines (SVM)	52
4.4.2. Logistic Model Tree	53
4.4.3. Random Forest	54
5. Active Learning for Thrombus Segmentation	55
5.1. Introduction	55
5.2. Learning and feature selection	59
5.3. Experimental setup	62
5.4. Experimental Results	64
5.5. Conclusions	66
6. Abdominal Aortic Aneurysm Registration	71
6.1. Introduction	71
6.2. Overview of Registration Algorithms	73
6.2.1. Similarity measures	74
6.2.2. Transformation models	75
6.2.3. Optimization	77
6.3. Aorta's Lumen Registration	79
6.4. Thrombus co-registration	79
6.5. Conclusions	80
7. Computer Aided Diagnosis	87
7.1. Endovascular Repair	87
7.2. Computer Aided Diagnosis systems	88

7.3. Computational pipeline	89
7.3.1. Lumen Segmentation	89
7.3.2. Quantification of Abdominal Aortic Deformation after EVAR	90
7.3.3. Learning Algorithms	91
7.4. Results	93
7.4.1. Datasets	93
7.5. Conclusions	94
8. Conclusions and Future works	99
8.1. Conclusions	99
8.2. Future works	100
A. Computer Tomography Datasets	101
A.1. Hospital Donostia Dataset	101
A.1.1. 16-row CT scanner	101
A.1.2. 64-row CT scanner	101
A.2. Mount Sinai School of Medicine (New York) Datasets	102
B. Insight Toolkit Software	107
B.1. Introduction	107
B.2. Configuring ITK	107
B.3. ITK Modules	108
B.3.1. Data representation	108
B.3.2. Filters	108
B.3.3. Reading and Writing Images	111
B.3.4. Segmentation Methods	111
B.3.5. Registration Framework	113
B.4. Process Pipeline	115
Bibliography	117
Bibliography	117

Nomenclature

AAA	Abdominal Aortic Aneurysm
AAA	Abdominal Aortic Aneurysm
AAA	Abodminal Aaorta's Aneurysm
BP	Backpropagation
CAD	Computer Aided Diagnosis
CT	Computed Tomography
CT	Computerized Tomography
CTA	Computed Tomography Angiography
CTA	Computed Tomography Angiography
EVAR	EndoVascular prostheses for Aneurysm Repair
EVAR	Endovascular Aneurysm Repair
FFD	Free From Deformations
LMT	Logistic Model Tree
LVQ	Learning Vector Quantization
MI	Mutual Information
MIP	Maximum Intensity Projection
MLP	Multi-Layer Perceptron
MRI	Magnetic Resonance Imaging
MSD	Mean Squared Differences
PET	Positron Emission Tomography
RBF	Radial Basis Function
RF	Random Forest
SVM	Support Vector Machine

1. Introduction

This introductory chapter is aimed to provide a quick overlook of the thesis that may allow the casual reader to assess its contents and main contributions. Its structure is as follows: Section section 1.1 gives some general guidelines and motivation of the Thesis contents. Section section 1.2 gives a general description of the Thesis contents. Section section 1.3 summarizes the main contributions of the Thesis. Section section 1.4 enumerates the publications obtained along the works. Section section 1.5 describes the actual contents of the chapters in the Thesis.

1.1. Introduction and motivation

The main material on which this Thesis works are Computed Tomography (CT) abdominal images, specifically Computed Tomography Angiography (CTA) of patients of Abdominal Aortic Aneurysms (AAA) which underwent Endovascular Aneurysm Repair (EVAR). It is expected of the deployment of CT imaging devices to improve our ability for detecting and monitoring anatomical structures in the body, as well as tracking their evolution in time. However, these kind of images pose new kinds of challenges.

This Thesis has grown along two main lines of work. First, the idea of predicting the evolution of patients who underwent EVAR according to aortic deformation values measured by image registration techniques. Prediction has to be achieved by Machine Learning approaches. Second, the segmentation of challenging structures in the images (3D CTA) applying an Active Learning approach in the training of classifiers performing the voxel-based classification achieving the segmentation. Some of the works in this Thesis have been done in close relation with the clinicians in actual treatment of AAA patients, so that some of the contents of the Thesis are directly aimed to provide them with useful tools for their daily work.

1.2. General description of the contents of the Thesis

The pipeline of processes implemented in the Thesis is shown in Figure Figure 1.1. The starting point is the CTA data provided by the clinicians from conveniently anonymized databases. Major goals of the work done in this Thesis are highlighted

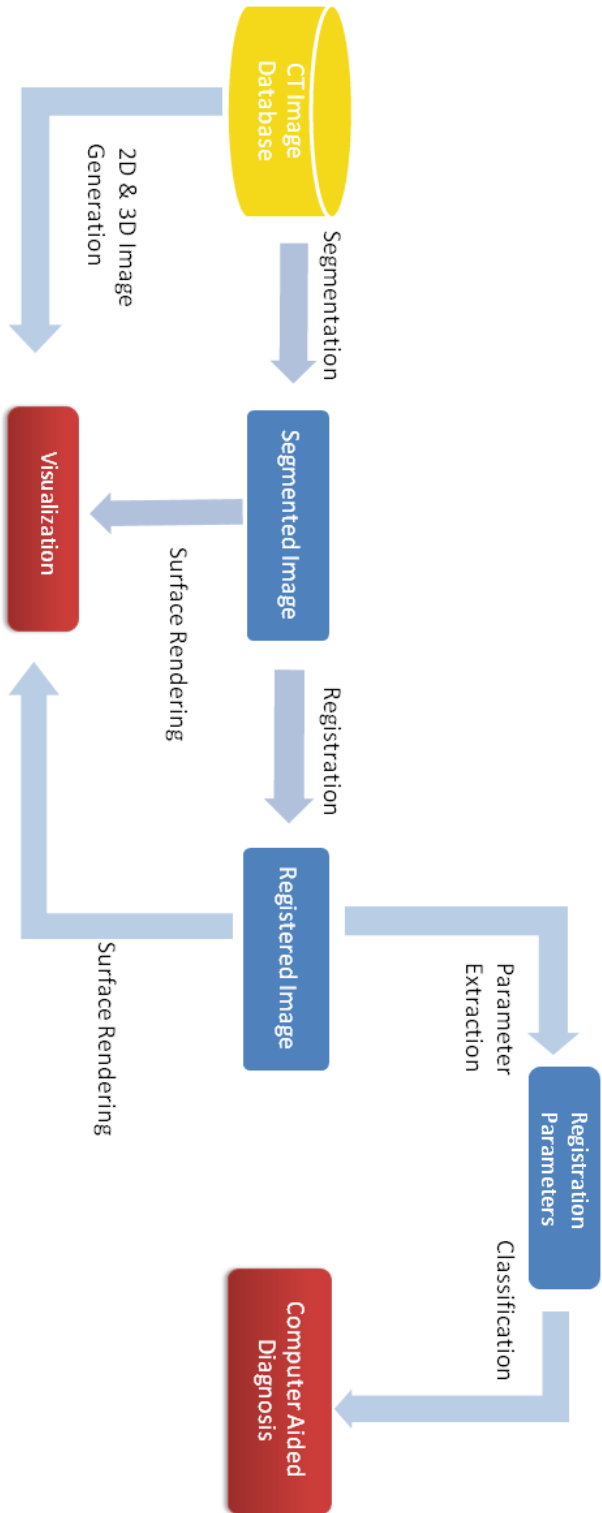


Figure 1.1.: Pipeline of the processes involved in the works performed in this Thesis

in red boxes: Visualization and Computer Aided Diagnosis. Visualization is a requirement for the human assessment of the patient's state and evolution. The goal is to provide the clinicians with a visualization procedure that highlights the required information. In this case is the evolution of the AAA's thrombus. Computer Aided Diagnosis (CAD) goal is to provide predictions about patient's state on the basis of image information. In this case, the prognosis of the patient. CAD is done on the basis of the registration parameters which can be also used for visualization. Thus, the central processes in this pipeline are the segmentation and registration of the patient's imaging data. Volume registration is performed using the first study of a patient as the reference image, and the other taken as the moving image, so that the deformation and movement introduced by the evolution of the AAA thrombus, stent graft and aortic lumen are computed in a longitudinal analysis.

1.2.1. Segmentation by Active Learning

Segmentation of AAA thrombus and lumen in the CTA volume image has been proposed following diverse approaches, as will be commented in Chapters 3 and 5, requiring diverse degrees of interaction and human operator feedback. Some attempts have been reported applying adaptive region growing and deformable surface matching approaches, which require usually good initial guesses to achieve good results, and some careful algorithm design because of the very low contrast-to-noise ratio of some features of AAA volumetric CTA data. Parameter tuning and validation of all segmentation processes is conditioned to the availability of data samples, which must be representative of all possible situations in order to assess the generalization of the segmentation method to new data. CTA data may have strong variability due to several causes: (a) different CT imaging devices, either from the hardware or the software point of views, (b) variations in anatomical localization due to inter and intra-subject variability, (c) low contrast-to-noise ratio due to similarity of tissue absorption patterns in neighboring organs of the abdomen, (d) miscellaneous noise sources such as capture and computational additive noise and patient motion, (e) functional/physiological variations, such as diverse flow patterns of the contrast agent. To cope with such variability we are forced either to retrain the existing segmentation process or to start afresh the segmentation design following some optimized design strategy. In this Thesis we have opted for the second approach applying an Active Learning strategy to train specific classifiers for the detection of the target anatomical structures.

Active Learning is an interactive train data selection and labeling algorithm that uses the actual classification uncertainty to guide the selection of new training data to be labeled by an oracle, usually the human operator. Active Learning minimizes the number of data samples needed to build up a classifier maximizing its generalization performance by selection of the data samples with maximal uncertainty. The intuitive rationale is that maxim. On this basis, the segmentation procedure consists in the following steps:

1. Computation of the selected features from the data set given by the CTA 3D image data.
2. Create a random selection of candidate voxels for the train dataset. Ask the oracle for their class labeling.
3. Iterating the following steps, until reaching a desired accuracy performance.
 - a) Add the selected set of labeled voxels to the train dataset. The data consist of pairs of feature vectors and corresponding labels. The
 - b) Train the classifier on the train dataset.
 - c) Compute accuracy by suitable crossvalidation procedure. Often it is reduced to leave-one-out if the dataset is too small. In experiments where the ground truth is already available, accuracy can be computed on all samples out of the train dataset.
 - d) Compute the classification uncertainty of the data samples outside the train dataset which are candidates to be added to it.
 - e) Select the candidate data samples with maximal uncertainty asking the oracle for their class labeling.
4. Apply the obtained classifier to the whole CTA 3D image data. In the experimental validation reported in this Thesis, there is a given ground truth, therefore the accuracy on the whole image can be obtained.

This procedure involves some human operator interaction in the clinical setting, however this interaction reduces to picking among the voxels with highest classification uncertainty. An appropriate visualization and interface tool would make this process amenable in the real clinical context for accurate measurement of the AAA's thrombus volume.

1.2.2. Registration for visual assessment

The clinicians find very useful tools that allow them to perform visual inspection of the data in such a way that their intuitive assessment of the patient's state and evolution. For the monitoring of AAA patients after EVAR treatment, the visual inspection of the evolution of the thrombus in the aneurysm sac provides a very direct way to perform the desired assessment. The approach followed consists in the rigid registration of the thrombus according to the registration transformation computed on the Aorta's lumen bounded by the stent graft. Segmentation of the lumen and stent graft usually does not pose problems. Moreover, when the stent graft is stable, the shape of the lumen will not vary, so that the rigid registration of the segmented lumen between the initial and subsequent imaging studies is within the scope of conventional registration software. The complete procedure is as follows:

- Segment aortic lumen in CTA volumes obtaining the fixed (initial EVAR imaging study) and moving (imaging study after some time) binary 3D images for registration.
- Compute rigid registration of the lumen region.
- Apply the rigid registration transformation to the lumen and segmented thrombus of the moving study.
- Visualize the overlapping of the two thrombus regions.

The restriction of the registration transformation to the rigid body case arises from the fact that we do not want to introduce false deformations of the thrombus that may misguide the clinician's assessment. The presentation of the results to the clinicians has been encouraging.

1.2.3. Computer Aided Diagnosis

Aiming to offer a complementary tool supporting the clinician assessment, we look to the application of Machine Learning approaches to provide some CAD system for AAA prognosis based on imaging information. The features considered for the characterization of the AAA state are the parameters of the registration performed to match the thrombus in the moving CTA data to the thrombus in fixed CTA data. Now, the registration includes affine and non-linear transformations, because we want to build the CAD system on the quantitative measurement of the deformations suffered by the thrombus along time. To reduce the feature dimensionality, we use as features the registration quality measures instead of the transformation parameters. The procedure for feature extraction proceeds by successive registration refinements, from the rigid body, affine registration, up to a two level diffeomorphic registration using B-splines to model the deformation field. The registration quality measures are input to a Machine Learning algorithm learning the prognosis prediction from the actual diagnosis provided by the clinicians. The validation of the approach reported includes several state-of-the-art algorithms for classifier training on the available clinical data (conveniently anonymized). Results have been positive, reaching high accuracy in a leave-one-out validation process. However the small sample size asks for an extended recruitment of patients and data to perform extensive validation of the approach.

1.3. Contributions

The specific contributions of the Thesis are the following ones:

- A state-of-the-art review covering diverse topics tackled in the Thesis, such as AAA segmentation, imaging and visualization techniques, image registration, and Machine Learning for medical image analysis.

- Definition of a feature selection procedure for Random Forests based on the sensitivity of the out-of-bag error as a measure of feature importance. This procedure has been applied to the selection of the voxels' features for the CTA image segmentation.
- Definition of an Active Learning strategy based on the variance of the individual classifier Random Forest outputs as a measure of classification uncertainty. This strategy has been applied to CTA image segmentation of the AAA's thrombus.
- Experimental validation of the Active Learning strategy for training classifiers to perform AAA's thrombus segmentation.
- Definition of a visualization pipeline for the visual assessment of AAA's thrombus evolution, avoiding artifacts due to image registration.
- Definition of the feature extraction for a CAD system devoted to EVAR prognosis. Features are based on the successive steps of a registration pipeline, specifically they are the registration quality measures.
- Validation of the CAD systems on clinical CTA datasets provided by the clinicians, testing several state-of-the-art supervised classifier training algorithms.

1.4. Publications obtained

1. J. Maiora, B. Ayerdi, M. Graña, «Random Forest Active Learning for Computed Tomography Angiography Image Segmentation» Neurocomputing, 2012 (in press)
2. D. Chyzhyk, M. Graña, A. Savio, J. Maiora, «Hybrid Dendritic Computing with Kernel-LICA applied to Alzheimer's Disease detection in MRI», Neurocomputing, 2012, Volume 75, issue 1, pp. 72-77.
3. G. García, J. Maiora A. Tapia, M. De Blas, «Evaluation of Texture for Classification of Abdominal Aortic Aneurysm After Endovascular Repair», Journal of Digital Imaging, Volumen 25, issue 3, pp. 369-376, 2012.
4. J. Maiora, M. Graña, «A computer aided diagnostic system for survival analysis after EVAR treatment», Journal of Medical Informatics & Technologies, Volume 18, pp. 51-58, 2011.
5. I. Macia; M. Graña; J. Maiora; C. Paloc; M. de Blas, «Detection of Type II Endoleaks in Abdominal Aortic Aneurysms After Endovascular Repair», Computers in Biology and Medicine, Volume 41, issue 10, pp. 871-880, 2011.
6. J. Maiora, G. Garcia, A. Tapia, I. Macia, J.H. Legarreta, C. Paloc, M. De Blas, M. Graña «Thrombus Change Detection After Endovascular Abdominal Aortic Aneurysm Repair», International Journal of Computer Assisted Radiology and Surgery, Springer-Verlag, Volume 5 (Suppl 1), pp. S15, 2010.

7. J. Maiora, M. Graña, «Abdominal CTA Image Analysis Through Active Learning and Decision Random Forests: Application to AAA Segmentation», IJCNN 2012, Brisbane, Australia.
8. J. Maiora, M. Graña, «A Hybrid Segmentation of Abdominal CT Images», 7th International Conference on Hybrid Artificial Intelligence Systems. Special session on Hybrid Computational Intelligence and Lattice Computing for Image and Signal Processing. Salamanca, Spain. March 28-30, 2012.
9. J. Maiora, G. García, M. Graña, M. De Blas, J. Sanchez, «Classification of Patients after Endovascular Repair Based on Image Registration Quality Measures», MICCAI-CVII 2011, Toronto, Canada, 18-22, Sept 2011.
10. J. Maiora, M. Graña. «A hybrid system for survival analysis after EVAR treatment of AAA», Hybrid Artificial Intelligence Systems, 6th International Conference (HAIS), Wroclaw, Poland, 2011.
11. J. Maiora, G. García, I. Macía, J. Hartz-Legarreta, F. Boto, C. Paloc, M. Graña and J. Sanchez Abuín, «Thrombus Volume Change Visualization after Endovascular Abdominal Aortic Aneurysm Repair», Hybrid Artificial Intelligence Systems, 6th International Conference (HAIS), San Sebastian, 2010.
12. J. H. Legarreta, F. Boto, I. Macía, J. Maiora, G. García, C. Paloc, M. Graña and M. de Blas, «Hybrid Decision Support System for Endovascular Aortic Aneurysm Repair Follow-up», Hybrid Artificial Intelligence Systems, 6th International Conference (HAIS), San Sebastian, 2010.
13. J. Maiora, G. Garcia, M. Grana, I. Macia, J.H. Legarreta, C. Paloc, M. De Blas, «Thrombus change detection after endovascular abdominal aortic aneurysm repair», CARS 2010 Computer Assisted Radiology and Surgery, Geneva, Switzerland, 2010.
14. I. Macía, J.H. Legarreta, C. Paloc, M. Graña, J. Maiora, G. García, «Segmentation of Abdominal Aortic Aneurysms in CT Images using a Radial Model Approach», IDEAL 2009, Burgos, 2009.
15. J. Maiora, G. García, A. Tapia, I. Macía, J. H. Legarreta, M. Graña, «Stent Graft Change Detection after Endovascular Abdominal Aortic Aneurysm Repair», IDEAL 2009, Burgos, 2009.

1.5. Structure of the Thesis

The Contents of the Thesis is the following:

- Chapter 2 reviews the medical background of the Abdominal Aortic Aneurysm (AAA), including some description of the gold standard medical imaging device employed for patient examination and monitoring.

- Chapter 3 reviews the medical image processing background, with some emphasis in the algorithms employed for the segmentation of AAA's structures.
- Chapter 4 reviews Machine Learning methods with an emphasis on their application to the medical image data, either at the level of image segmentation or clinical assistance based on global image classification.
- Chapter 5 contains the first main contribution of the Thesis consisting in the application of Active Learning to the segmentation of thrombus in AAA volumes. The chapter explains the approach and provides empirical results on real life data.
- Chapter 6 contains the second contribution of the Thesis, consisting in the application of registration methods for the visualization of the AAA's thrombus evolution in clinical application. The method has been tested on real clinical data.
- Chapter 7 contains the last contribution of the Thesis, consisting in the application of Machine Learning for the development of Computer Aided Diagnosis system for the prognosis of the evolution of the treatment of the AAA.
- Chapter 8 contains the conclusions of the Thesis and some lines of future research.
- Appendix A comments on the datasets used for the experiments along the Thesis, provided by medical teams from Hospital Donostia and Mount Sinai School of Medicine.
- Appendix B comments on the main software tool used for image processing, namely the ITK library.

2. Medical Background: Abdominal Aortic Aneurysm

This chapter is aimed to set the stage for the Thesis from the medical point of view, describing the main problem addressed in the Thesis, and its motivation. Section section 2.1 gives an introduction to the main medical issue: Abdominal Aortic Aneurysm and its endovascular repair. Section section 2.2 introduces Computed Tomography Angiography (CTA). Section section 2.3 comments on its application to this medical issue.

2.1. Abdominal Aortic Aneurysm and Treatment

An aneurysm is a focal dilation of a blood vessel to more than twice its normal diameter. Aneurysms are most commonly found in large arteries (aorta, iliac, and femoral); however, they have been reported in smaller arteries such as the radial or coronary arteries as well. The etiology of aneurysm is currently believed to be multifactorial with atherosclerosis contributing the greatest part to the disease process. Other causes may include infectious etiologies, traumatic injury, chronic lung diseases, genetic disorders, smoking, and biomechanical factors such as hypertension, disturbed blood flow, and wall tissue degradation. The prevalence of aneurysms is greatest in the infra-renal abdominal aorta.

Abdominal Aortic Aneurysm (AAA) [80] is a dilation of the aorta that occurs between the renal and iliac arteries due to weakening of the vessel wall. The weakening of the aortic wall leads to its deformation and the generation of a thrombus. If the aneurysm gets too big, it can break. If left untreated, nearly all aneurysms continue to enlarge and eventually rupture. Aneurysms with a diameter of 5 cm or greater should be treated. The rupture of an aneurysm can have very serious consequences and even cause death. Figure

Treatment options involve replacement of the diseased artery segment with a synthetic tube and, until this past decade, were solely performed with standard open surgical technique, which is considered to be a major intervention with significant risk to the patient. In the early 90s there was a breakthrough in the treatment of AAA with the implantation of the Endovascular Aneurysm Repair (EVAR) [127]. Nowadays, EVAR is one of the most popular treatments against AAA because it is

a minimally invasive procedure to remove the aneurysm from the blood flow. Compared with traditional surgery, a stent graft is deployed in the interior of the aorta using a catheter system that is introduced through the femoral arteries (see Figure 2.2). After the stent graft implantation, it becomes the Aorta's lumen in the aneurysm section of the Aorta, supporting all blood flow and pressure. Outside the stent graft a thrombus develops in the aneurysm sac, that can disappear if reabsorbed by the body. Despite the success of the technique, in a number of occasions it is preferable traditional open surgery of AAA[143].

EVAR risks A major problem after EVAR is migration [70]of the stent graft, which may involve a twisting or buckling. This can lead to leaks and or fatigue of the material of the prosthesis, leading to progressive aneurysm complications [44].

Incomplete exclusion of the aneurysms from the blood flow results in endoleaks: the leakage of blood around the stent graft entering the thrombosed aneurysm sac. The endoleaks may cause continued pressurization of the sac which again increases the risk of Aorta rupture. In addition to leakage and fatigue of the material of the prosthesis, their migration can cause blockages in their legs that have to be treated by femoral bypasses. It requires post-treatment follow-up to ensure that the stent is stable (no leaks). A decrease in aneurysm size indicates that the exclusion of the Aorta's wall from the blood flow has been effective, while an expansion after deployment is indicative of the presence of a leak in the stent, and the existence of risk of rupture.

To prevent future risk after the EVAR and to assess the response of the aneurysm to the implant of the stent graft, the patient needs to be monitored imaging the abdominal region along the follow-up period. The acquired images help physicians to get information about the aneurysm and the stent graft. Based on the segmentation of aortic inner and outer boundary, that is, lumen and thrombus boundary, it is possible to reconstruct and visualize the 3D AAA model allowing to assess the displacement and deformation of the stent graft and to measure the aneurysm's size.

2.2. Computed Tomography Angiography

Computed Tomography (CT), a modality for non-invasive medical imaging has been established as the gold standard in many areas. Computed Tomography (CT) is a further development of the traditional X-ray technique. It is a medical imaging method employing tomography to generate a large series of cross-sectional images of the body. Though the CT slice is a two-dimensional (2D) image, using image processing, anatomical structures can be segmented and three-dimensional (3D) rendering can be created, which enhances the visual information of planar images and give physicians anatomical information of the region of interest .

Early CT scanners could only acquire images as a single axial slice at a time (sequential scanning). Later, several generations of scanners have been developed. Spiral CT scanners enable the X-ray tube to rotate continuously in one direction around the patient. Multi-slice CT machines (now up to 64-slice) utilize the principle of the spiral scanner and incorporate multiple rows of detector rings. The latest generation of CT scanner is Dual Source CT scanners, which were introduced in 2005. They allow higher temporal and spatial resolution, therefore reducing motion blurring at high heart rates and potentially requiring a shorter breath-hold time.

Volumetric data acquired by the modern CT scanner can be reconstructed to suit most clinical requirements. The data can be reformatted in various planes which is called multiplanar reformatting (MPR). We can get sagittal, coronal and oblique plane views along with the standard transaxial plane. The stack of 2D slices can also be reconstructed as volumetric (3D) representations of structures for a better anatomical view. Contrast between different tissues of the body can be improved by the use of different contrast agents. These contrast agents are used to highlight specific areas so that the organs, blood vessels, or tissues are more visible. Figure 2.3 highlights the differences in contrast due to the use of a blood contrast. Contrast-enhanced Computed Tomography Angiography (CTA) is the most widely used medical imaging technology for getting exact knowledge of the position, shape, size of an aneurysm and the occurrence of endoleaks.

Hounsfield Unit (HU) is a unit to describe the amount of X-ray attenuation of each voxel in the CT image. The reading in Hounsfield Unit is also called the CT number. It is obtained by scaling and calibrating the original value to the intensity value of water (equation Equation 2.1) and named after Godfrey Hounsfield, who demonstrated the first CT scanner in 1972.

$$H = 1000 \frac{(u - u_{water})}{u_{water}} \quad (2.1)$$

This scale assigns water as a standard attenuation value of zero HU. The range of CT numbers is usually 2000 HU wide and some modern scanners have a greater range of up to 4000 HU. Each number represents a shade of gray with +1000 (white) and -1000 (black) at either end of the spectrum (figure Figure 2.4).

Since the human eye can only distinguish less than 80 different gray scale values, it is not possible to display all possible density values in perceptible shades of gray. In order to allow the observer to interpret the image, only a narrow range of HU values are displayed. This is done by a process called windowing. To set a proper window, a center gray scale value and the window width have to be defined. The window is usually centered over average HU values of a particular structure to be studied. Afterwards the window width has to be set, which covers the HU of all the tissues of interest. Tissues with CT values in this range should be distinguishable by varying gray scale values. CT values outside this range are displayed either black or white.

2.3. Application of CTA to AAA

High quality imaging is mandatory for both selection of appropriate candidates for EVAR and follow-up after EVAR. The endovascular devices currently available require the assessment of several anatomical features of an abdominal aortic aneurysm prior to endoluminal repair.

In most centers, spiral CTA has become the gold standard for preoperative imaging for EVAR [15] [56]. High quality preoperative imaging is essential for patient selection, stent graft sizing and planning. Employing the single breath-hold technique to avoid respiratory artifact optimizes the image quality, patients are asked to hold their breath during scanning for as long as possible. Most patients will be able to do this for approximately 30 seconds. By that time, the aortic bifurcation will have been reached. Modern multi-slice helical CT scanners will be able to cover the entire abdomen within 25 seconds, reducing motion artifacts even further [144]. Such scans of the patient's abdomen are available in clinical routine as a set of 2D images, as shown in Figure Figure 2.5. An additional advantage of multi-slice scanners is that the thickness of the slices is smaller and the voxel size becomes more isotropic. This will not only increase the effective in-plane resolution because of a smaller partial volume effect, but the resolution of reconstructed planes will also improve dramatically compared with the resolution in normal spiral CTA.

2.3.1. Preoperative Imaging

In order to evaluate a patient for suitability for EVAR, it is essential to measure the diameter and length of the infra-renal aortic neck and both common iliac arteries. CTA provides adequate tissue contrast by which lumen, mural thrombus and aortic wall can be easily distinguished. These qualities, in combination with image post-processing, provide the basis for accurate measurements. Furthermore, it is important to depict the amount of thrombus and calcium in the infra-renal neck, common iliac arteries and external iliac arteries. For stent graft sizing, aortic length and diameter are needed. Depending on these measurements, the right configuration (supra-renal, aorto-iliac or bifurcated) of stent graft can be chosen. The last step in preoperative imaging is planning the intervention. In most abdominal aneurysms, the aorta is elongated and tortuous. This may result in a more difficult introduction through one of the iliac systems or in a complicated stent graft delivery owing to a very angulated infra-renal neck [22].

2.3.2. Postoperative Imaging

Follow-up after EVAR is an important part of patient care. After EVAR patients need to be monitored for life because the long-term durability and outcome of this treatment are still unknown[69, 70]. In most clinical centers, CTA is currently used

for the follow-up of patients after EVAR[56]. Endoleak detection, change in size of the aneurysmal sac, size and type of endoleak, stent graft migration and deformation are the most important aspects of the EVAR follow-up [195, 196, 184]. To this end, we can perform the monitor the evolution of the EVAR in two different ways:

1. Analysis of the density of the material inside the aneurysm sac. We study the different transformations within the aneurysmal sac by analyzing changes in gray levels or texture. Previously we should segment the aneurysm. By post processing imaging methods multiple CT scans are studied for quantitative assessment of temporal intensity profiles for further analysis of trends in behavior and classification [115]. The steps that are required are the spatial and intensity normalization and partial volume filtering. The spatial normalization corrects variations in patient positioning and distortion artifacts by algorithms for rigid and nonrigid registration. Normalization of intensities includes separate stages for correcting variations in intra and inter-scanners. Partial volume filtering is used to correct artifacts due to variations in patient positioning.
2. Motion analysis of the stent. Several strategies are studied to quantify the migration [112] and deformation [113] with the objective of evaluating the risk associated with these movements and especially to characterize the occurrence of complications. Rigid motion of the stent and the aorta in relation to the spinal cord is estimated. These data allow us to identify patterns for a high probability of dangerous progression of the aneurysm. This way we can make a prediction about future complications and the progression of the disease. Because the processes are complex and data from medical devices are difficult to assess visually, it requires a computer-assisted analysis. Currently, the morphological changes and migration of the stent and the aneurysm after EVAR are not systematically studied with a quantitative basis that represent the complexity of these movements.

Endoleaks A fundamental problem of endoleak classification on CTA images is that they provide instantaneous information, so that classification is based solely upon the location of the endoleak. Absolute proof can be obtained only through a dynamic imaging study. An essential part of our follow-up is the tracking of size change by volume measurements of the non-luminal aneurysm sac. Volume measurements have been shown to be more sensitive to size change than are measurements of diameter [180]. These volume measurements are obtained by a process of manual segmentation of the lumen and total aneurysm volume on a separate graphical workstation. Even using the most sophisticated CTA protocols, endoleaks may be missed [183, 182]. There is a significant number of patients with a growing aneurysmal sac after EVAR who do not have a detectable endoleak on CTA or conventional angiography [179]. The evaluation of aneurysmal sac size change, by using diameter or volume measurements, can be difficult on CTA as well. The only moderate amount of soft tissue contrast does not always allow an accurate demarcation of the aneurysmal wall, especially in inflammatory aneurysms. CTA images depict not only the

stent graft and lumen, but also calcium, bone, metal and other signal-intense tissues making introducing artifacts in the segmentation of the thrombus and lumen.

Migration and deformation of the stent graft The EVAR may have complications including internal leakage, torque and displacement of the stent, and imaging may suffer occlusions from limbs. In many cases, these complications are due to migration of the stent, which is often associated with the deformation of the stent. In most cases it can be treated with a second stent or operation.

Clinical studies describe methods to quantify the migration and shape changes [195]. They are based on interactive distance measurement over the visualization in a computer screen, thus they are not very accurate. The migration's translation parameters are roughly extracted, neither rotation nor non-linear deformation parameters are quantified. Other works [61] quantified the movement of a stent using 10 tantalum markers placed on it, using simulation data for reference. However, it is unclear how migration is measured against a fixed reference system using this method.

Quantification of several features of the shape of the aneurysm has been proposed to classify AAA [4, 30]. These features include specific distances and angles. The quality of the interactive extraction of these features by different observers have been used to evaluate CTA scans perpendicular to blood flow [158]. The computer-assisted (semi)automatic extraction of several characteristics have been evaluated before EVAR [102] and after EVAR [174][181]. Analysis of the geometry of the surface of an AAA has been carried out [154]. In addition to computing principal curvature distributions the authors present methods to compute principal strains and changes of curvature that was not subsequently applied to the AAA but to a membrane of an artificial heart valve.

A study [97, 96] investigated the influence of biomechanical factors in the migration of the stent using the modeling of blood flow, interactions of the wall structure and the pressure of the aneurysm sac, together with the modeling of AAA and deformation of the stent. These factors are the geometry of the stent, the material properties, hemodynamic conditions, the morphology of the AAA represented by the AAA neck angle, the angle of the iliac bifurcation, etc. The modeling will help to understand why the the stent begin to migrate. The modeling of the hemodynamics was also used to try to assess the risk of rupture. Other studies have modeled the pulsatile flow in AAA [58].

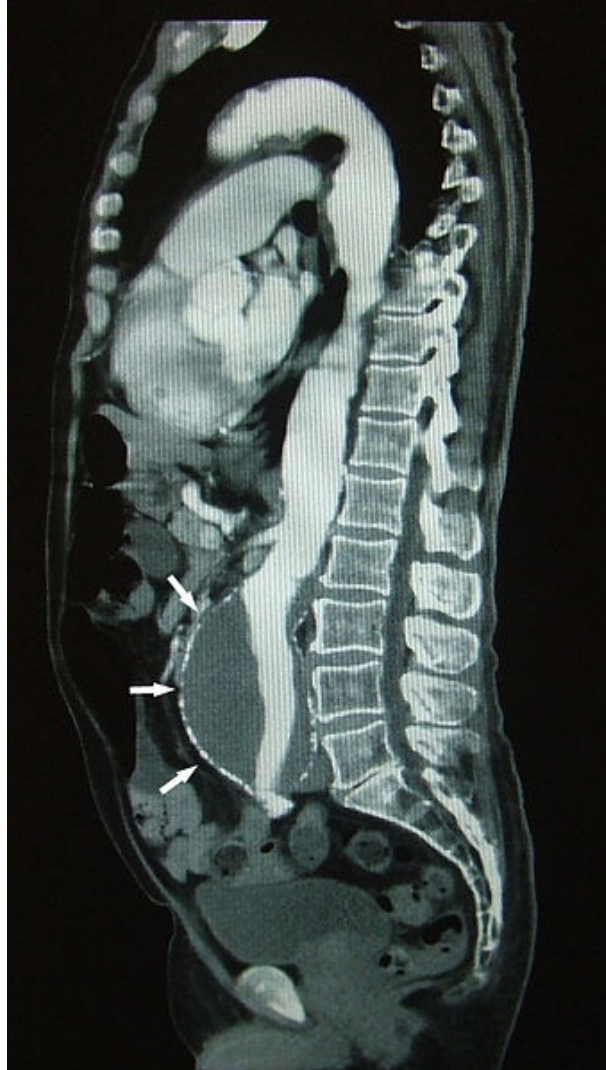


Figure 2.1.: A sagittal cut of the body showing a treated AAA. Arrows indicate the Aorta's wall, the white contrasted blood flowing inside the stent graft placed in the aneurysm section of the Aorta

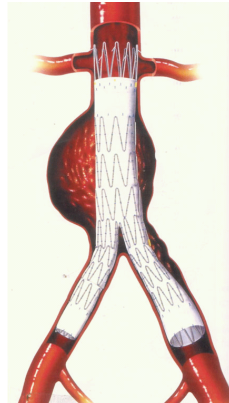


Figure 2.2.: Endovascular Prosthesis

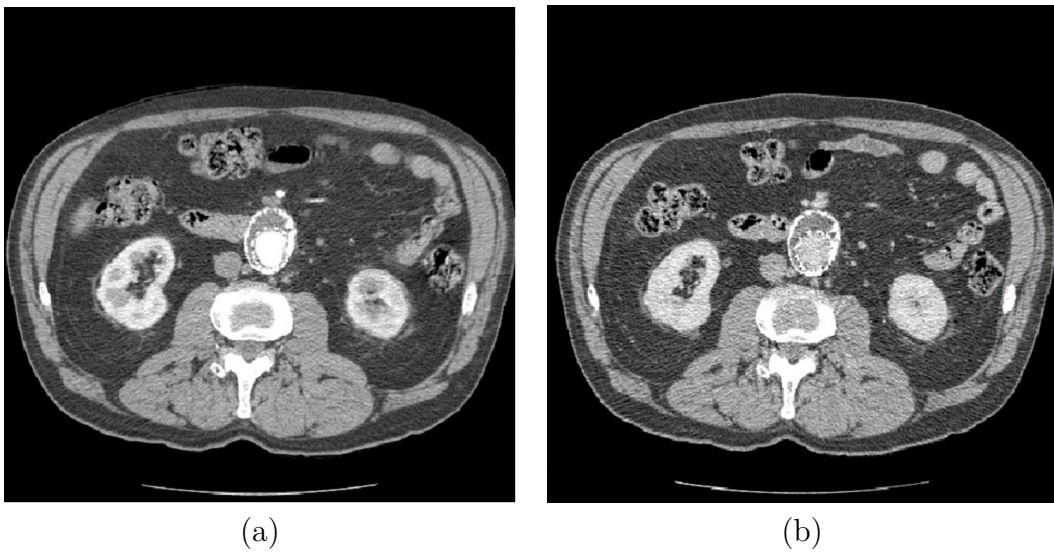


Figure 2.3.: Comparison of vessel intensity values between CT and CTA slice. a) in CTA slice using the contrast agents, blood in lumen is highlighted for a better view. b) in CT slice without using the contrast agent, intensity values of lumen and thrombus are similar.

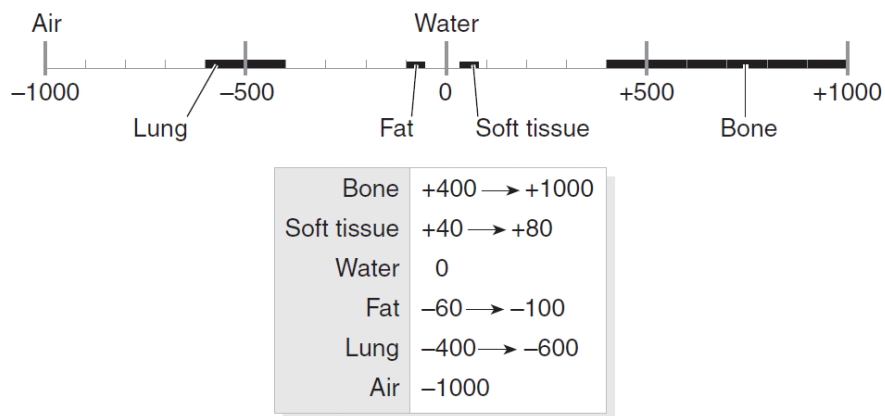


Figure 2.4.: The Hounsfield scale of CT numbers[1]



Figure 2.5.: CT set of images arranged in the traditional manner for monitoring EVAR

3. Medical Image Visualization for AAA

This chapter reviews relevant ideas about medical image processing and visualization, with an emphasis in its application to the Abodminal Aaortic Aneurysm (AAA). Section section 3.1 gives some introductory remarks. Section section 3.2 establishes some definitions for future reference. Section section 3.3 presents common medical image visualization methods, including 2D and 3D conventional methods. Section section 3.4 reviews some common methods used in vascular image segmentation. Section section 3.5 comments specific methods for AAA structures segmentation. Finally, Section section 3.6 gives some discussion of the state of affairs.

3.1. Introduction

An image is a map of some property of an object onto image space. Imaging allows to extract significant information about the objects and their properties from the visualized objects. Techniques to discover this information looking for answers to the mysteries of form and function are in the domain of image processing and visualization. A variety of techniques have been developed to process images in order to enhance the visibility and measurability of desired object features and properties. The challenge of imaging science in biomedical research is to provide advanced capabilities for acquisition, processing, visualization, and quantitative analysis of biomedical images providing faithful displays, interactive manipulation and simulation, accurate, reproducible measurements [14], and extraction any useful information that they contain.

Imaging science has evolved in three distinct fields: segmentation, registration and visualization.

Segmentation is the recognition and delineation of all individual objects in an image scene [121].

Registration methods seek to obtain the transformation that brings different images of the same object(s) into spatial (and/or temporal) congruence.

Visualization provides renderings of the objects enhancing the intuitive understanding of the human operator, and subsequent interations with the imaged objects [201].

3.2. Definitions

3-D medical image visualization: the transformation, presentation of and interaction with multidimensional medical image data sets.

Real time imaging: Processing allowing for on-line refreshment of the data visualization without perceptible artifacts. It is generally accepted to be a rate of 30 frames/s.

Interactive imaging: This refers to sufficiently quick response time of the system after sensing a user action (e.g., mouse movement, key press) providing a corresponding result (e.g., updating the view on the screen) so that the user will perceive (near) instantaneous response to his actions. This generally requires a response/repetition rate of 10 ± 20 frames/s. However, interactivity is application or procedure dependent, i.e., faster response times are needed in highly dynamic situations (e.g. catheter positioning), while and slower response times may be appropriate for more static activity (e.g., tumor delineation in images).

3-D imaging: Refers to acquiring imaging data on a 3D domain, i.e., in x , y , and z dimensions, usually but not necessarily with isotropic spacing (equal separation in all three directions). The term is often generalized to include processing, display and analysis of 3-D data sets.

Multi-modal imaging: The use of different imaging systems (e.g., CT, MRI, PET) to acquire images of the same object (e.g., a patient brain), providing complimentary and more complete information about the object than can be obtained from any single image type (uni-modal). Processing of multi-modal images involves some degree of information fusion.

3-D visualization: Display of 3-D objects so as to effectively represent the 3-D nature of the objects (e.g. shaded graphics). But the term visualization as used in computer imaging also implies the capability to manipulate and analyze the displayed information [48].

Segmentation: It is the partitioning of a dataset into contiguous regions (or sub-volumes) whose member elements (eg. pixels or voxels) have common properties. Segmentation is the procedure by which we impose structure on raw medical image data; we dwell on this structure when visualizing the anatomy or pathology in question as well as plan interventions and treatments to address the medical condition.

3.3. Visualization Methods

For 2-D, three types of multiplanar section projection and display will be described, including orthogonal, oblique planes and curved surfaces. For 3-D, two types of display will be discussed, namely surface renderings and volume renderings (including both projection and surface types) [131].

3.3.1. 2-D image generation and display

The utility of 2-D images often depends on the physical orientation of the image plane with respect to the structure of interest. However, most medical imaging systems are not able to create optimal 2-D image projections directly, because structure positioning and scanner orientation are generally restricted. Consequently, techniques to generate and display arbitrary 2-D images from 3-D volume images are particularly important, allowing a customized optimal orientation of the 2-D image plane showing the important features in the 2-D image of the visualized 3D structure. For example, the measurement of the cross-sectional shape of the aortic arc may be necessary for its functional assessment.

Multiplanar reformatting

3-D isotropic volume images allow for simple and efficient computation of 2D images lying along the non-acquired orthogonal orientations of the volume. This is accomplished by reordering voxels in the volume image, which can be done interactively when the volume image is entirely stored in the computer memory. When the imaged structure is anatomic, the orthogonal planes can be referenced by the anatomic terms for orthogonal orientation: transaxial, coronal, and sagittal. This is demonstrated in figure Figure 3.1 for a 3-D volume image of the torax and abdominal image from a 3-D acquired CT scan. The original plane of acquisition was the transaxial plane, as shown by the transaxial images in the top. The orthogonally reformatted coronal sections from the back towards the front are shown in the middle, with sagittal sections from the right toward the left side shown in the bottom [85]. Implementations of multiplanar reformatting techniques on current computer technology allow the interactive generation and display of these images, such as it is illustrated in figure Figure 3.2.

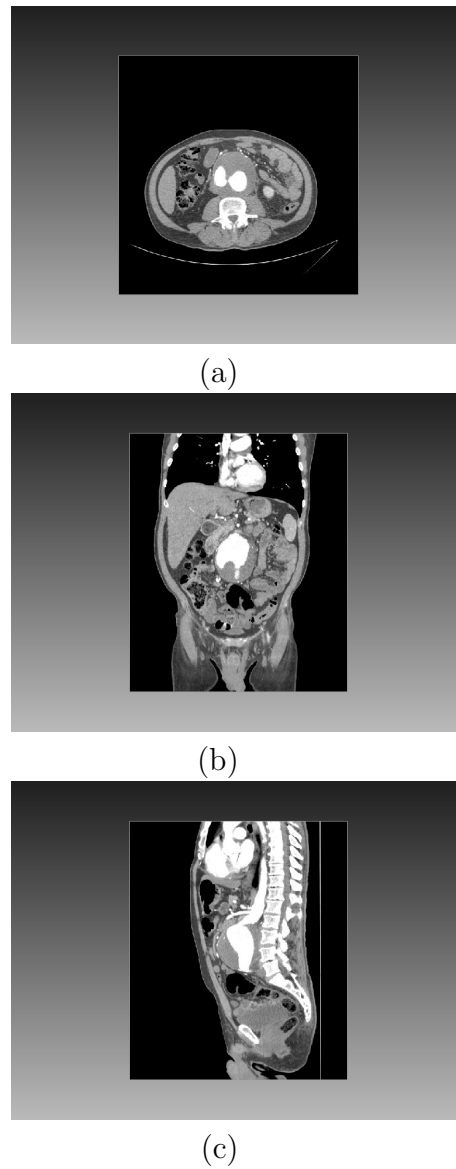


Figure 3.1.: Multiplanar reformatting of a 3-D CT volume image of the torax and abdomen. (a) Image in the original transaxial plane of acquisition. The orthogonally reformatted coronal plane (b) and sagittal plane (c) can be interactively computed and displayed.

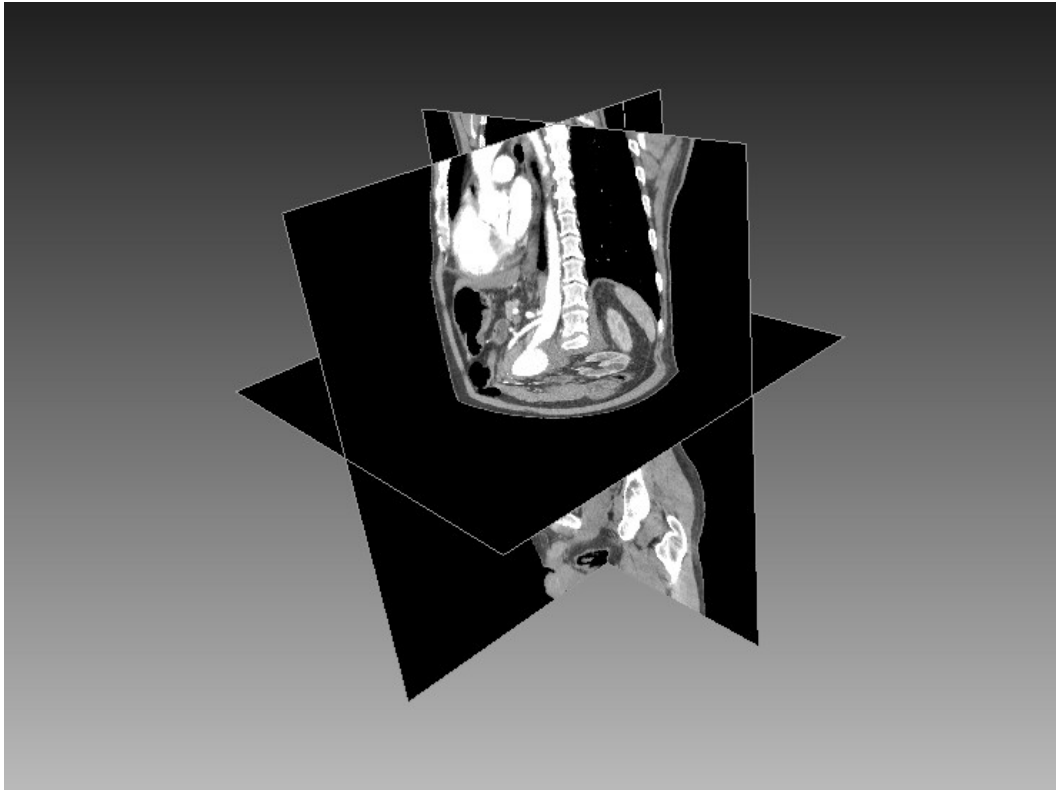


Figure 3.2.: Interactive orthogonal sectioning of a 3-D volume image. Sliders are used to control the interactive orthogonal sectioning.

Oblique projections

The desired 2-D image may not lie along an orthogonal plane of the 3-D volume image, but along an arbitrarily plane oriented at some oblique angle to the orthogonal axes of the volume image domain. Computing oblique projections involve accurate image interpolation and resampling to avoid artifacts due to image resotion.

Curved projections

Often structures of interest may have curvilinear morphology that multi-planar and oblique images cannot capture in a single 2-D image. This shortcoming of planar sections can be overcome using curvilinear projection techniques. This technique is useful for curved structures that remain constant in shape through one orthogonal dimension (one degree of freedom), like the entire extent of the spine in sagittal CT images or curved structures in the orbit of the eye.

3.3.2. 3-D image generation and display

Visualization of 3-D medical images has evolved into two different branches of techniques: surface rendering and volume rendering. Both techniques produce a visualization of selected structures in the 3-D volume image, but the methods involved in these techniques are quite different, and each has its advantages and disadvantages. Selection between these techniques is often conditioned on the particular nature of the biomedical image data, the application of the visualization, and its desired result [68].

Surface rendering

Surface rendering techniques require the extraction of the contours that define the surface of the structure to be visualized. An algorithm is then applied that places surface patches or tiles at each contour point, and the surface is rendered applying hidden surface removal and shading. The advantage of this technique lies in the small amount of contour data needed, resulting in fast rendering speeds. The technique can take advantage of particular graphics hardware to speed the geometric transformation and rendering processes. The contour-based surface descriptions can be transformed into analytical descriptions, which permits use with other geometric visualization packages (i.e., CAD/CAM software), and the contours can be used to drive machinery to create models of the structure. The disadvantages of this technique are largely based on the need to extract the contours defining the structure to be visualized. Any other volume image information is lost in this transformation, breaking the connection back to the original volume information, which may be important for slice generation or feature measurement. This also prohibits any interactive, dynamic determination of the surface to be rendered, as the decision has been made during contour extraction about specific surface will be visualized. Finally, due to the discrete nature of the surface patch placement, this technique is prone to sampling and aliasing artifacts on the rendered surface. Figure 3.3 illustrates surface rendering of the skeleton and vascular system from a thresholded CT scan of the thoracoabdominal region.

Shaded surface displays are useful if there is a need or desire to visualize 3-D surfaces. They are a 2-D representation of a 3-D surface. The 3-D nature of the surface is conveyed with the aid of visual cues such as perspective, shading, texture, shadowing, and stereopsis[81]. Generally, shaded surface displays are not well suited to 'immediate' full visualization of the 3-D volume; that is, they require some preprocessing of the 3-D data to extract the desired surfaces. Shaded surface displays have proven popular in many applications, since, once the surfaces of interest have been determined, it is not difficult to quickly compute images for display.

Modern computational systems can process thousands of polygon patches per second. This speed permits satisfactory interactive capabilities in computer-aided design applications but does not satisfy the requirements of interactive display of

biological/medical images, because a 3-D image of anatomic structures may contain up to hundreds of thousands of faces. Unless the number of faces can be greatly reduced, even state-of-the-art display systems do not really provide acceptable user interaction. Special-purpose graphics hardware can achieve the necessary speed at increased cost.

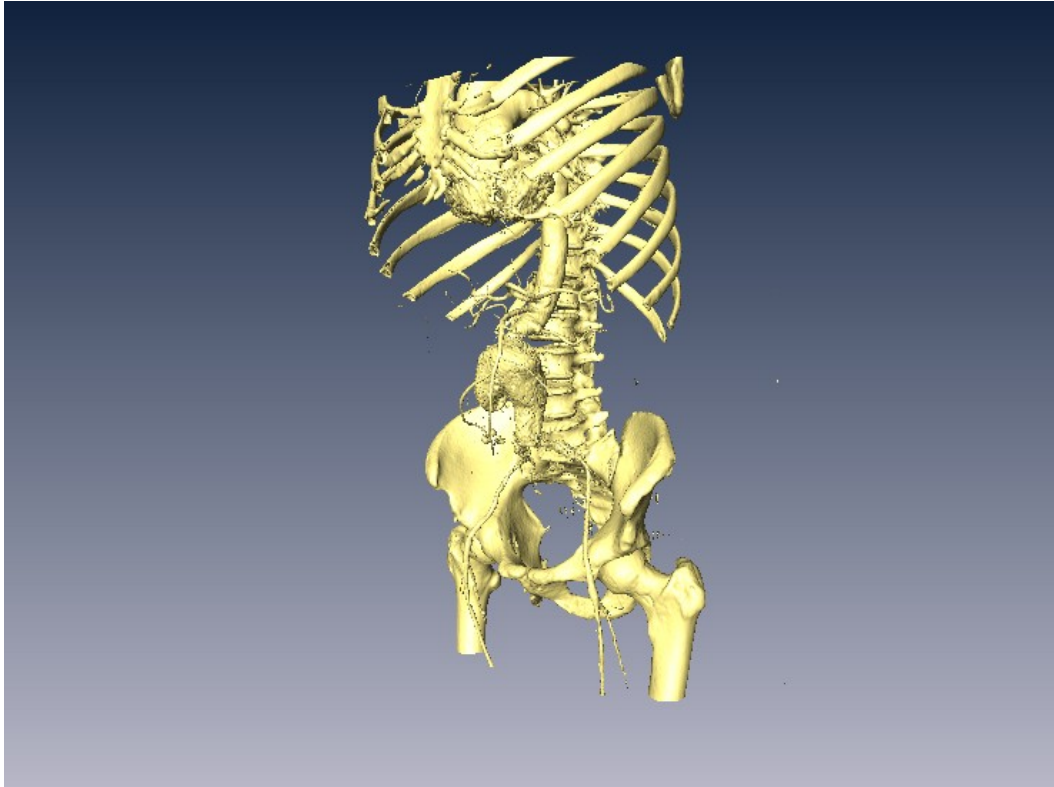


Figure 3.3.: Surface rendering of thoracoabdominal CT slices. Segmentation of skeleton and main vascular structures (aorta and iliac arteries).

Volume rendering

Volume rendering is one of the simplest ways to visualize 3D volumetric scalar data as projections into 2D images by a ray-casting process. The individual values in the dataset are made visible by the choice of a transfer function that maps the data to optical properties, like color and opacity, which are then projected and composited to form an image. An important advantage is that this process displays data directly from the gray scale volume. It produces 'on-the-fly' segmented surfaces, and/or selected degrees of transparency/opacity within the volume [146].

A common visualization goal in volume rendering is the depiction of the interface between two different materials in a volume dataset. The material surface can usually be seen with a simple transfer function which assigns opacity only to a narrow range

of values between the data values associated with each of the two materials[193]. An example of several of these capabilities for interactive transformation and volume rendering of 3-D biomedical image data is illustrated in figure Figure 3.4.

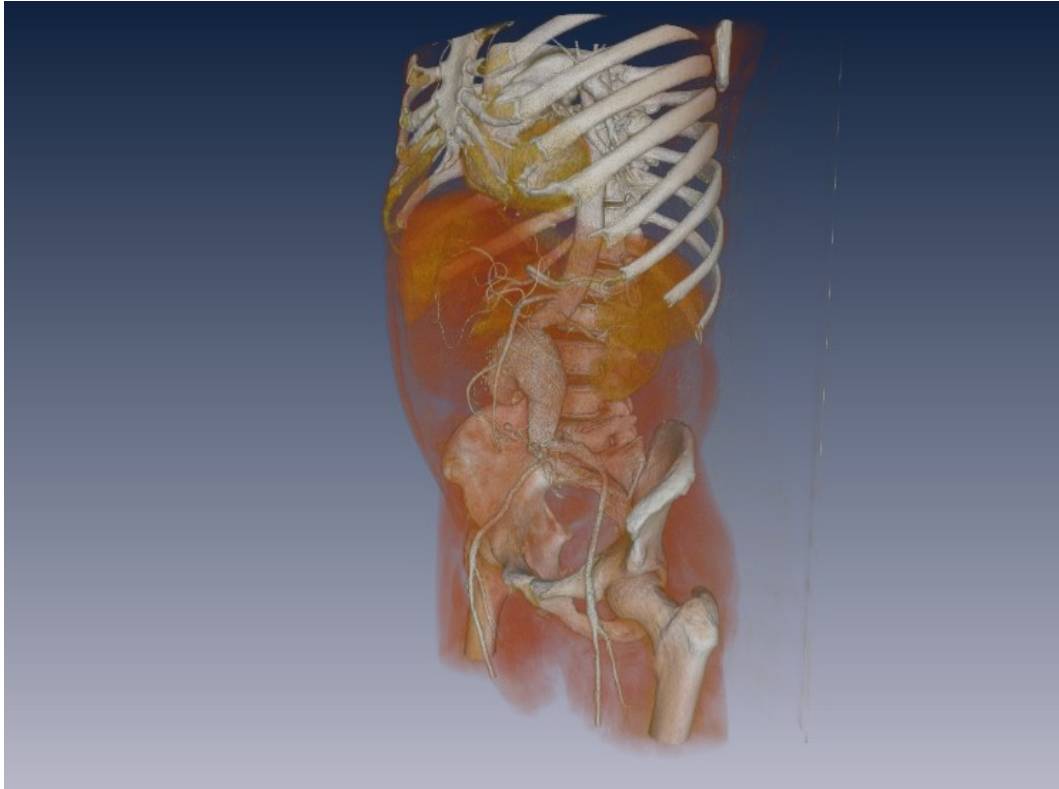


Figure 3.4.: Volume rendering of thoraco-abdominal CT slices

The most simple, and often used by radiologists, procedure for volume rendering is the Maximum Intensity Projection (MIP) method. The MIP algorithm works by projecting parallel rays (ray casting) through the volume from the viewpoint of the user. For each ray, the algorithm selects the maximum scalar value and uses that value to determine the color of the corresponding pixel on the 2D image plane. Figure Figure 3.5 shows a maximum intensity projection (MIP) of CT data of the thoracoabdominal region.

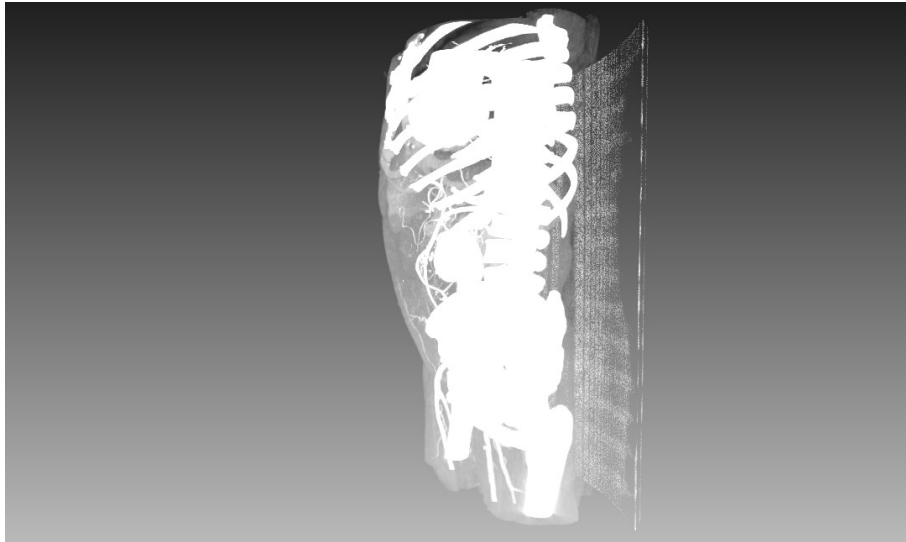


Figure 3.5.: A maximum intensity volume rendering of thoracoabdominal CT slices data.

3.4. 3D Vascular Segmentation

A common problem shared by many segmentation methods is that automated methods for partitioning structures within a dataset may not correspond to the object or structures meaningful to a human expert.

- *over-segmentation*: the data is fractured into many small pieces that have to be aggregated into whole structures using expert human intervention.
- *under-segmentation*: a dataset requires later subdivision of mixed or connected objects into separate pieces.

For this reason automated segmentation methods are often mixed with graphic user interfaces to allow clinicians and researchers to explore, manipulate, and edit the results created by computer segmentation algorithms. Meanwhile medical technicians have to process a large number of images with much more details. Compared with the algorithms for common imagery segmentation, the ones used for medical images require more concrete application background knowledge. *A priori* knowledge about the imaging procedure or the biomechanical behaviors of organs can be crucial for a successful segmentation. Also, medical images are usually low contrast to noise, so robustness requirements are stronger. In the following sections, segmentation algorithms are classified into three categories: algorithms based on threshold, algorithms based on pattern recognition techniques, and algorithms based on deformable models.

3.4.1. Thresholding Algorithms

Most of the algorithms that belong to this category make the assumption that the interested structures can be discerned by quantifiable features, like image intensity or gradient magnitude. Segmentation is a procedure of searching for pixels that satisfy the rules defined by the thresholds. Thresholds in these algorithms can be selected manually according to *a priori* knowledge or automatically through image information. Due to the noise influence and partial volume effect, the edges of organs or structures in medical images are usually not clearly defined and therefore algorithms based on threshold are seldom used alone. Algorithms can be further divided to edge-based, region-based and hybrid.

Edge-based algorithms: thresholds are related with the edge information. Structures are depicted by edge points. Common edge detection algorithms such as Canny edge detector [28] and Laplacian edge detector can be classified to this type. For example, Canny edge detector uses the threshold of gradient magnitude to find the potential edge pixels and suppresses them through the procedures of the non-maximal suppression and hysteresis thresholding. Due to the discrete nature of the images the detected edges may be incomplete or discontinuous. Hence, it is necessary to apply post-processing like morphological operations to connect the broken boundaries.

Region-based algorithms come from the observation that pixels inside a structure tend to have similar intensities. Region growing algorithm [3] is a typical algorithm of this type. After selecting initial seeds, algorithms begin to search for the neighbored pixels whose intensities are inside the intervals defined by the thresholds and then merge them to expand the regions. To eliminate the dependence on initial seeds and make the algorithm more automatic, statistical information and *a priori* knowledge can be incorporated, such as an adaptive homogeneity criterion robust to the different locations of initial seeds. However, as the algorithms mainly rely on the image intensity information, they do not handle partial volume effects (when a pixel represents more than one kind of tissue type).

Hybrid algorithms combine different image cues to achieve the segmentation. Typical examples are the watershed algorithms [16], which combine the image intensity with the gradient information. In the watershed algorithms, gray scale images are considered as reliefs and the gradient magnitude of each pixel is treated as elevation. Watershed lines are defined to be the pixels with local maximum of gradient magnitude. The segmentation procedure is to construct watersheds during the successive flooding of the gray value relief. Due to the combination of image information, watershed algorithms can achieve better results, but these algorithms tend to over-segmentation especially when the images are noisy or the objects themselves have low signal-to-noise ratio. Hybrid threshold-based algorithms can further combine with other techniques to perform the segmentation [120].

3.4.2. Algorithms Based on Pattern Recognition Techniques

As structures in medical images can be treated as patterns, techniques from pattern recognition fields can be used to perform the segmentation. Classification algorithms are the most popular ones for the medical image segmentation. However, supervised classification algorithms are sensitive to the initial conditions. To guarantee the correctness of the results, the training set must contain enough samples and the samples should be representative and segmented accurately. Popular techniques used by the supervised algorithms include supervised Artificial Neural Network (ANN) [6], Support Vector Machine (SVM) [177] and Active Appearance Models (AAM) [39]. ANN and SVM are non-linear statistical data modeling tools and can be used to model complex relationships between inputs and outputs. Weights in the classifier are estimated optimizing energy functionals, sometimes using updating rules processing each sample in the training set. The extracted information from the training set provides important cues of the structures such as intensity, position and shape, which can be valuable complementary information for the segmentation of test images. AAM are statistical models of the shape of structures. Training samples are used to extract the mean shape, mean appearance and define ranges of shape parameters. Restrictions on shape parameters guarantee the similarity between the segmentation result and the training samples. The segmentation procedure is to find the better positions of the shape points according to the appearance information. Algorithms based on classifiers have been widely applied to segment organs in medical images like cardiac and brain images. Frequently used unsupervised classification algorithms include Fuzzy C-means algorithm [118], Iterative Self-organizing Data Analysis Technique Algorithm and unsupervised neural network [34].

3.4.3. Algorithms Based on Deformable Models

Algorithms based on deformable models are very flexible and can be used for complex segmentations. According to the representation of the contour, deformable models can be classified into parametric models and geometric models. A moving equation should be defined to drive the initial contours to the structure boundaries. Therefore, the procedure of these algorithms can be viewed as a modeling of curve evolution. The moving equation for the parametric deformable models can be derived from either an energy functional or dynamic forces.

The parametric deformable models have a tight relationship with the snake method [83]. Snake method was the first deformable model applied to medical image segmentation. Contours are sampled as discrete points and are tracked according to their respective moving equations. The explicit tracking has the advantage of high computational efficiency, so that it allows for real-time applications. The traditional snake method relies on the gradient information, therefore is sensitive to the initial position of the contour. The contour must be placed to the positions near to the

structure boundary so that the external forces are strong enough to attract the contour. Otherwise the contours may converge to wrong positions.

The geometric deformable models are based on the level set method [124] which was initially proposed to handle the topological changes during the curve evolution. The main idea of the level set method is to implicitly embed the moving contour into a higher dimensional level set function and view the contour as its zero level set (Figure Figure 3.6). Then, instead of tracking the contour points, we can track the zero level set of the level set function. The advantage of doing so is that topological changes can be naturally handled and the geometric properties of the contour such as normal vector and curvature can be calculated implicitly. Consequently, the computational complexity is decreased. Like the parametric deformable models, speed functions should be properly defined. Malladi, et al. [109] and Caselles, et al. [29] first applied the level set methods to medical images. Malladi's model used the gradient information as a stop criterion. The definition of the contour's speed is intuitive: when the contour moves to the structure boundary, the increase of gradient magnitude decreases the speed value therefore slows down the contour motion. However, this speed model suffered from leakage due to its mere dependence on the gradient magnitude.

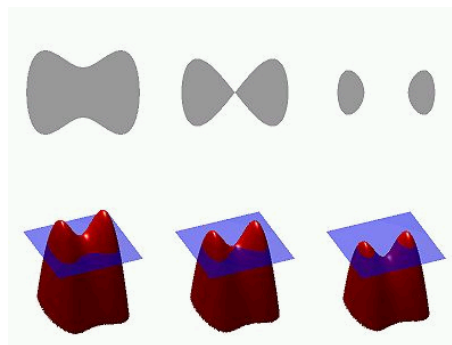


Figure 3.6.: An illustration of the level set method

Unlike Malladi's model, the Geodesic Active Contour algorithm (GAC) [29] treated the segmentation as an optimization problem of finding the minimal distance curve. The moving equation of GAC is also derived through energy functional. While instead of solving directly the moving equation, the contour is embedded in a level set function and the moving equation then becomes a level set equation. . The introduction of level set representation in GAC makes the algorithm flexible to handle the topological changes. GAC and the later improved GAC algorithms have been applied to process the MR, CT and ultrasound images like the tumor detection and vascular segmentation.

3.5. AAA segmentation

The assessment of AAA begins with a computed tomography angiography (CTA) study, in which several hundred of axial images are acquired during the first arterial pass of intravenous iodinated contrast material. Aneurysm size is relatively easy to determine using the reconstructed transaxial, sagittal and/or coronal cross sections. However, determination of aneurysm morphology, including the length and location of the proximal neck as well as the location and patency of important branch vessels, is much more difficult, and often requires tedious manual interaction to segment the aorta and branch vessels. While there are some methods for segmentation of the iodinated contrast content of the lumen, accurate automatic determination of the outer aortic wall and thrombus bulge is presently a challenging problem.

In anatomical regions where the vessel wall is surrounded by fat, segmentation is relatively easy. However, where the wall touches muscle and/or other vascular structures, the difference in CT attenuation values is small compared to expected noise and artifacts, making automatic methods problematic. Manual segmentation, involving hand tracing of tomograms using a pointing device, requiring trained operators, is often time-consuming, tiring, and prone to inter- and intra- observer variability.

3.5.1. Lumen Segmentation

Segmentation of the lumen is typically performed by a 3D region growing algorithm [3] computed on the CTA volume [94]. The CTA signal of the contrasted blood flowing through the lumen is hyper intense, with good contrast against surrounding tissues. Minor confusion may occur with calcifications and the frame of the stent graft. First, a Volume of Interest (VOI) is defined in order to reduce the extent of the data and then preprocessed to reduce noise. A manually given seed point on the lumen is at least required for the region growing algorithm. The algorithm includes voxels whose intensity values lie in a confidence interval defined over the current segmented region over an iterative process.

3.5.2. Thrombus Segmentation

The AAA's thrombus segmentation is still a difficult task, for which only a handful of methods have appeared in the literature.

A semi-automatic method based on Active Shape Model (ASM) is described in [45]. On average it requires one out of six image slices to be segmented manually. The automatized part of the segmentation is performed by fitting an ASM to a slice on the basis of landmark points in manually labeled training images, using the result from the previous slice as a reference. The shape is captured by a point distribution

model. For each slice of the training set, a vector containing the positions of the landmarks is formed. The covariance matrix of these vectors is built subsequently, and a principle component analysis (PCA) is performed. A new shape is then approximated by the vector of the mean positions, to which a linear combination of the largest eigenvectors of the covariance matrix is added. The optimal fit is determined on the basis of multi-resolution gray level models constructed from gray value patches sampled around each landmark. Only the similarity of adjacent image slices for this gray level model is used because of the high variability in thrombus' shape within the whole data set. The reported results are accurate, but the amount of user intervention is large, since slice-by- slice control is required.

A method based on 3D deformable model is introduced in [162]. The application uses a 3D deformable model implemented using the level-set algorithm, but the contrast of outer boundary is quite low. Low contrast areas produce large gaps on the aortic boundary. which level-set algorithm can't handle. In order to eliminate large boundary gaps, several pre-processing steps are used, such as local thresholding to image data, thresholding the image gradient with two thresholds, and some other knowledge based image processing. After all slices are processed, a binary volume represents abdominal aorta. Then the 3D deformable model is applied on the binary volume to detect the edge and get the outer aortic boundary. Although user intervention is minimal. the reported results are not accurate.

Another method is a grey level modeling approach based on a nonparametric pattern classification technique, namely k-nearest neighbors was proposed in [122]. The intensity profile sampled along the surface normal is used as the classification feature. Manual segmentations are used for training the classifier: samples are collected inside, outside, and at the given boundary positions. The deformation is steered by the most likely class corresponding to the intensity profile at each vertex on the surface.

In [106] the internal and external radii of the thrombus of the aneurysm are modeled as radial functions in cylindrical coordinates. At every value, the origin of these functions is chosen to be the centerline point at the corresponding slices. The external and internal radii of the thrombus and the aneurysm can be defined as two contours. The segmentation procedure consists of calculating the internal and external radii at every point, which enclose the segmented region corresponding to the thrombus(Figure Figure 3.7).

3.6. Discussion

New imaging modalities, more accurate simulation models, and continued growth in computational power all contribute to confronting biomedical researchers and engineers with an unprecedented volume of information to further their understanding of biological systems and improve clinical practice. As the size and complexity of the

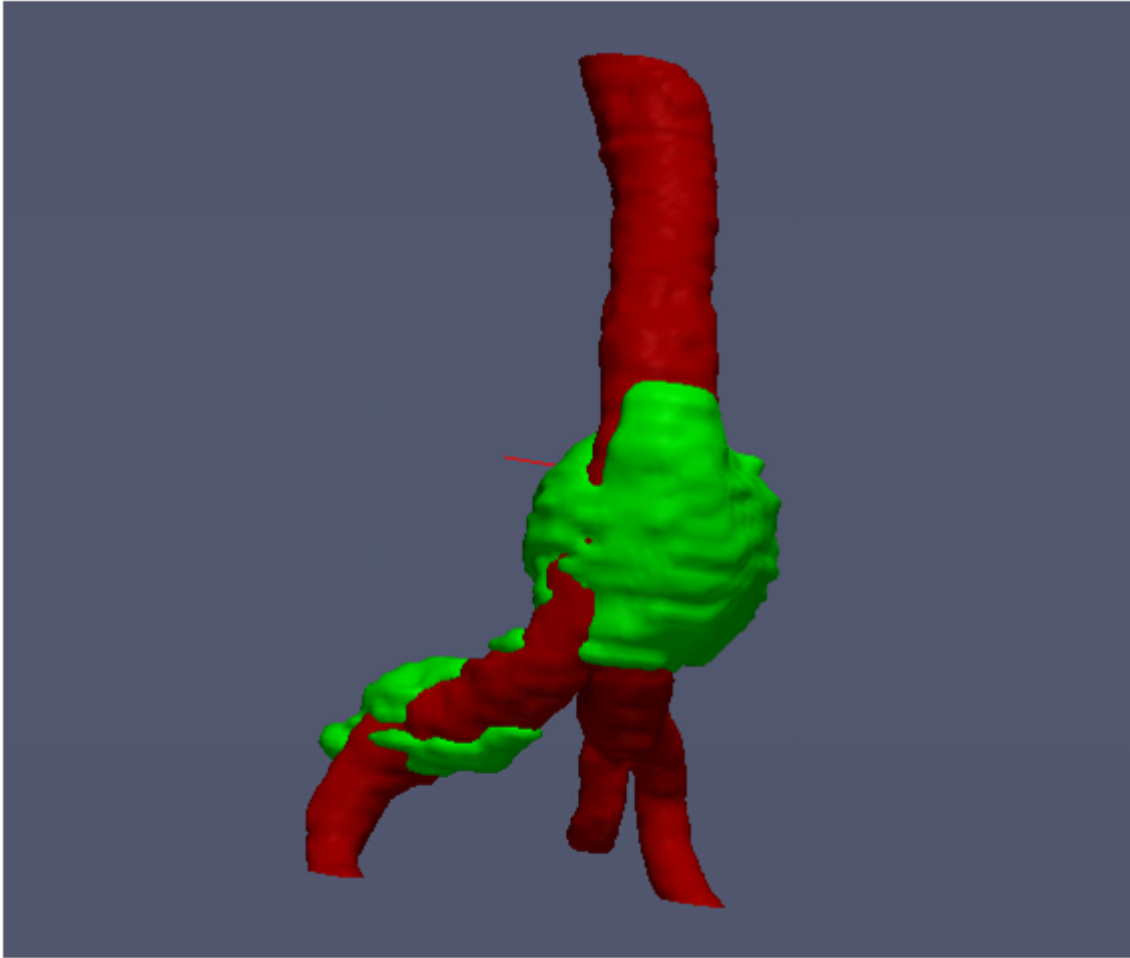


Figure 3.7.: 3D view of the segmented lumen and thrombus.

resulting data explode, the tools created by medical visualization research become crucial to gaining insight into the underlying biophysical phenomena.

High performance computing, including massively parallel computers and even powerful new micro-computer-based systems and software packages have been integrated into networks which permit access to all the information available in large 3-D image databases, facilitating rapid display, manipulation, and measurement of those data. However such facilities are far from the clinical practice, so that computational solutions that can effectively applied on of-the-shelf computers are still required. This Thesis contributes in some aspects to this endeavor, specifically the active learning approach to volume segmentation is intended for application in the clinical practice.

4. Machine Learning for Medical Image Analysis

This chapter provides a review of the Machine Learning techniques and methodologies that are applied for Medical Image Analysis along the remaining chapters of the Thesis. Section section 4.1 gives some introductory remarks and motivation of Machine Learning in Medical Image Analysis. Section section 4.2 presents the Active Learning that will be used for thrombus segmentation. Section section 4.3 provides a review of classification methods based on Artificial Neural Networks. Section section 4.4 provides a review of classification methods based on statistical approaches.

4.1. Introduction

The increasing number and complexity of the images requires new capacities to interpret them. CT images acquisition as increased its resolution so that many more and thinner slices than in the past are produced in each study. The time needed for interpretation by the radiologists increases as the number of CT slices grows, consequently increasing the probability of error due to fatigue and other problems inherent human machine interaction.

Automated intelligent image analysis is becoming an essential component of medical image analysis procedures, such as image segmentation, registration, and computer-aided diagnosis. Machine learning may play an important role when we have problems that complicate medical image segmentation such as high anatomic variability, vague and incomplete boundaries, inadequate contrast, artifacts and noise. Machine Learning provides effective techniques for these tasks, with great potential for reducing processing time and undesired errors. Actual applications include:

- medical image segmentation (e.g., brain, spine, lung, liver, kidney, colon);
- medical image registration (e.g., organ image registration from different modalities or time series);
- computer-aided detection and diagnosis systems for CT or MRI images (e.g., mammography, CT colonography, and CT lung nodule CAD).

Machine Learning algorithms learn complex relationships of patterns from empirical data to make accurate predictions and decisions [51] [17]. It is an interdisciplinary

field that has close relationships with artificial intelligence, pattern recognition, data mining, statistics, probability theory, optimization, statistical physics, and theoretical computer science.

The Machine Learning pipeline The conventional Machine Learning Pipeline consists in three elements: Feature extraction, learning algorithm, and validation of the algorithm. The two first elements can be roughly assumed to be sequentially performed. While the latter is a wrapper process that may execute many feature extraction and learning processes in order to estimate the generalization error of the classifier.

4.1.1. Learning algorithm categories

Machine learning algorithms can be categorized into supervised learning, semi-supervised learning, and unsupervised learning algorithms depending on the utilization of class labels of the train dataset samples:

- Supervised learning: each data sample is an input-output pair. The input corresponds to the quantitative features describing the object. The output corresponds to the desired system's response, which can either be a categorical variable specifying a class label or a continuous real valued variable specifying a functional relation [7]. Alternatively, the input observations can be conceptualized as causes and the output observations as effects. The goal of supervised learning is to induce a functional relationship from provided train data that generalizes well to unknown test data. The model of the relationship is a set of (non-linear) equations parameterized by numerical coefficients or weights. Examples of supervised learning include classification, regression, and reinforcement learning.
- In unsupervised learning, we only have one set of observations and there is no label information for each sample [71]. Usually these observations or features are caused by a set of unobserved or latent variables. The main purpose of unsupervised learning is to discover relationships between samples or reveal the latent variables behind the observations. Examples of unsupervised learning include clustering, density estimation, and blind source separation.
- Semi-supervised learning falls between supervised and unsupervised learning [200]. It utilizes both labeled data (usually a few) and unlabeled data (usually many) during the training process. Semi-supervised learning algorithms were developed mainly because the labeling of data is very expensive or impossible in some applications. Examples of semisupervised learning include semi-supervised classification and information recommendation systems.
- Active Learning: classifier training is embedded in a closed loop that takes the human operator, or an equivalent oracle, in an iterative enrichment of the

train data set in order to maximize the classifier generalization performance while minimizing the amount of data that must be processed by the oracle to provide supervised labels.

4.1.2. Classifier models

The classifier model states the functional relationship that is to be discovered in the data through the learning process. It also imposes limits on what can be learnt. The most popular are:

- Linear models: they assume that there is a linear relationship between the input of the model and the output of the model. Perhaps it is the simplest method for classification and regression. It has been widely used in computer-aided classification.
- Artificial neural networks (ANNs) are techniques that were inspired by the brain and the way it learns and processes information. ANNs are frequently used to solve classification and regression problems in real world applications. Neural networks are composed of nodes and interconnections. Nodes usually have limited computation power. They simulate neurons by behaving like a switch, just as neurons will be activated only when sufficient neurotransmitter has accumulated. The density and complexity of the interconnections are the real source of a neural network's computational power.
- Learning with kernels: By applying traditional supervised and unsupervised learning methods in the feature space, kernel methods provide powerful tools for data analysis and have been found to be successful in a number of real applications. Support vector machines (SVMs) are a set of kernel-based supervised learning methods used for classification and regression [25]. Typical applications of kernel-based learning methods in radiology are in CAD [176].
- Learning and inference in probabilistic models. Probabilistic models provide a concise representation of real world data and enable predictions of future events from present observations. One of the most popular probabilistic classifier is the Naive Bayes classifier. It is a classifier based on probabilistic models with strong (Naïve) independence assumptions. In spite of its oversimplified assumptions, Naïve Bayes classifiers work well in many real life applications [50].
- Ensemble learning. Ensemble learning refers to a collection of methods that learn a target function by training a number of individual learners and combining their predictions together. Bagging, bootstrapping and Adaboost are popular ensemble learning algorithms applied in medicine.

4.1.3. Feature extraction

Feature extraction is any transformation or selection process that allows to obtain a reduced representation of the data with increasing discrimination power. That is, feature extraction often produces a noise reduction and enhanced separation of the classes in feature space. Classical techniques for dimensionality reduction which can be used as feature extraction are Principal Components Analysis (PCA) [82] and Independent Component Analysis (ICA) [38]. Both are linear transformation methods. The difference is that for ICA the transformation matrix is designed to minimize the statistical dependence between its components; whereas in PCA the transformation matrix is to retain the components with maximal variance or energy. In PCA the noise corresponds to the lowest eigenvalue eigenvectors and the data informative dimensions to the high eigenvalue eigenvectors. PCA does not ensure discrimination between classes. Anyway it is still the most common transformation found in the literature because of its well know statistical properties. The ICA searches to decompose the data into statistically independent sources, hoping that some of them correspond to noise, other to informative data coefficients. There is no value associated with the sources, contrary to PCA, so that the assignation of meaning to the sources must be done by hand.

As image resolution increases significantly in the last years, more data is provided in each image, therefore input spaces increase and the classifier learning complexity increases accordingly. Therefore, dimension reduction are increasingly important. However, linear transformations have a great disadvantage, they loss all localization information, so that even we can obtain accurate classifiers, we can not attribute value to specific locations in the source image. In medical image analysis, localization is often important, because it carries some anatomical or functional significance attributed by the a priori medical accumulated knowledge. Besides, in the current scope of this thesis, feature extraction is not very relevant for the task pursued. For these reasons, we will not consider further feature extraction methods.

4.1.4. Validation

Validation plays an important role in the evaluation of machine learning algorithms such as computer-aided diagnosis (CAD) systems. Usually a machine learning algorithm will be trained on a training set and tested on a test set obtained from partitions of the given data set. Test set is intended to give some estimation of the generalization of the error of the classifier in new data. Popular partition strategies include K -fold cross-validation, leave-one-out, and random sampling. In K -fold cross-validation, the whole data set is partitioned into K subsets. A learning algorithm is trained on $K - 1$ of the subsets and tested on the remaining one. This procedure is conducted K times until all K subsets have been tested. Leave-one-out is similar to K -fold cross-validation but each subset consists of only a single sample from the dataset. Each time a sample will be held aside for testing and the learning

algorithm is trained on the other samples. This process is repeated N times, where N is number of samples in the dataset (each sample will be tested exactly once). Conventional performance measures are accuracy, sensitivity, specificity, F-index. Receiver operating characteristic (ROC) analysis provides a practical tool for model selection. An ROC curve is a 1D curve which shows the trade-off in sensitivity versus false positive rate as the threshold is varied for the decision variable for a binary classifier [203].

4.1.5. General problem statement

Here we give some notation that will be used in the definition of the algorithms and applications. In this Thesis we deal with a two class classification problem, given a collection of training/testing input feature vectors $X = \{\mathbf{x}_i \in \mathbb{R}^n, i = 1, \dots, l\}$ and the corresponding labels $\{y_i \in \{-1, 1\}, i = 1, \dots, l\}$, which sometimes can be better denoted in aggregated form as a binary vector $\mathbf{y} \in \{-1, 1\}^l$. Our aim is to classify the patients as those who have a favorable or unfavorable evolution.

4.2. Active Learning

4.2.1. Introduction

Classifier supervised learning consists in building a map from data features into a set of classes given a labeled training set. In many real life situations, obtaining the training data is costly, time consuming and error prone. This makes the construction of the training set a cumbersome task requiring extensive manual analysis of the image. This is typically done by visual inspection of the scene and successive labeling of each sample. Consequently, the training set is highly redundant and training phase of the model is significantly slowed down. Besides, noisy pixels may interfere the class statistics, which may lead to poor classification performances and/or overfitting. For these reasons, a training set should also be kept as small as possible and focused on those pixels effectively improving the performance of the model[107]. Therefore a desirable training set must be constructed in a smart way, meaning it must represent correctly the class boundaries by sampling discriminative pixels.

Generalization is the ability of providing correct class labels to previously unseen data. The difference in performance of supervised training classification algorithms when feed by different train datasets is strongly dependent on the information gain provided by the new data in one set relative to the other.

Active Learning is an strategy for the construction of the optimal set of training data, which tries to obtain the most accurate classification and greater generalization using the smallest possible training set. To this end, Active Learning [169, 36, 37] exploits the interaction with a human operator, which is the oracle providing the labels

for the samples added to the training set. These samples are optimally selected for inclusion, ensuring that they will provide the greatest increase in accuracy [148]. The incremental data selection follows some classification uncertainty criterium that does not require actual knowledge of the data sample label, thus there is no circularity in the validation process. In the context of classifier based image segmentation [190], the system returns to the user the pixels whose classification outcome is most uncertain. After accurate labeling by the user, pixels are included into the training set in order to retrain the classifier [62]. When the underlying data statistics are non stationary, so that the classifier built at one time instant may not be optimal later on, Active Learning provides an efficient methodology to retrain the already obtained classifiers, or to train them from scratch. Besides, Active Learning provides economy of computation and data labeling,

4.2.2. Query Strategy

An active learning process requires interaction between the user and the model: the first provides the labeled information and the knowledge about the desired classes, while the latter provides both its own interpretation of the distribution of the classes and the most relevant pixels that are needed in order to solve the discrepancies encountered. This point is crucial for the success of an active learning algorithm: the machine needs a strategy to rank the pixels in the pool of unlabeled data samples U . The main strategies that have been considered in the literature are (a) membership query synthesis, (b) stream-based selective sampling, and (c) pool-based sampling, (d) uncertainty sampling, and (e) query by committee. All these scenarios assume that queries take the form of unlabeled instances to be labeled by the oracle.

Membership Query Synthesis In learning with membership queries [9] the training algorithm may request labels for any unlabeled instance in the input space, including (and typically assuming) queries that the learner generates *de novo*, rather than those sampled from some underlying natural distribution. Query synthesis is reasonable for many problems, but labeling such arbitrary instances can be awkward if the oracle is a human annotator.

Stream-Based Selective Sampling An alternative to synthesizing queries is selective sampling[37]. This method assumes that obtaining an unlabeled instance is not expensive, so it can first be sampled from the actual distribution, and then the learner can decide whether or not to request its label[43]. This approach is sometimes called stream-based or sequential active learning, as each unlabeled instance is typically drawn one at a time from the data source, and the learner must decide whether to query or discard it [192].

Pool-Based Sampling For many real-world learning problems, large collections of unlabeled data can be gathered at once. This motivates pool-based sampling [95], which assumes that there is a small set of labeled data and a large pool of unlabeled data available. Queries are selectively drawn from the pool typically, in a greedy fashion, according to an informativeness measure used to evaluate all instances in the pool. The pool-based scenario has been studied for many real-world problem domains in machine learning such as text classification [95], information extraction [166], image classification and retrieval [168] [197], and cancer diagnosis [99] to name a few.

Uncertainty Sampling Perhaps the simplest and most commonly used query framework is uncertainty sampling [95]. In this framework, an active learner queries the instances about which it is least certain how to label. This approach is often straightforward for probabilistic learning models. A general uncertainty sampling strategy (and possibly the most popular) uses entropy [151] as an uncertainty measure.

Query-By-Committee Another query selection framework is the query-by-committee (QBC) algorithm [149]. The QBC approach involves maintaining a committee of models which are all trained on the current labeled set, but represent competing hypotheses. Each committee member is then allowed to vote on the labelings of query candidates. The most informative query is considered to be the instance about which they most disagree.

Additional query strategies can be divided in margin-sampling based [27] and posterior probability based families [137].

4.2.3. Active Learning Canonical Algorithm

Active learning algorithms are iterative sampling schemes, where a classification model is adapted regularly by feeding it with new labeled pixels corresponding to the ones that are most beneficial for the improvement of the model performance. These pixels are usually found in the areas of *uncertainty* of the model and their inclusion in the training set forces the model to solve the regions of low confidence.

Let $X = \{\mathbf{x}_i, y_i\}_{i=1}^l$ be a training set labeled samples, with $\mathbf{x}_i \in \mathbb{R}^d$ and $y_i \in \{1, \dots, N\}$. Let be $U = \{\mathbf{x}_i\}_{i=l+1}^{l+u} \in \mathbb{R}^d$ the *pool of candidates*, with $u \gg l$, corresponding to the set of unlabeled pixels to be classified. In a given iteration ϵ , the Active Learning algorithm selects from the pool U^ϵ the q candidates that will at the same time maximize the gain in performance and reduce the uncertainty of the classification model if added to the current training set X^ϵ . The selected samples $S^\epsilon = \{\mathbf{x}_m\}_{m=1}^q \subset U^\epsilon$ are labeled with labels $\{y_m\}_{m=1}^q$ by an oracle, which can be a human operator in interactive segmentation, or the ground truth. Finally, the set

S^ϵ is added to the current training set ($X^{\epsilon+1} = X^\epsilon \cup S^\epsilon$) and removed from the pool of candidates ($U^{\epsilon+1} = U^\epsilon \setminus S^\epsilon$). The process is iterated until a stopping criterion is met. Algorithm 4.1 summarizes the Active Learning process.

Algorithm 4.1 Active learning canonical algorithm

Inputs

–Initial training set $X^\epsilon = \{x_i, y_i\}_{i=1}^l$ ($X \in \mathcal{X}$, $\epsilon = 1$).

–Pool of candidates $U^\epsilon = \{x_i\}_{i=l+1}^{l+u}$ ($U \in \mathcal{X}$, $\epsilon = 1$).

–Number of pixels q to add at each iteration (defining the batch of selected pixels S).

```

1: repeat
2:   Train a model with current training set  $X^\epsilon$ 
3:   for each candidate in  $U^\epsilon$  do
4:     Evaluate a user-defined heuristic
5:   end for
6:   Rank the candidates in  $U^\epsilon$  according to the score of the heuristic
7:   Select the  $q$  most interesting pixels  $S^\epsilon = \{x_k\}_{k=1}^q$ 
8:   The system assigns a label to the selected pixels  $S^\epsilon = \{x_k, y_k\}_{k=1}^q$ 
9:   Add the batch to the training set  $X^{\epsilon+1} = X^\epsilon \cup S^\epsilon$ 
10:  Remove the batch from the pool of candidates  $U^{\epsilon+1} = U^\epsilon \setminus S^\epsilon$ 
11:   $\epsilon = \epsilon + 1$ 
12: until accuracy > 0.99

```

4.3. Artificial Neural Networks

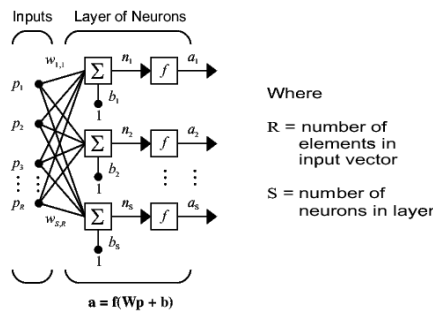
4.3.1. Neuron Model

The simple neuron unit receives the input through the synapses which modulate its value, multiplying it by a weight. The net stimulus received by the neuron is the inner product of the feature vector and the weight vector. This net stimulus is filtered by a non-linear transfer function to give the output of the neuron activation, which can be transferred to further neurons. The main advance given by Artificial Neural Networks (ANN) was that they were endowed with learning algorithms that search for the weights of the neuron that produce the desired output value (in the supervised training case). Three of the most commonly used neuron transfer functions are:

- The hard-limit transfer function limits the output of the neuron to either 0, if the net input argument is less than 0; or 1, if n is greater than or equal to 0. This was the transfer function originally proposed in the Perceptron to create neurons that make classification decisions.
- The linear transfer function is used as linear approximators in Linear Filters.

- The sigmoid transfer function takes the input, which may have any value between plus and minus infinity, and squashes the output into the range 0 to 1. This transfer function is commonly used in back-propagation networks because of the recursive expression of its derivative.

Network Architectures can be composed when the single neurons are disposed in layers such as the one illustrated in figure Figure 4.1, which can be disposed into a multilayer architecture such as the one shown in figure Figure 4.2. Each layer feeds on the outputs of the previous layer, forwarding its output to the next layer. Each layer is characterized by its own weight matrix, including the bias values of the single neurons, and the settings of the transfer functions, which conventionally are uniform over all the network. The last layer is the output layer, giving the result of the ANN process.



Where
 $R =$ number of elements in input vector
 $S =$ number of neurons in layer

Figure 4.1.: A layer in an Artificial Neural Network

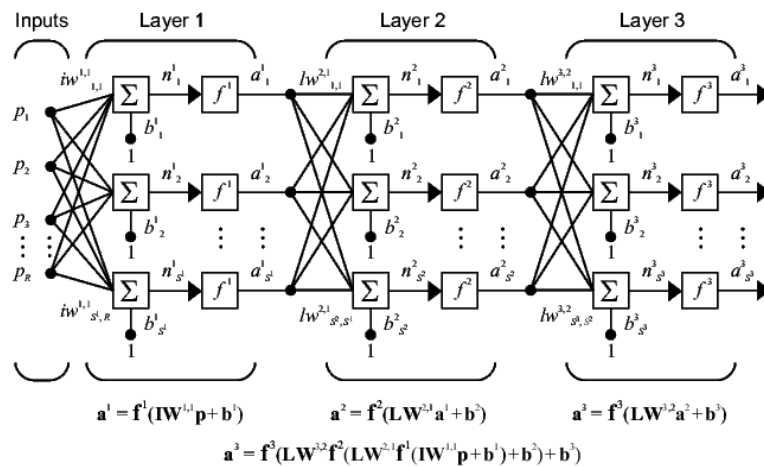
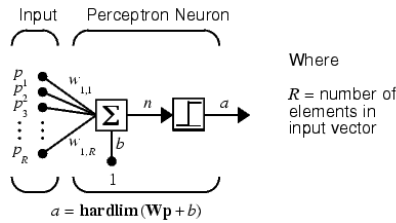


Figure 4.2.: Multilayer architecture of an ANN

4.3.2. Perceptron

The Perceptron is the oldest proposal of a learning analogic (no based on logic rules) classifier. Is a single layer system, where the single neuron is as illustrated in figure

Figure 4.3, that is, it is a neuron with a hard-limit transfer function. The perceptron learning rule is a supervised hebbian learning rule that reinforces the weights upon success and reduces them on failure to output the desired class. The Perceptron is especially suited for simple two class problems in pattern classification, providing fast and reliable solutions for problems that can be solved by a single hyperplane as the class boundary.



Where
 $R =$ number of elements in input vector

Figure 4.3.: Single Perceptron

A single layer Perceptron network consists of a single layer of S perceptron neurons connected to R inputs through a set of weights $w_{i,j}$ as shown below in two forms. As before, the network indexes i and j indicate that $w_{i,j}$ is the strength of the connection from the i th input to the j th neuron. The composition of a multi-layer Perceptron network is not so straight forward, and the learning algorithm is not defined in general. In fact, the reason that the Perceptrons were abandoned was the theoretical result that they are only able to learn a linear discriminant function, that is, they can not implement classifiers for data which are not linearly separable.

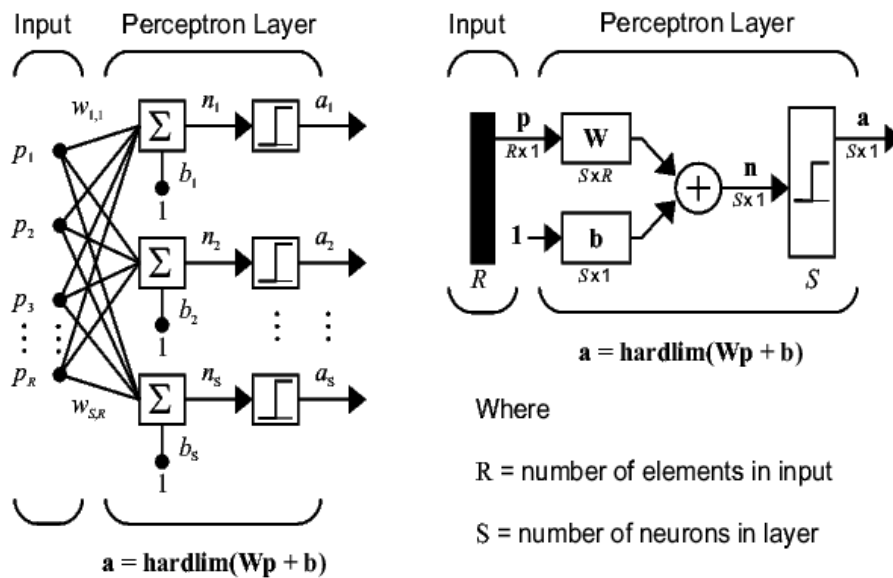


Figure 4.4.: General structure of the single layer Perceptron network.

4.3.3. Linear Networks

The linear networks discussed are similar to the perceptron, but their transfer function is a linear function rather than the hard-limiting function. Their outputs can take any value, whereas the perceptron output is limited to either 0 or 1.

Linear networks, like the Perceptron, can only solve linearly separable problems. Here we will design a linear network that, when presented with a set of given input vectors, produces outputs of corresponding target vectors. For each input vector we can calculate the network's output vector. The difference between an output vector and its target vector is the error. We would like to find values for the network weights and biases such that the sum of the squares of the errors is minimized or below a specific value. This problem is manageable because linear systems have a single error minimum. In most cases, we can calculate a linear network directly, such that its error is a minimum for the given input vectors and targets vectors. In other cases, numerical problems prohibit direct calculation. Fortunately, we can always train the network to have a minimum error by using the Least Mean Squares (Widrow-Hoff) algorithm.

4.3.4. Backpropagation

Backward propagation of errors, or Backpropagation (BP), [138][140] [72, 142, 141] is a non-linear generalization of the squared error gradient descent learning rule for updating the ANN's weights to feed-forward networks with sigmoid transfer functions, also called Multi-Layer Perceptron (MLP) with some abuse of the language. MLP is illustrated in figure Figure 4.5. The BP rule solves the problem of computing the output error gradient relative to the hidden units' weights, generalizing the Widrow-Hoff learning rule to multiple-layer networks with nonlinear differentiable transfer functions. Feedforward ANN with biases, a sigmoid layer, and a linear output layer are capable of approximating any function with a finite number of discontinuities. There are a number of variations on the basic algorithm that are based on other standard optimization techniques, such as conjugate gradient and Newton methods.

4.3.4.1. Analytical derivation

We restrict our presentation of BP to train the weights of the MLP for the current two class problem. Let the instantaneous error E_p be defined as:

$$E_p(\mathbf{w}) = \frac{1}{2} (y_p - z_K(\mathbf{x}_p))^2, \quad (4.1)$$

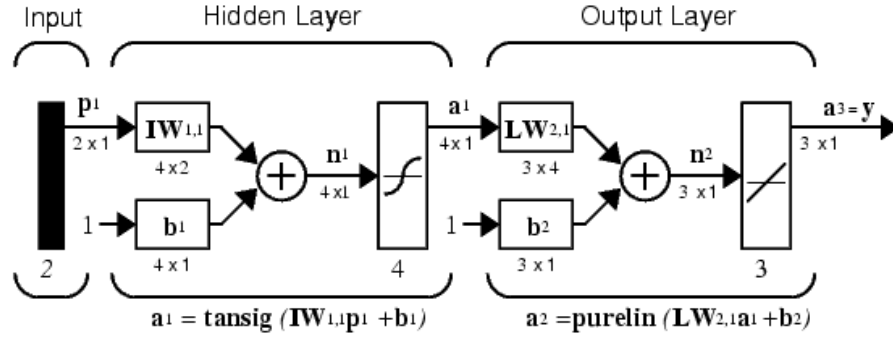


Figure 4.5.: A Multilayer Perceptron architecture

where y_p is the p -th desired output y_p , and $z_K(x_p)$ is the network output when the p -th training exemplar x_p is inputted to the MLP composed of K layers, whose weights are aggregated in the vector \mathbf{w} . The output of the j -th node in layer k is given by:

$$z_{k,j}(\mathbf{x}_p) = f\left(\sum_{i=0}^{N_{k-1}} w_{k,j,i} z_{k-1,i}(\mathbf{x}_p)\right), \quad (4.2)$$

where $z_{k,j}$ is the output of node j in layer k , N_k is the number of nodes in layer k , $w_{k,j,i}$ is the weight which connects the i -th node in layer $k-1$ to the j -th node in layer k , and $f(\cdot)$ is the sigmoid nonlinear function, which has a simple derivative:

$$f'(\alpha) = \frac{df(\alpha)}{d\alpha} = f(\alpha)(1 - f(\alpha)). \quad (4.3)$$

The convention is that $z_{0,j}(\mathbf{x}_p) = \mathbf{x}_{p,j}$. Let the total error E_T be defined as follows:

$$E_T(\mathbf{w}) = \sum_{p=1}^l E_p(\mathbf{w}), \quad (4.4)$$

where l is the cardinality of X . Note that E_T is a function of both the training set and the weights in the network. The backpropagation learning rule is defined as follows:

$$\Delta w(t) = -\eta \frac{\partial E_p(\mathbf{w})}{\partial w} + \alpha \Delta w(t-1), \quad (4.5)$$

where $0 < \eta < 1$, which is the learning rate, the momentum factor α is also a small positive number, and w represents any single weight in the network. In the above equation, $\Delta w(t)$ is the change in the weight computed at time t . The momentum term is sometimes used ($\alpha \neq 0$) to improve the smooth convergence of the algorithm. The algorithm defined by equation (Equation 4.5) is often termed as *instantaneous backpropagation* because it computes the gradient based on a single training vector. Another variation is *batch backpropagation*, which computes the weight update using the gradient based on the total error E_T .

To implement this algorithm we must give an expression for the partial derivative of E_p with respect to each weight in the network. For an arbitrary weight in layer k this can be written using the Chain Rule:

$$\frac{\partial E_p(\mathbf{w})}{\partial w_{k,j,i}} = \frac{\partial E_p(\mathbf{w})}{\partial z_{k,j}(\mathbf{x}_p)} \frac{\partial z_{k,j}(\mathbf{x}_p)}{\partial w_{k,j,i}}. \quad (4.6)$$

Because the derivative of the activation function follows equation Equation 4.3, we get:

$$\frac{\partial z_{k,j}(\mathbf{x}_p)}{\partial w_{k,j,i}} = z_{k,j}(\mathbf{x}_p) (1 - z_{k,j}(\mathbf{x}_p)) z_{k-1,j}(\mathbf{x}_p), \quad (4.7)$$

and

$$\frac{\partial E_p(\mathbf{w})}{\partial z_{k,j}(\mathbf{x}_p)} = \sum_{m=1}^{N_{k+1}} \frac{\partial E_p(\mathbf{w})}{\partial z_{k+1,m}(\mathbf{x}_p)} z_{k+1,m}(\mathbf{x}_p) (1 - z_{k+1,m}(\mathbf{x}_p)) w_{k+1,m,j},$$

which at the output layer corresponds to the output error :

$$\frac{\partial E_p(\mathbf{w})}{\partial z_K(\mathbf{x}_p)} = z_L(\mathbf{x}_p) - y_p. \quad (4.8)$$

4.3.5. Radial Basis Function

Introduction Radial Basis Function networks (RBF) [33] [72][73] are a type of ANN that use radial basis functions as activation functions. RBFs consist of a two layer neural network, where each hidden unit has a transfer function given by a radial activation function. Figure Figure 4.6 illustrates one hidden unit of the RBF architecture, whose activation function is detailed in figure Figure 4.7. A The output units compute a weighted sum of hidden unit outputs. Training consists of the unsupervised training of the hidden units followed by the supervised training of the output units weights. Radial basis networks may require more neurons than standard feed-forward backpropagation networks, but often they can be designed in

a fraction of the time it takes to train standard feed-forward networks. They work best when big sample sizes are available.

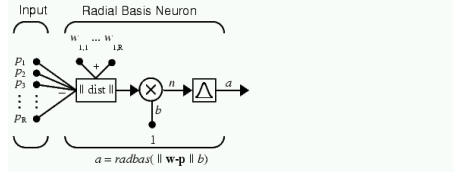


Figure 4.6.: Radial Basis Function neuron

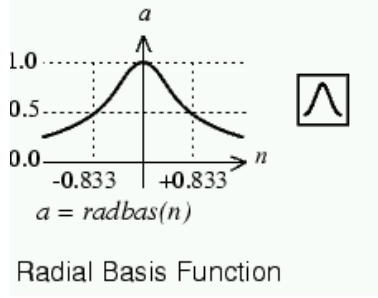


Figure 4.7.: Profile of a radially activated function for RBF activation function.

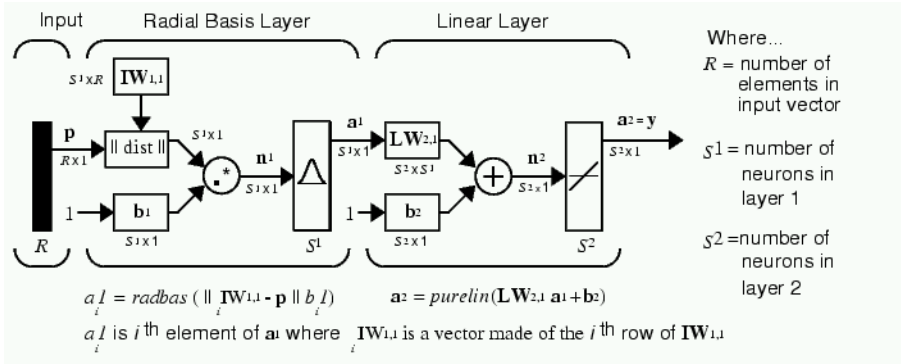


Figure 4.8.: RBF architecture, as realized in the Matlab’s Neural Networks toolbox.

Formally, RBFs have their origin in the solution of a multivariate interpolation problem [23]. An arbitrary function $g(\mathbf{x}) : \mathbb{R}^n \rightarrow \mathbb{R}$ can be approximated by a map defined by a RBF network with a single hidden layer of K units:

$$\hat{g}_{\theta}(\mathbf{x}) = \sum_{j=1}^K w_j \phi(\sigma_j, \|\mathbf{x} - \mathbf{c}_j\|), \tag{4.9}$$

where θ is the vector of RBF parameters including $w_j, \sigma_j \in \mathbb{R}$, and $\mathbf{c}_j \in \mathbb{R}^n$; let us denote $\mathbf{w} = (w_1, w_2, \dots, w_p)^T$, then the vector of RBF parameters can be expressed

as $\boldsymbol{\theta}^T = (\mathbf{w}^T, \sigma_1, \mathbf{c}_1^T, \dots, \sigma_K, \mathbf{c}_K^T)$. Each RBF is defined by its center $\mathbf{c}_j \in \mathbb{R}^n$ and width $\sigma_j \in \mathbb{R}$, and the contribution of each RBF to the network output is weighted by w_j . The RBF function $\phi(\cdot)$ is a nonlinear function that monotonically decreases as \mathbf{x} moves away from its center \mathbf{c}_j . The most common RBF used is the isotropic Gaussian:

$$\hat{g}_{\boldsymbol{\theta}}(\mathbf{x}) = \sum_{j=1}^p w_j \exp\left(-\frac{\|\mathbf{x} - \mathbf{c}_j\|^2}{2\sigma_j^2}\right).$$

The network can be thought as the composition of two functions $\hat{g}_{\boldsymbol{\theta}}(\mathbf{x}) = W \circ \Phi(\mathbf{x})$. The first one, implemented by the RBF units $\Phi: \mathbb{R}^n \rightarrow \mathbb{R}^K$, performs a data space transformation which can produce a dimensionality reduction or not, depending on whether $K > n$. The second function corresponds to a single layer Perceptron network $W: \mathbb{R}^K \rightarrow \mathbb{R}$ mapping the RBF transformed data into the class labels. Training is accordingly decomposed into two phases. First a clustering algorithm is used to estimate the Gaussian RBF parameters (centers and variances). Afterwards, linear supervised training is used to estimate the weights from the hidden RBF to the output. In order to obtain a binary class label output, a hard limiter function is applied to the continuous output of the RBF network.

4.3.6. Learning Vector Quantization Neural Network

Learning Vector Quantization (LVQ) [88] [156] represents every class $c \in \{-1, 1\}$ by a set $W(c) = \{\mathbf{w}_i \in \mathbb{R}^n; i = 1, \dots, N_c\}$ of weight vectors (prototypes) which tessellate the input feature space. Let us denote W the union of all prototypes, regardless of class. If we denote c_i the class the weight vector $\mathbf{w}_i \in W$ is associated with, the decision rule that classifies a feature vector \mathbf{x} is as follows:

$$c(\mathbf{x}) = c_{i^*}$$

where

$$i^* = \arg \min_i \{\|\mathbf{x} - \mathbf{w}_i\|\}.$$

The training algorithm of LVQ aims at minimizing the classification error on the given training set, i.e., $E = \sum_j (y_j - c(\mathbf{x}_j))^2$, modifying the weight vectors on the presentation of input feature vectors. The heuristic weight updating rule is as follows:

$$\Delta \mathbf{w}_{i^*} = \begin{cases} \epsilon \cdot (\mathbf{x}_j - \mathbf{w}_{i^*}) & \text{if } c_{i^*} = y_j \\ -\epsilon \cdot (\mathbf{x}_j - \mathbf{w}_{i^*}) & \text{otherwise} \end{cases}, \quad (4.10)$$

that is, the input's closest weight is adapted either toward the input if their classes match, or away from it if not. This rule is highly unstable, therefore, the practical approach consists in performing an initial clustering of each class data samples to obtain an initial weight configuration using equation Equation 4.10 to perform the fine tuning of the classification boundaries. This equation corresponds to a LVQ1 approach. The LVQ2 approach involves determining the two input vector's closest weights. They are moved toward or away the input according to the matching of their classes.

4.4. Statistical Classification Algorithms

4.4.1. Support Vector Machines (SVM)

The Support Vector Machines (SVM) are currently considered the state-of-the-art classifier system in the machine learning and pattern recognition community [165] [170] owing to its good generalization properties [170]. A SVM separates a given set of binary labeled training data with a hyperplane that is maximally distant from the two classes (known as the maximal margin hyperplane). The objective is to build a discriminating function using training data that will correctly classify new examples (\mathbf{x}, y) . The SVM approach to build a classifier system from the given data consists in solving the following optimization problem:

$$\min_{\mathbf{w}, b, \xi} \frac{1}{2} \mathbf{w}^T \mathbf{w} + C \sum_{i=1}^l \xi_i, \quad (4.11)$$

subject to

$$y_i(\mathbf{w}^T \phi(\mathbf{x}_i) + b) \geq (1 - \xi_i), \quad \xi_i \geq 0, \quad i = 1, 2, \dots, n. \quad (4.12)$$

The minimization problem is solved via its dual optimization problem:

$$\min_{\alpha} \frac{1}{2} \alpha^T Q \alpha - \mathbf{e}^T \alpha, \quad (4.13)$$

subject to

$$\mathbf{y}^T \alpha = 0, \quad 0 \leq \alpha_i \leq C, \quad i = 1, \dots, l. \quad (4.14)$$

Where \mathbf{e} is the vector of all ones, $C > 0$ is the upper bound on the error, Q is an $l \times l$ positive semidefinite matrix, whose elements are given by the following expression:

$$Q_{ij} \equiv y_i y_j K(\mathbf{x}_i, \mathbf{x}_j), \quad (4.15)$$

where

$$K(\mathbf{x}_i, \mathbf{x}_j) \equiv \phi(\mathbf{x}_i)^T \phi(\mathbf{x}_j), \quad (4.16)$$

is the kernel function that describes the behavior of the support vectors. Here, training vectors \mathbf{x}_i are mapped into a higher (maybe infinite) dimensional space by the function $\phi(\mathbf{x}_i)$. The decision function is:

$$\text{sgn}\left(\sum_{i=1}^l y_i \alpha_i K(\mathbf{x}_i, \mathbf{x}) + b\right). \quad (4.17)$$

The regularization parameter C is used to balance the model complexity and the training error. It was always set to 1 in this case study.

The chosen kernel function results in different kinds of SVM with different performance levels, and the choice of the appropriate kernel for a specific application is a difficult task. In this study we only needed to use a linear kernel, defined as:

$$K(\mathbf{x}_i, \mathbf{x}_j) = 1 + \mathbf{x}_i^T \mathbf{x}_j, \quad (4.18)$$

this kernel shows good performance for linearly separable data.

4.4.2. Logistic Model Tree

Logistic Model Tree (LMT) produces a single tree containing binary splits on numeric attributes, multiway splits on nominal ones, and logistic regression models at the leaves, and the algorithm ensures that only relevant attributes are included in the latter. The result is not quite as easy to interpret as a standard decision tree, but much more intelligible than a committee of multiple trees or more opaque classifiers like kernel-based estimators. Like other tree induction methods, it does not require any tuning of parameters by the user[92].

4.4.3. Random Forest

The Random Forest (RF) machine learning algorithm [21] is a classifier that encompasses bagging [20] and random decision forests [8] [77]. RF has been widely used in a variety of applications, including Virtual Reality [12]. RF became popular due to its simplicity of training and tuning while offering a similar performance to boosting. It is a large collection of decorrelated decision trees, which are ideal candidates to capture complex interaction structures in data. RF is supposed to be resistant to over-fitting of data if individual trees are sufficiently deep. Consider a RF collection of tree predictors

$$h(x; \psi_u), u = 1, \dots, U, \quad (4.19)$$

where x is a random sample of d -dimensions associated to random vector X and ψ_u independent identically distributed random vectors. Given a dataset of N samples, the bootstrap training sample of tree $h(x; \psi_u)$ is used to grow the tree by recursively selecting a subset of random dimensions \hat{d} such that $\hat{d} \ll d$ and picking the best split of each node based on these variables. Unlike conventional decision trees, pruning is not required.

$$\hat{c} = \text{majority vote}\{C_u(x)_1^u\} \quad (4.20)$$

To make a prediction for a new sample x , the trained RF could then be used for classification by majority vote among the trees of the RF as shown in Eq. (1), where $C_u(x)$ is the class prediction of the u_{th} RF tree. The important parameters of the RF classifier to set are, the number of trees in the forest -that should be sufficiently large to ensure that each input class receives a number of predictions- and the number of variables randomly sampled at each split node.

Despite the success of SVMs and boosting, these techniques do not extend naturally to multiple class problems. In principle, classification trees and forests, work unmodified with any number of classes.

5. Active Learning for Thrombus Segmentation

In this chapter we develop and apply an Active Learning approach to image segmentation of the AAA's thrombus. The rationale is that the system is intended to help the human operator to perform the thrombus segmentation in the minimal time with the minimal need to interact with the system specifying sample labels. That is, the system is not intended as classifier able to generalize to any future dataset, because the high variability of scanners and patients will prevent that. Validation is performed against ground-truth data, following a conventional machine learning methodology.

The structure of the chapter is as follows: Section section 5.1 gives an introduction. Section section 5.2 describes the learning and feature selection methods. Section section 5.3 describes the experimental setup. Section section 5.4 provides the experimental results. Section section 5.5 presents summary conclusions of the chapter.

5.1. Introduction

3D Contrast Computerized Tomography Angiography (CTA) is the preferred imaging method for tracking the evolution of AAA because it allows minimally invasive visualization of the Aorta's lumen, thrombus and calcifications. Methods for Aorta's lumen segmentation have been reported [94] [104, 105], however AAA's thrombus segmentation is still challenging due to low signal contrast between the thrombus and surrounding tissues, as can be appreciated in Fig. Figure 5.1. Furthermore, attempts to establish prior spatial information are useless because of AAA great shape variability.

Previous works Deformable models describe object shapes in a compact and analytical way, and incorporate anatomic constraints, to adapt the segmentation to the variability of biological structures over time and across different individuals [114]. In deformable models and level set-based segmentation methods, training information is incorporated into the segmentation method in an implicit way (through parameter learning). On the contrary, active shape models (ASMs) tries to utilize training

shape information in a more explicit way by building a shape model from training images and adapting the model to a new test image through an alternative optimization way [40].

Several AAA thrombus segmentation methods have been recently developed in this direction. An interactive contour tracking method performed on axial slices of abdominal CTA is proposed by De Bruijne et al. [45]. A deformable model approach based on a nonparametric statistical grey-level appearance model is employed by Olabarriaga et al. [122] to determine the deformable model adaptation direction starting from a lumen contour shape interactive segmentation. A level-set segmentation based on a parametric statistical model is presented by Zhuge et al. [202]. A deformable B-spline parametric model based on a nonparametric intensity distribution model is proposed by Demirci et al. [46]. An iterative model-constrained graph-cut algorithm is applied by Freiman et al. [57]. The above methods involve a significant user interaction either for the initialization of the segmentation process or for guiding its evolution. They are based on the optimization of some non-linear functional of the image, such that the state of each pixel is updated according to the values of the neighboring pixels searching for the optimal value of the functional. Recently, the fusion of categorization and segmentation (JCaS) has become a hot topic in computer vision [91]. In JCaS, interested objects in a 2D image are categorized and segmented simultaneously.

Alternative segmentation methods Shi and Malik proposed a graph partitioning method called “normalized cut” to perform image segmentation [153]. Given a graph $G = (V, E)$, where V represents a set of vertices and E a set of edges, a *cut* between two disjoint subsets of vertices $A, B \subset V$ is defined as $(A, B) = \sum_{u \in A, v \in B} w(u, v)$

where $w(u, v)$ is the weight of the edge connecting two nodes in subsets A and B . The cut measures the dissimilarity between the two subsets. Graph cuts have many applications in medical image segmentation including interactive or fully-automated organ segmentation for 3D CT and MRI images [19] [60] [84] [5]. Bayesian methods using Markov Random Fields (MRFs) priors have wide applications in medical image segmentation [74] [198], but its applicability to AAA segmentation is limited to the extent that there is no proper atlas that could be used as a topological *a priori*.

Segmentation by classification Image segmentation can be realized as a classification process, where each pixel receives a class label according to the pixel features which can be computed from the pixel neighborhood. Clustering algorithms may discover classes in the feature space, which can be applied directly to some medical image segmentation problems [26]. However, in the problem of AAA thrombus segmentation, we need to apply some supervised approach to perform detection of the target structure in the image. In this chapter we perform the pixel classification using random forest (RF) classifier. In the medical image domain, RF have been applied to delineate the myocardium in 3D ultrasound (US) of adult hearts

[93], brain tissue segmentation [62, 191], detection of several organs in CT volumes [41, 42]. Thrombus segmentation of AAA on CTA data volumes is a voxel classification problem mapping them into aortic thrombus or background.

Active Learning Image segmentation of 3D CTA data is affected by a variety of noise conditions so that an image segmentation procedure developed and validated on a collection of training CTA data may be ineffective when applied on new CTA data. The approach followed to tackle this problem in this thesis is to provide an Active Learning based interactive image segmentation system which will allow quick volume segmentation requiring minimal intervention of the human operator. The experimental setup is illustrated in Fig. Figure 5.2. In one experiment, we perform Active Learning on each CTA slice containing part of the thrombus. In the other experiment we apply the results of Active Learning performed on data from the thrombus' central slice to the remaining slices of the volume, providing a strong test of the generalization power of the approach. The Active Learning oracle in the experiments is the ground truth provided by manual segmentation.

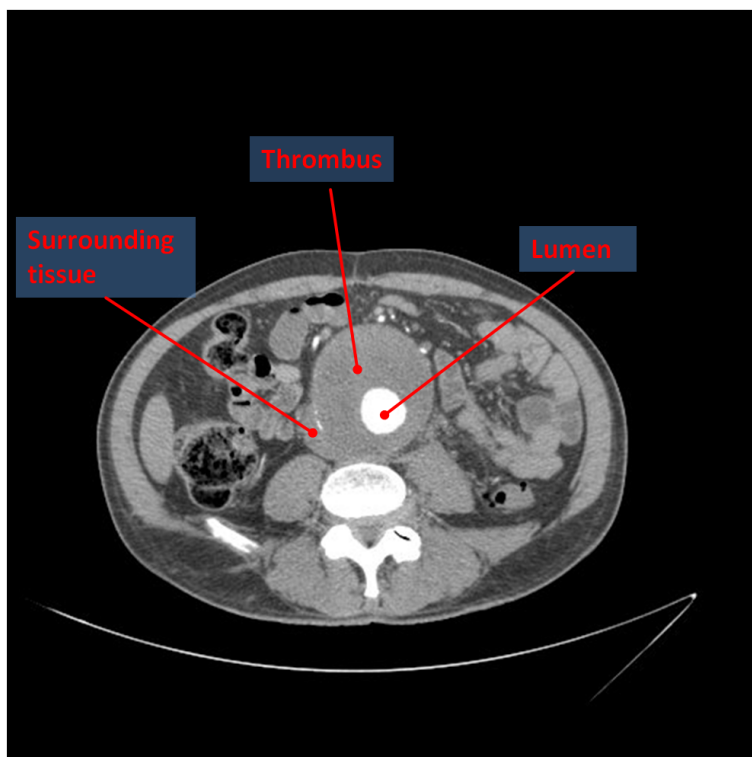


Figure 5.1.: Axial view of thrombus and lumen in a CTA orthoslice using the contrast agents, blood in lumen is highlighted but thrombus intensity levels are similar to other surrounding tissue.

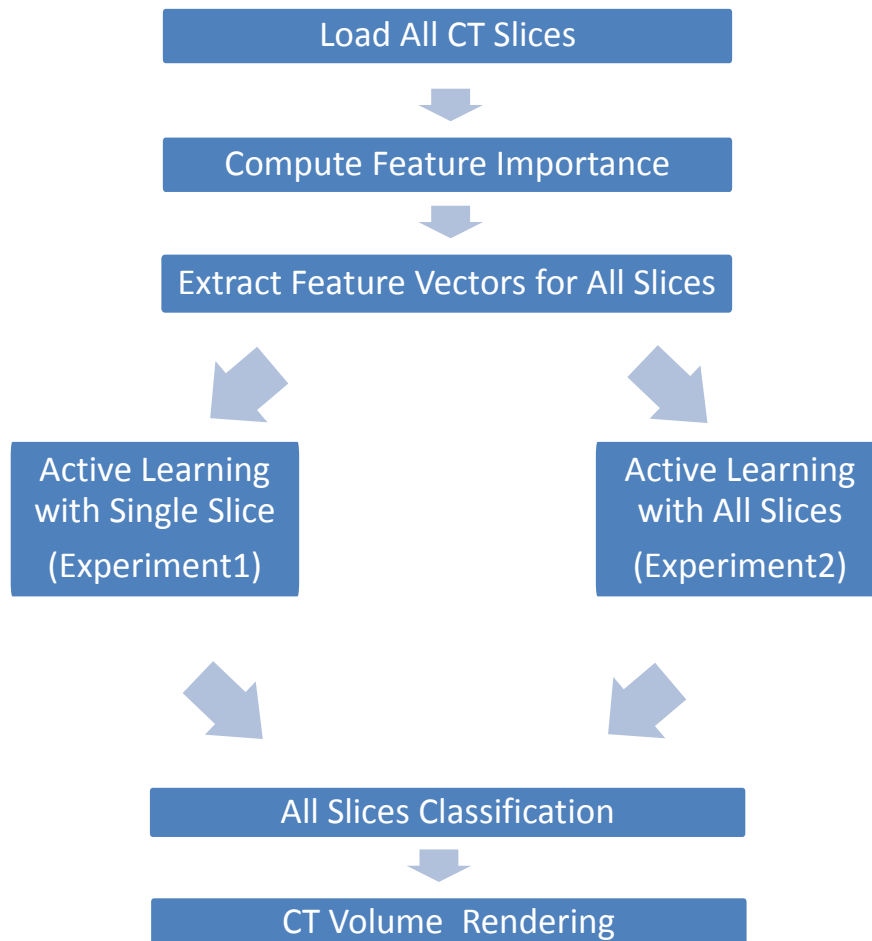


Figure 5.2.: Pipeline of the experimental setup for the Active Learning segmentation process

5.2. Learning and feature selection

Active Learning

Active Learning has been introduced in section section 4.2, including the canonical algorithm for Active Learning. In this chapter it is applied to the training of the RF classifiers for thrombus segmentation. Because RF is an ensemble, we can follow the committee approach to the prediction of the unlabeled sample uncertainty [169]: assume that we have built a committee of k classifiers, i.e. a RF with k trees, so that classification outcome is produced by majority voting. The goal is the classification of all CTA dataset voxels, therefore, the unlabeled sample set U^ϵ corresponds to the feature vectors attached to all voxels which have not been labeled or used for building a classifier in previous iterations of the Active Learning process.

In the RF implementations the committee is built by bagging [20]:

- First, we build k training sets using a draw with replacement of the original data. These draws account for a part of the available labeled pixels only.
- Second, each set is used to train a separate RF classifier, which is used to predict the uncertainty u of the candidates.

We quantify the uncertainty of a pixel as follows: The output of the RF component classifiers provide k labels for each candidate unlabeled voxel feature vector $\mathbf{x}_i \in U$. The standard deviation of the class predictions' distribution, denoted $\sigma^c(\mathbf{x}_i)$, is the heuristic measure of the uncertainty of its classification. Let us consider the candidates ordered by this uncertainty measure:

$$U^\epsilon = \{\mathbf{x}_i | (i < j) \Rightarrow [\sigma^c(\mathbf{x}_i) \geq \sigma^c(\mathbf{x}_j)]\}. \quad (5.1)$$

The set of selected voxels to be labeled by the human operator and included in the training set for the next iteration of the Active Learning, correspond to the first q candidates in this ordered set:

$$S^\epsilon = \{\mathbf{x}_i \in U^\epsilon\}_{i=1}^q. \quad (5.2)$$

Standard deviation of the classification outputs of the ensemble constituents is a natural multiclass heuristic measure of classification uncertainty. A candidate sample for which all the classifiers in the committee agree has a zero prediction standard deviation, therefore is not appropriate for inclusion in the training set because it does not bring any additional information. On the contrary, a candidate with maximum disagreement between the classifiers results in maximum standard deviation, so that its inclusion will be highly beneficial.

Feature extraction

The goal of the segmentation procedure is to classify image pixels into two classes, the thrombus region and the background [190]. Image intensity is not a discriminant value, because often many unrelated regions have similar pixel intensity values. This is specially true of voxels in CTA volume data. Feature extraction aims to attach additional information to each pixel computed from the spatial distribution of intensity values so that the spatial structures can offer more discriminant information for classification. Features are computed as functions of the intensity in neighboring pixels, the simplest ones are the first and second order statistics: average and standard deviation. The simplest non linear features are the maximum and minimum values in the pixel's neighborhood. Table 5.1 summarizes the spatial features extracted from the CTA images. The size (radius) of the neighborhood was set to powers of two: $1, 2, 4, \dots, 2^n$. With n set empirically.

Image Feature
Voxel Coordinates
Maximum
Minimum
Mean
Variance

Table 5.1.: Image features extracted to build the training set

Feature selection based on variable importance

The feature set built as specified can be of very high dimension and with much redundancies. Feature selection aims to reduce the dimension of the feature set for each pixel, increasing the discriminative power by removing redundant or non-informative features. In this chapter feature selection is done on the basis of the variable importance defined on the basis of the individual responses of the trees in the RF that we use for classification. Let us denote X^j the j -th feature of the feature vector. The variable importance of X^j is defined from the RF response as follows: For each tree $h(\mathbf{x}; \psi_t)$ of the RF, consider the associated out-of-box OOB_t dataset [21] constituted by data samples not included in the bootstrap sample used to construct $h(\mathbf{x}; \psi_t)$. Denote err_{OOB_t} the error corresponding to the misclassification rate for classification of the single tree $h(\mathbf{x}; \psi_t)$ over the OOB_t dataset.

Now, randomly permute the values of X^j in OOB_t to get a perturbed out-of-box dataset denoted by \widetilde{OOB}_t^j , and compute $err_{\widetilde{OOB}_t^j}$, the error of $h(\mathbf{x}; \psi_t)$ on the

perturbed sample. The Variable Importance of feature X^j is computed as follows:

$$VI(X^j) = \frac{1}{T} \sum_t (err\widetilde{OOB}_t^j - errOOB_t),$$

where T denotes the number of trees of the RF. To perform feature selection,

1. We order the features by decreasing value of Variable Importance, such that $VI(X^{j_i}) > VI(X^{j_{i+1}})$,
2. We compute the total variable importance of the features

$$TVI = \sum_{j=1}^N VI(X^j).$$

3. We find the first K features accounting for 95% of TVI:

$$\sum_{i=1}^K VI(X^{j_i}) \geq 0.95TVI.$$

4. We discard the remaining features

In Table 5.2 we show the image features finally selected to build the training set.

Morphological postprocessing

Morphological operators [155] are nonlinear filters, convolution-like operations applying lattice operators (infimum and supremum) on pixel neighborhoods defined by spatial masks. They have been used for edge detection, smoothing, removing noise and even detect shapes. Dilation, erosion, closing, and opening are the basic morphological operators. The structuring element defines the spatial span of the filter and some weighting that modulates it. The so-called area based operators do not depend on an specific structuring element, but work on connected components. For instance, area conditional erosion operator deletes connected components smaller of a given area, regardless of their size.

In this chapter, we apply morphological operators as a post-processing step removing small regions of false positives, disconnected from the main thrombus segmentation. We are concerned with binary images, whose pixels have values 0/1, resulting from the classification process. The structuring element can be of any size and has an arbitrary structure that can be represented by binary values. We will use a disk of diameter d as the structuring element. We briefly recall the definition of the elemental operators and filters.

The binary erosion of A by B , denoted $A \ominus B$, is defined as the set operation $A \ominus B = \{z | (B)_z \subseteq A\}$. In other words, it is the set of pixel locations z , where the

Image Feature (Filter radius)	Importance
Maximum (16)	1.277
Maximum (4)	0.9533
Maximum (8)	0.9531
Median (8)	0.8037
Maximum (2)	0.7623
Maximum (1)	0.7594
Median (1)	0.7415
Median (4)	0.7406
Median (16)	0.7328
Gaussian Blur (4)	0.725

Table 5.2.: Features selected according to the variable importance ranking

structuring element translated to location z overlaps only with foreground pixels in A .

The binary dilation of A by B , denoted $A \oplus B$, is defined as the set operation: $A \oplus B = \{z \mid (\hat{B})_z \cap A \neq \emptyset\}$ where $(\hat{B})_z$ is the reflection of the structuring element B . In other words, it is the set of pixel locations z , where the reflected structuring element overlaps with foreground pixels in A when translated to z .

Dilation and erosion are often used in combination to detect sub-images or image components. The definition of a morphological opening of an image is an erosion followed by a dilation, using the same structuring element for both operations: $X_B = (X \ominus B) \oplus B$. The morphological closing of an image is the reverse: it consists of a dilation followed by an erosion with the same structuring element: $X^B = (X \oplus B) \ominus B$.

5.3. Experimental setup

Datasets. We have performed computational experiments over 8 datasets to test the proposed Active Learning based image classification approach. Each dataset consists in real human contrast-enhanced datasets of the abdominal area with 512x512 pixel resolution on each slice. Each dataset consists of between 216 and 560 slices

and $0.887 \times 0.887 \times 1$ mm spatial resolution corresponding to patients who suffered Abdominal Aortic Aneurysm. The datasets show diverse sizes and locations of the thrombus. Some of them have metal streaking artifacts due to the stent graft placement. Ground truth segmentations of the thrombus for each dataset that simulates the human oracle providing the labels for the voxels, were performed manually by a clinical radiologist.

Segmentation problem. We are looking for the segmentation of the thrombus formed in the AAA after the placement of the endo-prosthesis. Therefore, segmentation is converted into a two-class classification problem.

Parameter tuning. In our experiments we build the feature set with Matlab, in a 8 core CPU running under Ubuntu. The total processing time to get the complete set of features for the 8 patients was 42 ours. We train the RF classifier with a single slice a to test the sensitivity of the forest parameters: the number of the trees T and their depth D . We vary T from 10 to 100 in steps of 10 and D from 10 to 24 in steps of 2. A 3-fold cross-validation is carried out for each parameter combination. In Fig. Figure 5.3 segmentation results are evaluated for each combination of RF parameters to compute the response surface of classification accuracy due to variations in RF parameters. The surface corresponds to the average accuracy in the 3-fold cross validation. The figure shows that for a fixed depth, increasing the number of trees and the depth leads to a more accurate classification. The increase in performance stabilizes around number of trees = 80 and depth = 20.

Once we get the optimal parameters and feature set, we have designed two different experiments to test the proposed approach in the patients' CTA volumes as illustrated in figure Figure 5.2:

1. Independent slice classifier: we build a separate RF classifier for each slice of the volume, applying an Active Learning strategy, and we test it with the corresponding slice.
2. Generalization of a single slice classifier: we build only one RF classifier from the data of the central slice of the aneurysm, applying an Active Learning strategy, and we apply it to the classification of the remaining slices of the CT volume, testing the generalization power of the learnt classifier.

Validation. The performance measure results of the experiments is the classification accuracy. For the first experiment, the independent slice classifiers, we average the classification accuracy obtained on each slice at each iteration of the Active Learning process. That is, we obtain the average evolution of the classification accuracy, with a corresponding variance value. For the second experiment, we plot the accuracy obtained when applying the single RF classifier on each slice.

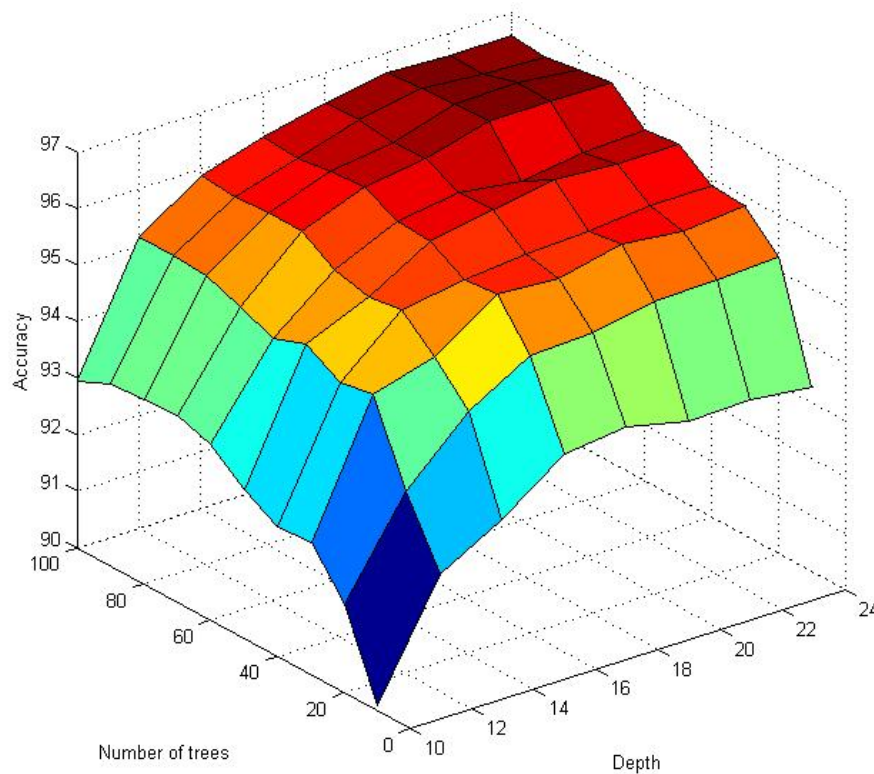


Figure 5.3.: Accuracy of the segmentation as a function of the RF parameters: number of trees and depth.

5.4. Experimental Results

Fig. Figure 5.4 shows the performance of the Active Learning based image segmentation algorithm for 6 CTA volumes of AAA patients. We plot the average accuracy of the RF classifiers built at each iteration of the Active Learning process on each slice, the abscissas correspond to the number of voxels being added to the training set, 5 voxels per iteration. It can be appreciated that all plots converge reaching 0.99 accuracy after four iterations (20 voxels added). The variance of the classification accuracy is represented by a blue region around of the mean, upper and lower limits correspond to adding and subtracting two times the standard deviation. Additionally the accuracy's variance drops dramatically after the fourth iteration, becoming negligible after the fifth iteration. The Active Learning process is extremely robust.

The experiment reported in Fig. Figure 5.4 is equivalent to asking of the human operator to follow the Active Learning procedure on each slice, which amounts to some two hundred independent segmentation processes, restricting the work to the CTA slices containing the AAA thrombus. Then we run the experiment in which we test the all the slices with the classifier built on the training set corresponding to the image features of one single slice, therefore achieving a hundred-fold reduction

on the human effort. We can observe that the approach provides good performance detecting and segmenting the anatomical structures in several consecutive slices. If the RF classifier obtained on one slice can be applied to the remaining slices without loss of accuracy, the human operator would only need to perform once the Active Learning process to obtain the whole volume segmentation. Fig. Figure 5.5 shows the overlaid plots of the accuracy obtained at each CTA volume slice applying the RF classifier trained on the thrombus central slice for each of the 8 CTA volumes in the experiment. The abscissa's zero value corresponds to the central slice, the negative abscissa values correspond to slices above the central slice, the positive values correspond to slices below the central slice. There is some variability of the plots' span, due to the different sizes of the thrombus in each patient. As can be expected, the drop in classification accuracy is symmetric. The generalization results are very good: the lowest accuracy is above 0.98 in almost all cases. This results comes with a hundred-fold reduction of learning complexity involving computer and human operator time.

The segmentation quality has minimum variations from one slice to the next. Thrombus segmentation is preserved, and the false positives are distributed in similar way. Fig. Figure 5.6 shows the segmentation of six consecutive slices. The final step of the system applies a morphological opening operator to get rid of the false positives, obtaining the mask of the aneurysm thrombus. Fig. Figure 5.7 shows the results of the opening on several consecutive slices of the same patient after classification with the RF trained in 8 Active Learning iterations on the central slice. We observe little variation between consecutive slices. The evolution of the DICE coefficient values after each Active Learning iteration is shown in the figure Figure 5.8. After the first two iteration DICE values are still relatively low, but after the third iteration there is a steep increase above 0.8. We observe that the segmentation quality reaches a maximum after 6 Active Learning iterations.

A 3D volume rendering of the Aorta's lumen (green) and thrombus (red) of one patient is shown in Fig. Figure 5.9 in three situations. Fig. Figure 5.9(a) shows the rendering of the ground truth given by volume manual segmentation. Fig. Figure 5.9(b) shows the result of the segmentation based on the Active Learning performed on each slice. The high accuracy of the segmentation is evident from the comparison with the rendering of the manual segmentaion. Fig. Figure 5.9(c) shows the result of the segmentation based on the RF classifier built from the thrombus' central slice. The structure of the thrombus is well delineated, most errors come from the identification as thrombus of separate structures which can be easily removed by morphological operations.

5.5. Conclusions

This chapter presents an Active Learning approach to the segmentation of the AAA's thrombus for posterior measurement and monitoring. Active Learning is justified by the difficulty of ensuring that learned classifiers will remain valid for new data due to the great anatomical variability in the patients, as well as the variability of the imaging sensors. The results are quite positive, showing that a great reduction of human segmentation effort preserving a high accuracy can be obtained by the procedure of training a classifier on the central slice and applying it to the remaining slices, followed by a simple morphological post-processing.

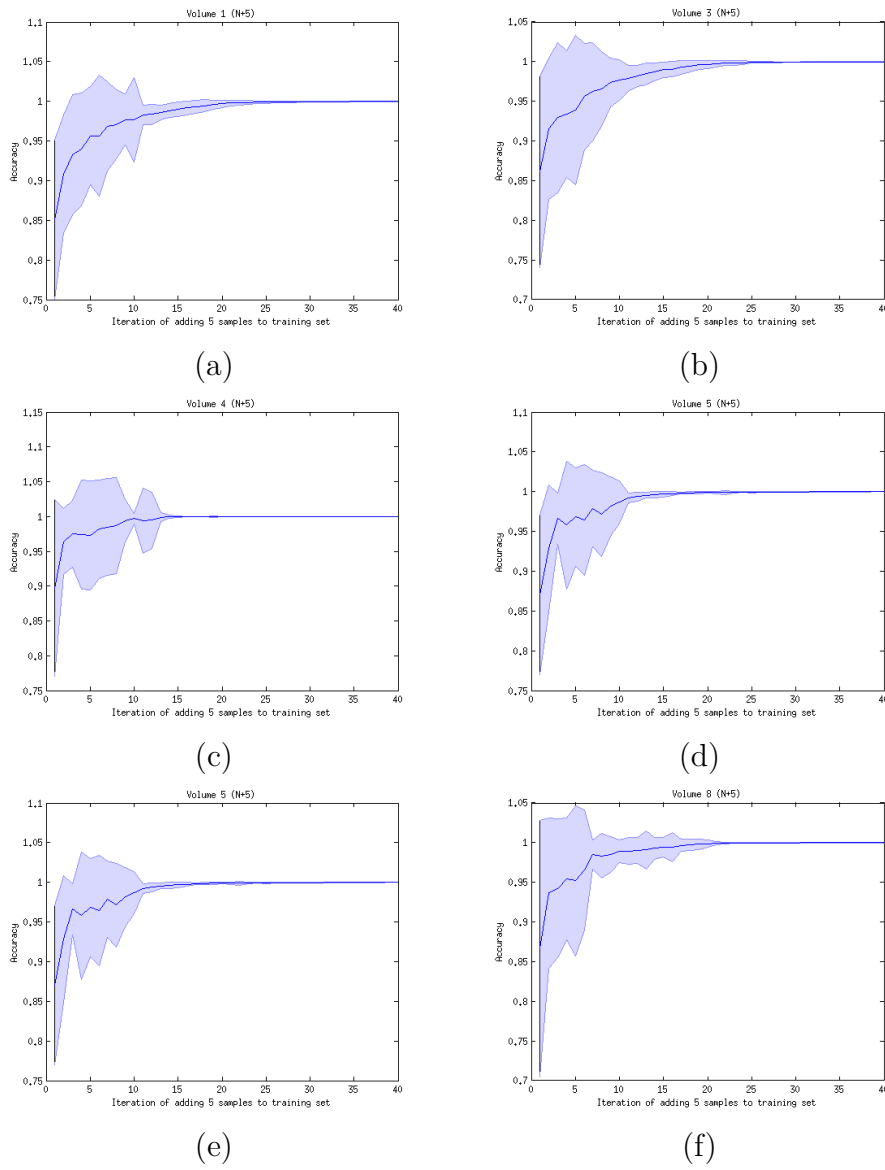


Figure 5.4.: Average and standard deviation interval of the classification accuracy at each slice versus size of the additions to the train dataset for the 6 CTA volumes of AAA patients. Active Learning adds the 5 most uncertain unlabeled samples to the train dataset at each iteration. Initial train dataset of 20 voxels.

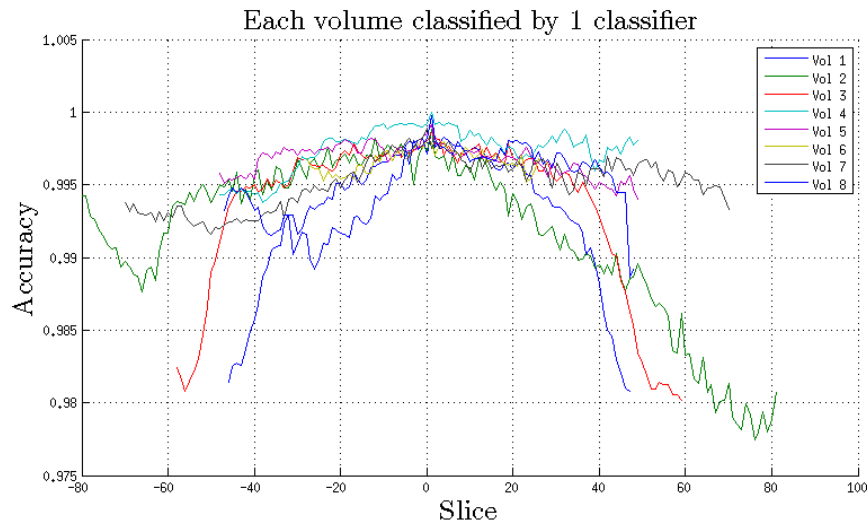


Figure 5.5.: Generalization result. The classifier learned on the central slice is applied to the remaining slices.

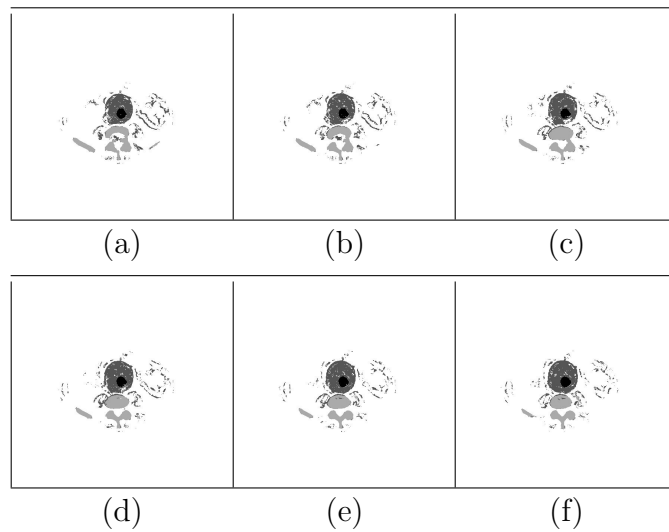


Figure 5.6.: Segmentation of 6 consecutive abdominal slices of the same patient after RF classification process. Lumen (darkest circle in the center), thrombus (circle around lumen), and bones (backbone and rib) are distinguished.

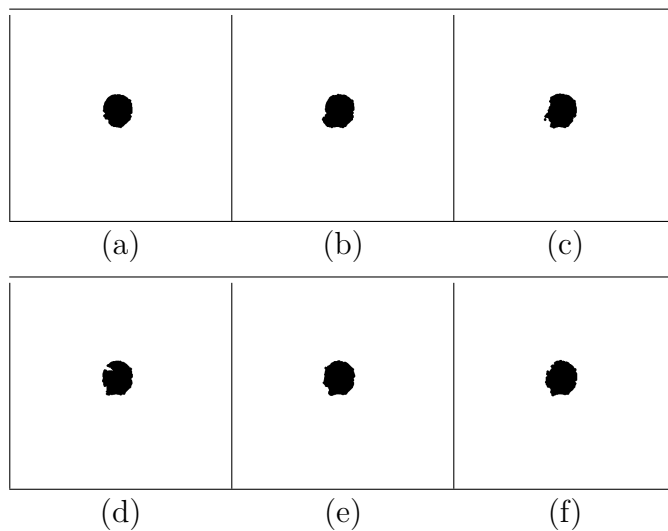


Figure 5.7.: Segmented images after opening to remove noisy false positive components: 6 consecutive abdominal aortic aneurysm thrombus slices of the same patient.

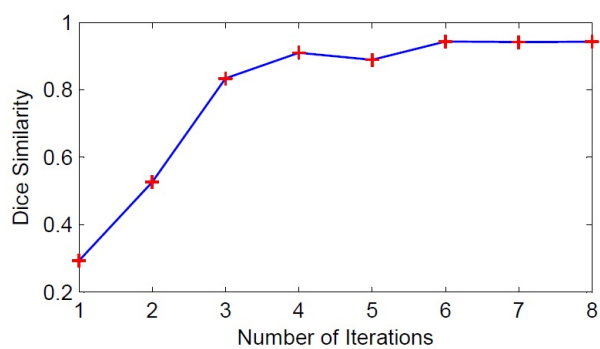


Figure 5.8.: Dice similarity measures after each iteration

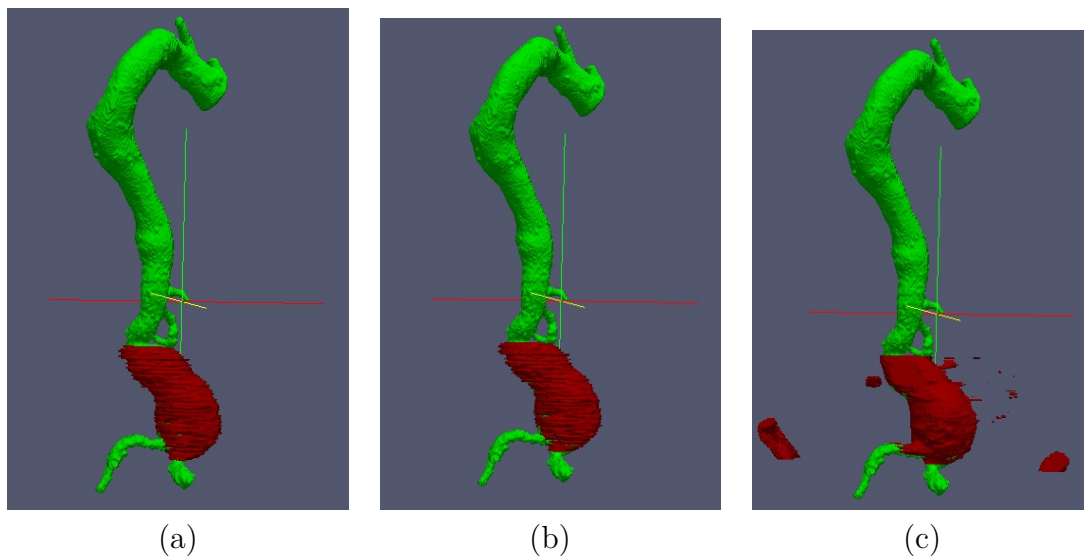


Figure 5.9.: Volume rendering of aortic lumen (green) and thrombus (red) obtained from the segmentation of one CTA volume. (a) manual segmentation of the ground truth, (b) result of Active Learning RF classifiers detecting the thrombus in each slice, (c) result of generalization of the Active Learning the RF classifier on the central slice to the remaining slices.

6. Abdominal Aortic Aneurysm Registration

This chapter describes the works done on the registration of images of the Abdominal Aortic Aneurysm (AAA) taken at different time instants. The registration allows the accurate comparison of the state of the aneurysm in these time instants, so that a clinician can easily determine the evolution of the thrombus by visual inspection.

Section section 6.1 gives a short introduction. Section section 6.2 gives an overview of registration algorithms. Section section 6.3 explains the Aorta's lumen registration. Section section 6.4 presents results on the thrombus co-registration. Section section 6.5 gives some conclusions of the work reported in this chapter.

6.1. Introduction

Image registration is the process of overlaying two or more images of the same scene taken at different times, from different viewpoints, and/or by different sensors, so that the same pixel site corresponds to the same point in the real life object. In medical images, the goal is that the pixel or voxel images the same anatomical point.

As illustrated in figure Figure 6.1, registration considers a *fixed* image, corresponding to the nominal positions of the objects in the scene, and a *moving* image, which must be transformed to overlay as much accurately as possible the fixed image. The moving image is transformed according a domain transformation, applying interpolation methods to allow for numerical accuracy. The quality of the registration is measured using a image comparison metric. The estimation of the best transformation is performed as an optimization process over the transformation parameters maximizing the registration quality. Registration techniques can be categorized by the transformation computed to align the moving image to the fixed image:

- Rigid registration permits translation in any direction and rotation around any axis, resulting in six degrees of freedom in 3D imaging.
- Affine registration adds skew and scaling to the rigid transformations, permitting 12 degrees of freedom for 3D image sets [87].
- Deformable registration algorithms [90] computes non-rigid free-form transformations from. Deformable registration involves much more parameters than

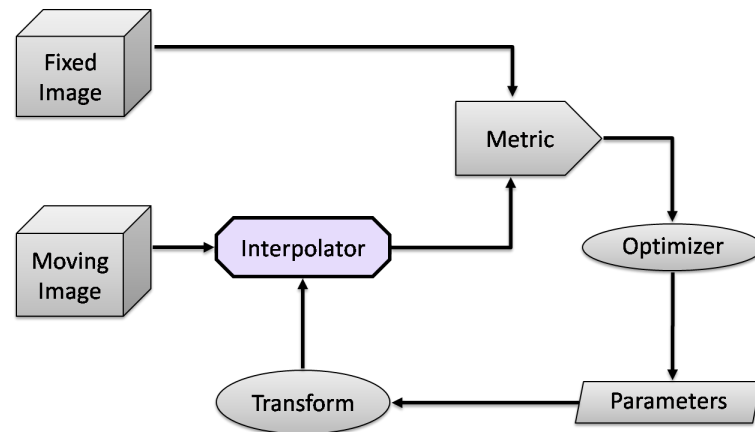


Figure 6.1.: Image Registration Framework[79]

rigid and affine registration, and despite advances reached so far, it is still a topic of ongoing research[152][87].

Rigid and affine registration methods have been shown to be effective in aligning PET, CT and MR images of the brain where the rigidity of the skull prevents arbitrary deformation [178]. However, in more general cases, rigid and affine approaches cannot sufficiently model the image differences. Registration algorithms can also be grouped according to the kind of information used:

- Feature based methods require the preprocessing of the images to extract features such as edges, landmarks, segmented structures and texture. For instance, non-rigid registration based on by correspondence of boundary structures is reported in [53, 52][125][160].
- Voxel-based methods work directly on the image gray values without any preceding feature extraction. Voxel-based methods are more flexible and less reliant on the success of the processing steps, but they have a higher computational cost [126][152].

Image registration is a critical step in image analysis tasks combining information from various data sources like in image fusion, change detection, and multichannel image restoration[76]. The ability to register images from different image modalities is also important to fuse the information from each mode, enabling better clinical decisions to be made. Much of the early work in medical image registration was dedicated to co-registration of brain images of the same subject acquired with different modalities (e.g. MRI and CT or PET) [128]. For these applications a rigid body approximation was sufficient as there is relatively little change in brain shape or position within the skull over the relatively short periods between scans. There have been several recent reviews that cover these areas in more detail [66]. Clearly most of the human body does not conform to a rigid or even an affine approximation and much of the most interesting and challenging work in registration today involves the development of non-rigid registration techniques for applications ranging from

correcting for soft-tissue deformation during imaging or surgery [55] to modeling neuro-anatomical changes [75].

Intramodality or intermodality studies use the same or different image acquisition technology. Intrasubject studies use images of the same subject, while intersubject studies use images from different subjects. Using these two axes, with an application-centered emphasis, we can divide the methods of registering images in:

- Intramodal, intrasubject: in this case it is aligning images of the same type and the same subject acquired at different time points. For example, one can study the longitudinal changes in a patient due to treatment, variations due to disease progression or check the result of surgery[167].
- Intramodal, intersubject: the use of this type of registration can compare images of different subjects and find differences between them. The image analysis procedure fMRI [188] and PET known as SPM (Statistical Parametric Mapping) requires this step before comparing studies. Using a reference atlas to assist in locating such structures also requires registration.
- Intermodal, intrasubject: studies using different methods for the same subject opens the possibility of combining the information from all of them. Thus, the precise location allowing anatomical modalities such as MRI or CT can be supplemented with functional information from PET or SPECT[159].
- Intermodal, intersubject: this case is the least practical applications presented so far. One of them could be the registration of PET or SPECT images with an anatomical atlas, but so far several difficulties are impeding good results.

Co-registration is the process of computing the optimal registration transformation over one object and applying it to a related object. In this chapter we perform co-registration of the aneurysm's thrombus by the Aorta's lumen. The rationale is that the Aorta's lumen is a stable object with the same shape in time, while the thrombus will be subject to shape changes due to reductions or dilations, according to the positive or negative evolution of the patient. Therefore, direct thrombus registration would mask the effect that we are trying to highlight to the clinician. The process followed has two steps:

1. Registration of the Aorta's lumen using affine and deformable registration.
2. Application of the transformation to the segmented thrombus to overlay its two time instants.

6.2. Overview of Registration Algorithms

Registration based on patient image content can be divided into geometric approaches and intensity-based approaches.

- Geometric approaches build explicit models of identifiable anatomical elements in each image. These elements typically include functionally important surfaces, curves and point landmarks [135] that can be matched with their counterparts in the second image, defining correspondences used to estimate the transformation parameters. The use of such structural information ensures that the mapping has biological validity, allowing the transformation to be interpreted in terms of the underlying anatomy or physiology.
- Intensity-based approaches match intensity patterns in each image using mathematical or statistical criteria. They are based in the definition of a measure of intensity similarity between the source and the target, tuning the transformation to maximize the similarity measure. Correct registration of the images will be the similarity maximum. Intensity-based registrations match intensity patterns over the whole image but do not use anatomical knowledge. Geometric registration uses anatomical information but usually sparsely distributed throughout the images. Combining geometric features and intensity features in registration should result in more robust methods. Hybrid algorithms are therefore of particular current interest, combining intensity-based and model-based criteria to establish more accurate correspondences in difficult registration problems [75].

Components of registration algorithms As illustrated in figure Figure 6.1 a registration algorithm can be decomposed into three components:

- The similarity metric measuring the image matching quality;
- The transformation model, which specifies the way in which the moving image can be changed to match the fixed image. A number of numerical parameters specify a particular instance of the transformation;
- The optimization process that searches in the transformation model parameter space to optimize the matching criterion.

6.2.1. Similarity measures

Regardless of the particular images, the used registration method, and the application area, it is highly desirable to provide the user with an estimate registration accuracy. Registration accuracy evaluation is a non-trivial problem, partially because the errors can be dragged into the registration process in each of its stages and partially because it is hard to distinguish between registration inaccuracies and actual physical differences in the image contents[119][150].

We use two well known [189] similarity metrics: the intensity mean squared differences (MSD) and Mutual Information (MI) [11, 10][173] [130]. These similarity metrics have each been used widely in the past for nonrigid registration, to measure the intensity agreement between a deforming image and the target image.

- The MSD is a suitable similarity metric when the images have been acquired by similar sensors, thus they are expected to present the same intensity range and distribution. For voxel sites \mathbf{x}_A in image A lying in an overlap region of the image domains $\Omega_{A,B}^T$ comprising N voxels:

$$MSD = \frac{1}{N} \sum_{x_A \in \Omega_{A,B}^T} (A(x_A) - B^T(x_A))^2 \quad (6.1)$$

- The MI is a measure of how much information one random variable has about another. The information contributed by the images is simply the entropy of the portion of the image that overlaps with the other image volume, and the mutual information is a measure of the joint entropy respect to the marginal entropies.

$$I(A, B) = H(A) + H(B) - H(A, B) \quad (6.2)$$

where $I(A, B)$ is the mutual information, $H(A)$ and $H(B)$ are the marginal entropies of the fixed and moving images and $H(A, B)$ is the joint entropy.

6.2.2. Transformation models

A spatial transformation maps each point in the 3D image domain into another point in the same space. The transformation model defines how one image can be deformed to match another; it characterizes the type and number of possible deformations. The best known example is the rigid or affine transformation that can be described very compactly by between 6 (3 translations and 3 rotations) and 12 (6 + 3 scalings + 3 shears) parameters for a whole image. These parameters are applied to a vector locating a point in the fixed image domain to predict its location in the moving image domain (forward transformation), or the location of the moving image point in the domain of the fixed image (backward transformation).

The transformation model serves two purposes; first it controls how image features can be moved relative to one another to improve the image similarity and second it interpolates between those features where there is no usable information. Transformations used in non-rigid registration range from smooth regional variation described by a small number of parameters [186] to dense displacement fields defined at each voxel [76]. One of the most important class of transformations is the linear combination of splines that have been used in various forms for around 15 years. The thin-plate spline (TPS) is an important tool for medical image registration. TPS can be considered to be a natural non-rigid extension of the affine map through minimizing a bending energy based on the second derivative of the spatial mapping [18]. Spline-based registration algorithms use corresponding (“control”) points, in the source and target image and a spline function to define correspondences away from these points. B-spline based non-rigid registration techniques [157] are popular due to their general applicability, transparency and computational efficiency. Their

main disadvantage is that special measures are sometimes required to prevent folding of the deformation field and these measures become more difficult to enforce at finer resolutions. Such problems have not prevented these techniques finding widespread use (in the brain, the chest, the heart, the liver, the breast etc. Diffeomorphic Registration is also another type of widely used registration method in medical image analysis. It seeks an invertible function smoothing and mapping one differentiable manifold (image) into another [139] [172].

6.2.2.1. Rigid Registration

For three dimensional images, such as CTA images, rigid body transformations have 6 degrees of freedom, consisting in the spatial translation $\mathbf{t} = [t_x, t_y, t_z]$ parameters and the rotation angles α , β and γ about these three axes, composed in a rotation matrix R . For a given point $\mathbf{x} \in \mathbb{R}^3$, a rigid body transformation T is given by the following expression:

$$T(\mathbf{x}) = R\mathbf{x} + \mathbf{t} \quad (6.3)$$

This transformation is appropriate for registration of rigid structures like bones [2] [101].

6.2.2.2. Affine Registration

While a rigid transformation preserves the distances between all points in the object transformed, an affine transformation preserves parallel lines. This model has 12 degrees of freedom, allowing for scaling and shearing. Let $\mathbf{x} = (x, y, z)^T$, the model can be expressed in extended coordinates as:

$$T(x, y, z) = \begin{pmatrix} x' \\ y' \\ z' \\ 1 \end{pmatrix} = \begin{pmatrix} a_{00} & a_{01} & a_{02} & a_{03} \\ a_{10} & a_{11} & a_{12} & a_{13} \\ a_{20} & a_{21} & a_{22} & a_{23} \\ 0 & 0 & 0 & 1 \end{pmatrix} \begin{pmatrix} x \\ y \\ z \\ 1 \end{pmatrix} \quad (6.4)$$

This transformation has been successfully applied in registration of free-form surfaces [54], registration of SPECT brain images [145], vascular atlas formation using a vessel-to-image registration [35] and four-dimensional registration models for respiratory-gated PET [86].

6.2.2.3. Deformable Registration

We give some details of a B-spline deformable transform [31, 32] because it has been used in our experiments below, for fine non-linear registration after the affine registration. Free Form Deformations (FFD) based in locally controlled functions such as B-splines are a powerful tool for modeling 3D deformable objects. A spline based FFD is defined on the image domain

$$\Omega = \{(x, y, z) \mid 0x < X, 0 \leq y < Y, 0 \leq z < Z\} \quad (6.5)$$

where Ω denotes an $n_x \times n_y \times n_z$ mesh of control points with uniform spacing δ . In this case, the displacement field $u(x, y, z)$ defined by FFD can be expressed as the 3D tensor product of 1D cubic B-splines:

$$u(x, y, z) = \sum_{l=0}^3 \sum_{m=0}^3 \sum_{n=0}^3 \Theta_l(u) \Theta_m(v) \Theta_n(w) \Phi_{(i+l, j+m, k+n)} \quad (6.6)$$

where

$$i = \left\lfloor \frac{x}{\delta} \right\rfloor - 1, j = \left\lfloor \frac{y}{\delta} \right\rfloor - 1, k = \left\lfloor \frac{z}{\delta} \right\rfloor - 1, u = \frac{x}{\delta} - \left\lfloor \frac{x}{\delta} \right\rfloor, v = \frac{y}{\delta} - \left\lfloor \frac{y}{\delta} \right\rfloor, w = \frac{z}{\delta} - \left\lfloor \frac{z}{\delta} \right\rfloor$$

and Θ_l represents the l -th basis function of the b-splines:

$$\begin{aligned} \Theta_1(s) &= (1-s)^3/6 \\ \Theta_2(s) &= (3s^2 - 6s^2 + 4)/6 \\ \Theta_3(s) &= (-3s^2 + 3s^2 + 3s + 1)/6 \\ \Theta_4(s) &= s^3/6 \end{aligned}$$

This transformation has been applied with good results in the implementation of an algorithm for targeted prostate cancer radiotherapy [175], registration of respiratory correlated CT images of lung cancer patients [123], breast MR images registration [47] and in spatio-temporal tracking of myocardial deformations [78].

6.2.3. Optimization

The search for the parameters values of the true transformation between the fixed and the moving image is performed in the parameter space following an optimization of the image similarity, either maximization or minimization. The optimizer is the

search algorithm used to perform such search. The landscape of the image similarity is plagued by the existence of local optima, so that finding the global optimum is usually infeasible. Therefore, optimizers look for the best local optimum or global suboptimum that they can provide in a reasonable amount of time. In other words, a good optimizer is one that reliably and quickly finds the best possible transformation.

Choosing a good optimizer requires a good understanding of the registration problem, the constraints that can be applied and knowledge of numerical analysis. Optimization in non-rigid registration applications is a more difficult problem than in affine registration because the number of parameters to estimate is much bigger, so it is the dimension of the search space, causing the appearance of many local optima, so that the difficulty of finding a good suboptimal solution (global minima may be almost impossible) is increased.

A more subtle problem is that a transformation parameter estimation that gives a good local optimum value of the feature similarity may not be physically meaningful. For example, we have a prior belief that the registration of one image onto another should be diffeomorphic [171]; in simple terms this means that if the transformation were applied to a real physical object to deform it then no tearing of the object would occur. Tearing can often result in a transformation that makes the images more similar despite it being physically invalid. Therefore in many situations, e.g. serial MRI brain registration of a subject undergoing diffuse atrophy, there is a prior expectation that folding or tearing should not be required to secure a good match. Often, object tearing results from correspondence problems. For instance, intersubject brain registration where one subject has a large extrinsic tumor [117], or registration of abdominal regions where fluid and gas filled spaces can appear and disappear between scans [187] are examples where correspondence is not well defined and where tearing or folding may be necessary to describe the underlying physical transformation. Other constraints can be implicit in the choice of the transformation model, e.g. that the transformation should be consistent with the behavior of a deforming elastic body. Much of the work of optimizers is therefore to balance the competing demands of finding the best set of correspondences subject to application-specific constraints.

Gradient based methods are realized for low and medium dimensional parameter spaces [100], when the similarity can be expressed functionally in terms of the transformation parameters. Gradient descent can be performed by some of the conventional numerical methods, such as Newton method [13], or Lavenberg-Marquard [132]. We can find applications of this method in multi modality image registration [64] like the registration of CT and intraoperative 3-D ultrasound images of the spine [185], 3-D/2-D registration of CT and MR to X-ray images [110] and rigid registration of 3-D ultrasound with MR images [134]

Random search methods, such as Genetic Algorithms [63] have been used for a robust 3-D MR-CT registration [136], while Simulated Annealing [163] shows a

good performance for registration of stereo and temporal images of the retina [133], automatic retinal image registration [111]. Wang et al. proposed a graph matching method based on mean field theory for computed tomographic colonography (CTC) scan registration [176]. We can find Particle Filtering applications in rigid shape-based surface registration [103], ultrasound to CT bone surface registration [116] and magnetic resonance prostate imagery [59]. These methods are applied when there is no such functional expression that can be differentiated, or the number of parameters is too big to manage by conventional numerical methods.

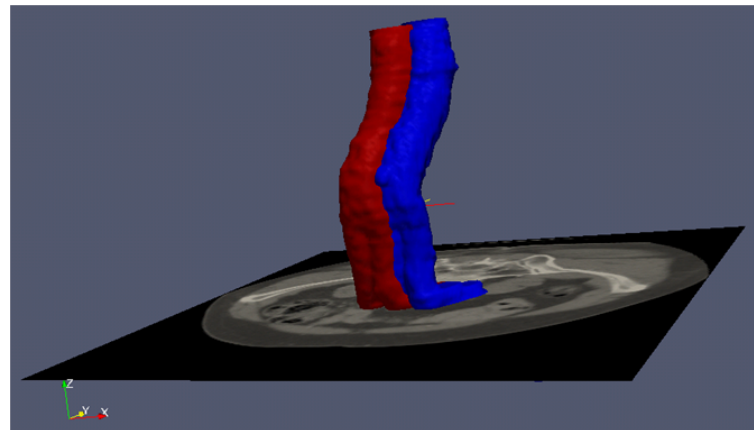
6.3. Aorta's Lumen Registration

First the two binary images corresponding to the patient lumen are roughly aligned by using a transform initialization and then the two images are registered using a rigid transformation. Figures Figure 6.2, Figure 6.3, and Figure 6.4 show examples of the results obtained by the proposed registration process. We apply an intra-subject and mono-modal registration of the same patient in different dates. A sequence of rigid, affine and deformable (B-splines) registrations is performed. We use FFDs to deform the lumen by manipulating an underlying mesh of control points. The resulting deformation controls the shape of the lumen and produces a smooth and continuous transformation. The earliest CT volume is considered the reference image and the others are registered relative to it. A linear interpolator, Mutual Information metric and Regular Step Gradient Descent Optimizer are used.

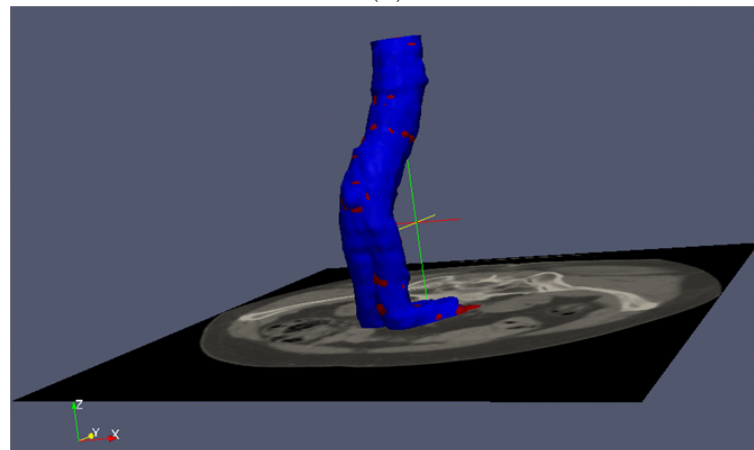
We have computed the MSD and MI similarity metrics for the evaluation of the registration in 3 registration processes performed on the data from the same subject, each of them consisting of rigid, affine, coarse-deformable and fine-deformable methods. A decrease of both metric is observed in the consecutive registration methods. MI reports include a negative number because traditionally that has been used as a cost function for minimization. Table Table 6.2 provides the quantification of the these similarities.

6.4. Thrombus co-registration

We have developed a method that places the thrombi of different datasets of the same patient referenced to the lumen of the first dataset. The registration process provides the transformation parameters that allow to transform the thrombus of the moving images to the same reference system of the fixed image, so that it becomes possible to compare the volume changes and deformation of the thrombus. Figure Figure 6.5 illustrates this process. Figure Figure 6.5(a) shows the thrombus of the fixed and moving image each one referred to its own aortic lumen. Figure Figure 6.5(b) shows the overlapping of the moving image thrombus and the fixed image thrombus. The method allows detecting small changes in volume or deformation of the thrombus



(a)



(b)

Figure 6.2.: 3D rendering of the segmented Aorta's lumen of patient #1 of the fixed and moving image (a) before and (b) after registration

that may go unnoticed for radiologists while comparing individual slices of the same patient along time. With this method, changes in thrombus's volume can be detected easily, such as the ones visualized in figure Figure 6.6.

6.5. Conclusions

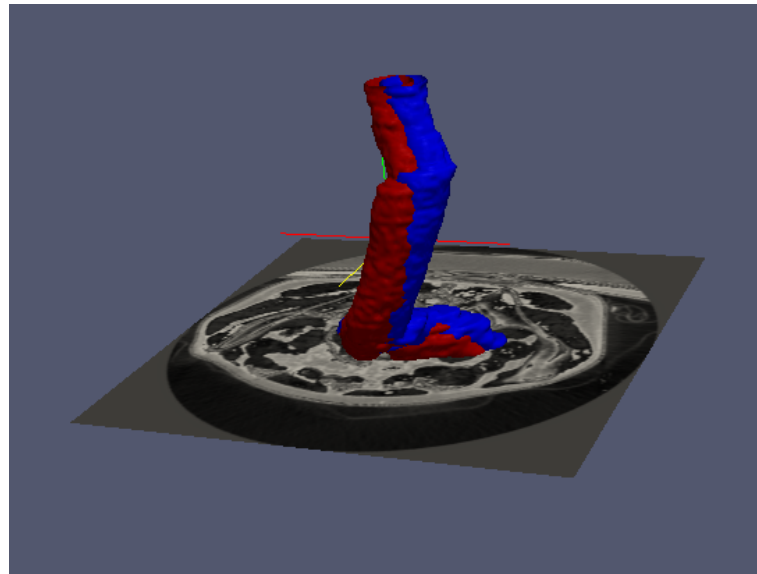
Co-registration of the thrombus of the aneurysm sac can provide a powerful visualization tool that may allow early detection of negative evolution of the EVAR treatment. Visualizations of several patients data provide empirical confirmation to this idea.

Besides, obtaining quantitative values of the changes in the thrombus after register images from different studies of the same patient, leads to consider predictive models of the evolution of other patients, providing quantitative measurements for decision

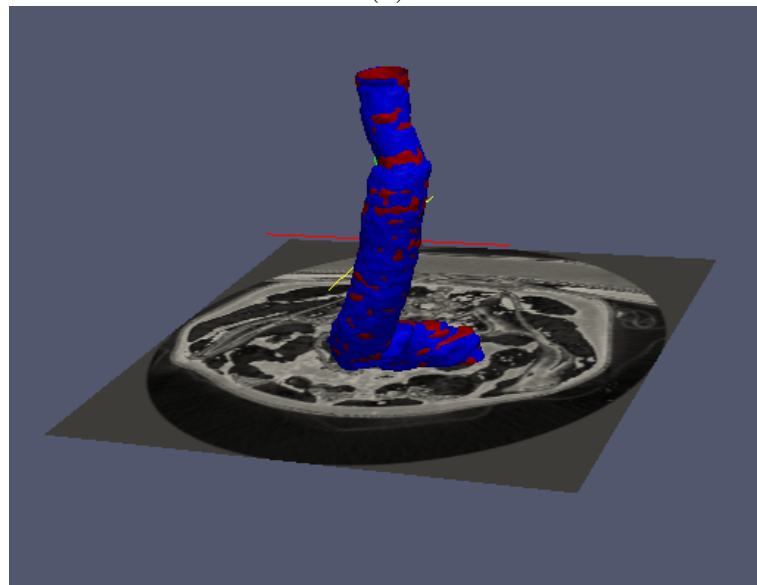
Registered Studies		Metric	
		MSD	MI
#2-#3	Rigid	4,60E-01	-5,28E-06
	Affine	3,42E-01	-7,25E-06
	Deform. Coarse	3,05E-01	-8,35E-06
	Deform. Fine	2,88E-01	-9,24E-06
#2-#4	Rigid	4,94E-01	-4,96E-06
	Affine	2,97E-01	-7,91E-06
	Deform. Coarse	2,70E-01	-8,64E-06
	Deform. Fine	2,65E-01	-9,53E-06
#2-#5	Rigid	8,03E-01	-3,48E-06
	Affine	3,73E-01	-6,29E-06
	Deform. Coarse	3,19E-01	-7,27E-06
	Deform. Fine	2,88E-01	-8,96E-06

Table 6.2.: Similarity metric results of the sequence of registrations over dataset pairs of one patient. Image #2 of the study is the fixed image for registration of moving images #3, #4 and #5.

support. Machine Learning approaches will be used to determine if the evolution of the EVAR is positive or not. These data would be integrated into a more complex database, where information about patients and monitored aneurysms may be available for comparative studies.

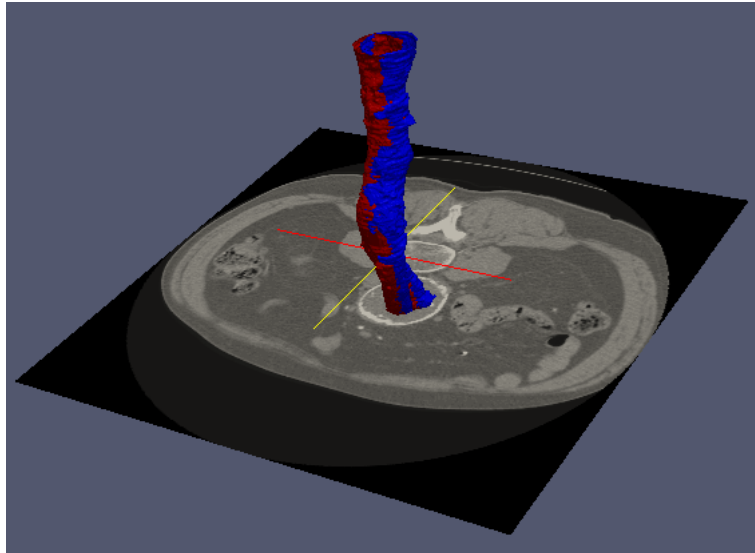


(a)

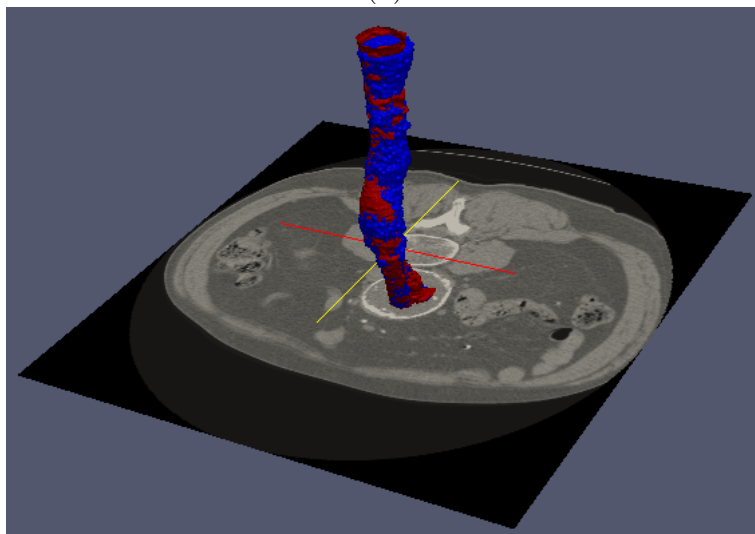


(b)

Figure 6.3.: 3D rendering of the segmented Aorta's lumen of patient #2 of the fixed and moving image (a) before and (b) after registration

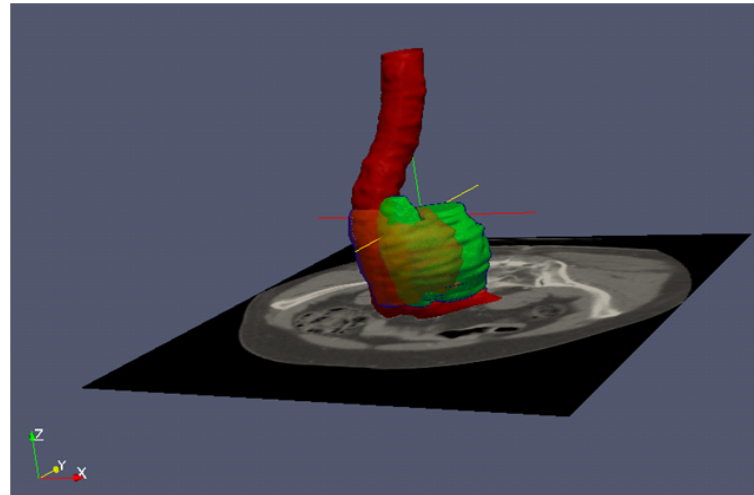


(a)

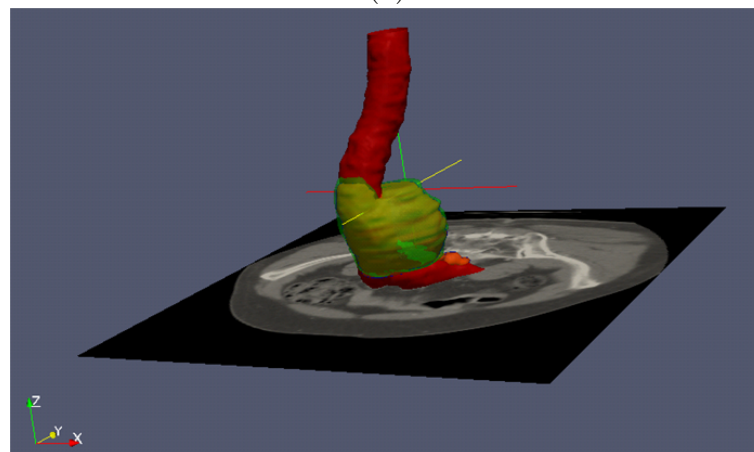


(b)

Figure 6.4.: 3D rendering of the segmented Aorta's lumen of patient #3 of the fixed and moving image (a) before and (b) after registration

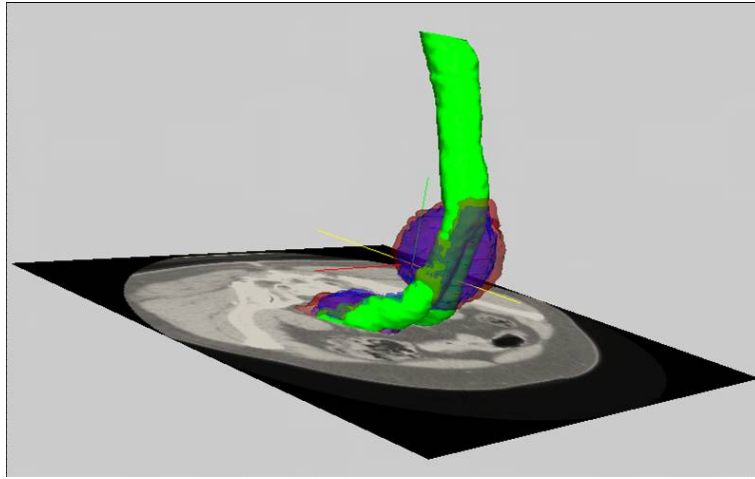


(a)

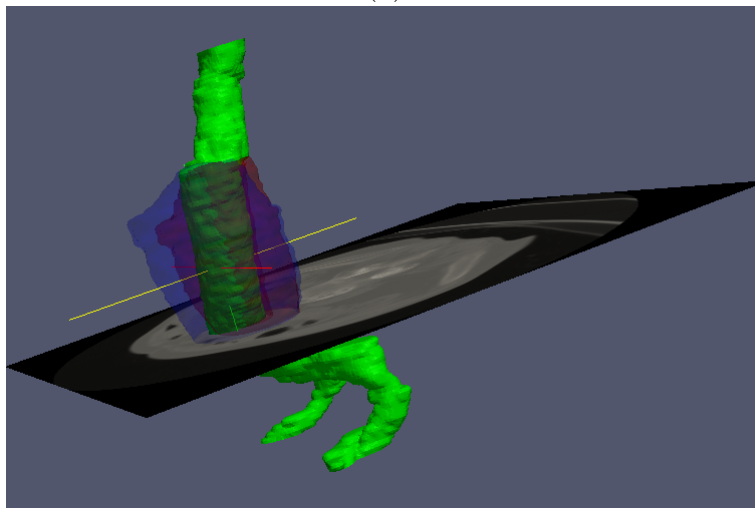


(b)

Figure 6.5.: Thrombus extracted for two points in time (semi-transparent orange for the first one, semi-transparent green the second one). (a) each thrombus is registered according to its correspondent segmented lumen, (b) both thrombi are referenced to the lumen of the first point in time, so the evolution of the aneurysm sac is highlighted.



(a)



(b)

Figure 6.6.: Thrombus extracted for two CT datasets obtained in two points in time (semi-transparent blue for the first one, semi-transparent red the second one), both referenced to the lumen of the first point in time. (a)It can be seen an increase in thrombus volume corresponding to an enlargement of the aneurysm sac. (b)In this case it can be seen a decrease in thrombus volume

7. Computer Aided Diagnosis

Cardiovascular diseases involving heart and blood vessels are the main causes of death in the western countries. Abdominal Aortic Aneurysms (AAA) is one of such diseases. This chapter describes the work done in this thesis to explore the construction of Computer Aided Diagnosis (CAD) systems to predict the evolution of the aneurysm in patients treated with an endovascular prostheses. These CAD systems are built on features obtained from image registration techniques. The aim of this work is to make a semi-automatic analysis of the AAA using digital image processing techniques, yielding visual and quantitative information for monitoring and tracking of patients who underwent EVAR, aiming to classify their evolution as favorable or unfavorable.

The contents of the chapter are the following: Section 7.1 gives some medical background on endovascular repairs. Section 7.2 introduces CAD systems. Section 7.3 presents the computational pipeline in detail. Section 7.4 presents results of the proposed CAD system on a specific dataset. Section 7.5 gives the conclusions of the chapter.

7.1. Endovascular Repair

The use of the endovascular prostheses for aneurysm repair (EVAR) has proven to be an effective technique to reduce the pressure and rupture risk of aneurysms, offering shorter post-operation recovery than open surgical repair. The EVAR isolates the dilated aorta vessel walls from the high pressure flow in the Aorta's lumen. In treated patients with positive evolution, the thrombus sac between the EVAR and the vessel wall is reabsorbed after a time. EVAR evolution monitoring main instruments are Computerized Tomography (CT) images of the abdominal region after injection of an intravenous contrast agent. The main concern is that there may be leaks into or from the thrombus sac due to incorrect positioning, displacement or torsion of the EVAR graft, that is, liquid blood may filter back from the Aorta's lumen inside the thrombus. This effect is called an endoleak and it can be detected by image analysis procedures [104]. Fig. 7.1(a) is a typical slice of the CT volume, while Fig. 7.1(b) shows a sagittal view of the volume with the segmented aorta, stent-graft and thrombus. Such images of the patient's abdominal area are available in the clinical routine as a stack of 2D images whose visual analysis is time-consuming. The majority of previous image processing methods for EVAR evolution monitoring

dealt with lumen and thrombus segmentation problems [162, 161][122][202]. Few works have addressed the lumen registration to estimate the deformation of the stent [112, 46].

7.2. Computer Aided Diagnosis systems

Decision support systems have a growing importance in the clinical routine, becoming Computer Aided Diagnosis (CAD) systems which CAD provide an effective way improve diagnosis accuracy, reducing tiredness and stress effects on the medical decisions, by combining elements of digital image processing, machine learning, pattern recognition, and domain knowledge of medicine [89][49]. It is used in a variety of diseases (i.e. cancer[164], neurological diseases [129], vascular diseases [147]) but the design and optimization is specific for each case.

Often, the initial component of image interpretation and diagnosis is the identification anatomical structures in the image. Afterwards, according to their position, shape, texture and/or evolution through time, they are classified as favorable or unfavorable. Artificial neural networks [65, 73] have become a standard tool for the development of computational decision support systems from data. They have been applied to a number of medical classification tasks [98]. Among the desirable properties of artificial neural networks is their ability to perform complex pattern-recognition tasks and the fact that they do not require prior knowledge of diagnostic rules. Among the statistical classifiers, the SVM have become a standard tool for the development of CAD systems from data [24].

The aim of our work is to make an automatic analysis of the AAA, yielding visual and quantitative information for monitoring and tracking of patients who underwent EVAR, allowing classifying their evolution as favorable or unfavorable. In this chapter we present a computer aided system for EVAR prognosis based on classification systems trained on the patient's data. Specifically, this data consists in the measurements of the deformation of the lumen between two different time instants obtained as the image registration quality measures. Visual rendering of AAA and EVAR transformation data can help the physician to recognize deformation patterns having a high probability of dangerous progression of the EVAR and the aneurysm. The quantitative features for the classification systems are the values of similarity metrics obtained after rigid, affine and deformable registration of the aortic lumen.

The proposed system has two phases:

1. A pipeline of image registration processes
2. A classification system based on the image similarity metrics resulting from the image registration steps.

The image registration of AAA after EVAR treatment has already been presented in [108]. We test classification systems built using the standard SVM, with linear and

non-linear (RBF) kernels, and some ANN architectures: Multi-Layer Perceptron (MLP), and Radial Basis Function (RBF). As a general result, the diverse systems showed a moderate accuracy due to a moderate sensitivity, and high specificity. Best results were obtained with SVM classifiers. Specifically, the input to the artificial neural network is the result of the registration methods.

7.3. Computational pipeline

We have developed a method to measure the deformation of the segmented Aorta between two studies of the same patient using registration techniques. Figure 7.2 shows the computational pipeline.

In our approach, first we estimate the rigid motion of the lumen relative to the spinal cord as well as its deformation [113, 46]. Visual overlapping of such transformed data can help identifying deformation patterns having a high probability of dangerous progression of the aneurysm but, we need to quantify those data to use neural network classifiers. The aim of our research is to calculate the similarity metrics after rigid, affine and deformable registration of the aortic lumen after EVAR and to construct a classifier to make a prediction about future complications and disease progression based on these variables.

First, the lumen is segmented using a 3D region growing algorithm. After that, the registration of the lumen extracted from two datasets of the same patient obtained at different moments in time is computed and then, we quantify the deformations of the lumen computing the similarity metrics between the reference and the registered binary image after the different registrations steps: rigid, affine and deformable. Finally we classify them as favorable or unfavorable using a neural network .

7.3.1. Lumen Segmentation

Aorta's lumen segmentation is performed applying User-Guided Level Set Segmentation (UGLSS) [194], based on the well-known Region Competition [199] 3D active contour segmentation method to get the segmented image of the lumen. During the data preprocessing, probability maps are computed, by applying a smooth lower and upper threshold. This ensures that voxels inside the lumen have a positive value and voxels outside it have a negative value. We place a seed to initialize the evolving contour into the lumen and we establish the parameters that control the propagation velocity and curvature velocity. An evolving contour is a closed surface $C(t, u, v)$ parametrized by variables u, v and by the time variable t . The contour evolves according to the following partial differential equation (PDE):

$$\frac{\partial}{\partial t}C(t, u, v) = F\vec{N} \tag{7.1}$$

We compute the external force F by estimating the probability that a voxel belongs to the structure of interest and the probability that it belongs to the background at each voxel in the input image:

$$F = \alpha(P_{obj} - P_{bg}) + \beta_K \quad (7.2)$$

Figure Figure 7.3 shows an evolution of the closed surface from an initial seed put inside the region of interest.

The spinal cord is also segmented as it is often used to place in the same reference system when comparing different datasets of the same patient. Figure Figure 7.4 shows the 3D rendering of the segmentation of both spinal cord and Aorta's lumen.

7.3.2. Quantification of Abdominal Aortic Deformation after EVAR

A sequence of three registration steps is performed:

1. rigid registration,
2. affine registration and
3. deformable registration (B-splines).

The segmented lumen of the first study is considered as the fixed image and the others are registered relative to it. A linear interpolator, Mutual Information (MI) metric, and Regular Step Gradient Descent Optimizer are used. Rigid, affine and deformable registration of the lumen allows for visual comparison of the evolution of the stent-graft.

- First, the two images corresponding to the patient lumen are roughly aligned by using an interactive registration initialization.
- Second, the two images are registered using a rigid transformation.
- Third, the rigid transformation is used to initialize a registration with an affine transform of the stent-graft.
- Fourth, the transform resulting from the affine registration is used as the bulk transform of a B-Spline deformable transform, and finally
- Fifth, the deformable registration is computed in two steps one at coarse resolution and refinement at fine resolution.

We use two similarity metrics: the mean of squared intensity differences (MSD) and mutual information MI. These similarity metrics have been used widely for non-rigid registration to measure the intensity agreement between a deformed source image and the fixed target image. We show in table Table 7.1 the measurements obtained

for the available datasets. The contents of table Table 7.1 summarize the dataset used for the classification experiments below.

7.3.3. Learning Algorithms

Chapter 4 provides a review of the Learning Algorithms that have been applied here, as well in other chapters of the Thesis. In this section we give some summary comments on the way these algorithms have been applied to AAA evolution prediction.

Problem Statement We deal with a two class classification problem, given a collection of training/testing input feature vectors $X = \{\mathbf{x}_i \in \mathbb{R}^n, i = 1, \dots, l\}$ and the corresponding labels $\{y_i \in \{-1, 1\}, i = 1, \dots, l\}$, which sometimes can be better denoted in aggregated form as a binary vector $\mathbf{y} \in \{-1, 1\}^l$. Our aim is to classify the patients as those who have a favorable or unfavorable evolution.

Learning algorithms The specific features of the learning algorithms applied in this chapter are as follows:

- SVM: we have tested SVM with linear and RBF kernels. The regularization parameter C is always set to 1 in this case study. Gamma is set to 0.01 in the RBF kernel.
- LVQ: The learning rate is set to 1. The number of clusters is set to 2.
- MLP trained with BP algorithm. The number of hidden layer is given by the wildcard value 'a' = (attribs + classes) / 2. In our case its value is 5. The learning rate was set to 0.3.
- Random Forest: we set the number of trees to 10. The number of attributes to be used in random selection is 2. The maximum depth of the the trees is not limited

We perform the classification in the Weka environment [67].

Methodology A leave-one-out process has been carried out to estimate generalization performance of the classifiers, due to the small sample size.

	Data1	Data2	Data3	Data4	Data5	Data6	Data7	Data8	Data9	Data10
MSD_R	4,60E-01	4,94E-01	8,03E-01	8,93E-01	1,29E+00	1,63E+00	1,25E-03	1,16E-03	4,12E-03	1,56E-03
MSD_A	3,42E-01	2,97E-01	3,73E-01	5,33E-01	7,06E-01	1,06E+00	1,23E-03	1,19E-03	4,12E-03	1,30E-03
MSD_CD	3,05E-01	2,70E-01	3,19E-01	4,43E-01	5,23E-01	6,96E-01	8,60E-04	9,80E-04	4,08E-03	8,28E-04
MSD_AD	2,88E-01	2,65E-01	2,88E-01	3,70E-01	4,41E-01	5,09E-01	9,69E-04	9,80E-04	4,19E-03	8,53E-04
MI_R	-5,28E-06	-4,96E-06	-3,48E-06	-2,71E-06	-1,34E-06	-9,62E-07	-4,50E-06	-4,75E-06	-9,41E-07	-6,10E-06
MI_A	-7,25E-06	-7,91E-06	-6,29E-06	-4,87E-06	-3,45E-06	-1,92E-06	-4,42E-06	-4,67E-06	-9,84E-07	-6,54E-06
MI_D	-8,35E-06	-8,64E-06	-7,27E-06	-5,58E-06	-5,00E-06	-3,93E-06	-5,66E-06	-5,68E-06	-1,32E-06	-8,28E-06
MI_AD	-9,24E-06	-9,53E-06	-8,96E-06	-6,96E-06	-6,49E-06	-5,87E-06	-5,40E-06	-5,68E-06	-1,14E-06	-8,22E-06

Table 7.1.: Similarity metrics for rigid (R), affine (A), coarse deformable (CD) and affine deformable (AD), measured with mean squared differences (MSD) and mutual information (MI). Rows are coded as (transformation_metric) Data1..n, are pairs of studies of the same patient obtained in different points in time.

Classifier	Accuracy	Sensitivity	Specificity	AUC
Linear SVM	0.72	0.75	0.67	0.97
RBF SVM	0.77	0.80	0.70	0.98
LVQ	0.80	0.86	0.72	0.76
BP- MLP	0.73	0.71	0.80	0.97
Random-Forest	0.91	0.99	0.73	0.99

Table 7.2.: Leave-one-out cross-validation results of EVAR evolution classification performed over the similarity metric features computed from the available CT datasets.

7.4. Results

7.4.1. Datasets

We have tested the approach with 15 datasets corresponding to 5 patients which have been treated with stent-graft devices. 4 datasets, corresponding to 1 patient, are validated by the doctors as having a favorable evolution and 11, corresponding to 4 patients, as unfavorable, according to aneurysm volume and surface measures, as well as blood leakages in the aneurysm sac. The CT image stacks consists of datasets obtained from a LightSpeed16 CT scanner (GE Medical Systems, Fairfield, CT, USA) with 512x512x354 voxel resolution and 0.725x0.725x0.8 mm. spatial resolution. The time elapsed between different studies of the same subject ranges between 6 and 12 months. We have computed the MSD and MI similarity metrics for the evaluation of the registration. A decrease of dissimilarity is observed in the consecutive registration methods as shown in figure Figure 7.5.

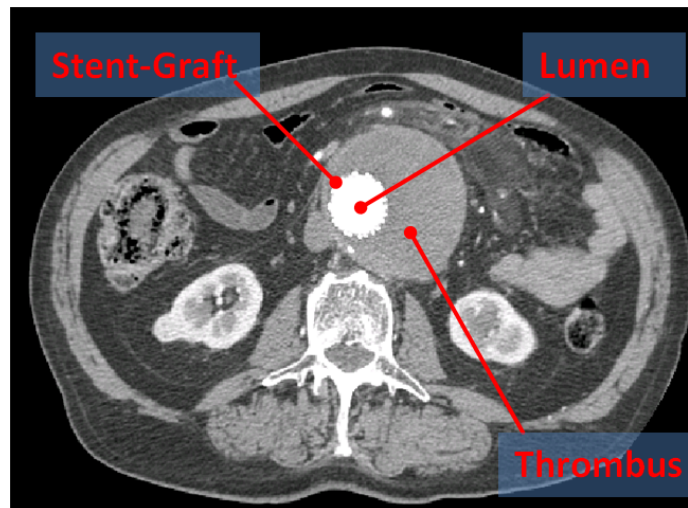
We build the input feature vectors with the values of the similarity measures after different registration modalities for each pair of segmented lumen images. So, we have 8 features for each registered image pair, 4 computing the MSD dissimilarity and 4 computing the MI similarity between the pair

Results We train over the set of features different classifiers and we show the results for accuracy, sensitivity, specificity, and area under the ROC (AUC). Table Table 7.2 gives average results from on a one-leave-out cross-validation strategy on this database. We obtain the best results for Random-Forest, followed by LVQ and RBF-SVM while MLP-BP and Linear SVM, give us the less accurate results. Results are promising of high accuracy prognosis, needing confirmation on a larger patient population.

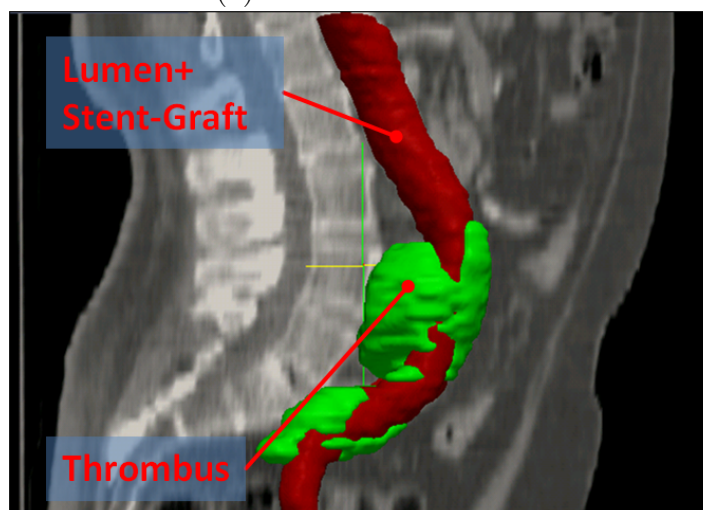
7.5. Conclusions

This chapter reports an approach to built CAD system for the prognosis of EVAR treated patients with AAA. Features for the CAD classifier are the the similarity measures of the segmented lumen after rigid, affine and deformable registration of the Aorta's lumen. The rationale is that registering images from different datasets of a patient may provide us quantified values of deformation of the stent-graft. The datasets of the patients have been previously validated by the medical team as having a favorable or unfavorable evolution.

Considering the average accuracy data achieved by most of the classifiers tested, our main conclusion is that the proposed feature extraction is very effective in providing a good discrimination between patients that can easily be exploited to build classifier systems predicting the evolution of other patients and provide support for the physician decision making. We have obtained very good results with a parsimonious set of features. Other approaches, such as using the deformation fields, would involve much more computational cost and the need to assess the dimensionality reduction appropriate for the problem. Our approach shows that simple summary information allows effective discrimination. Extensive validation of the approach requires the incorporation of additional datasets, which is a long term endeavor.



(a)



(b)

Figure 7.1.: (a) Axial view of thrombus and lumen in a CT orthoslice using the contrast agents, blood in lumen is highlighted for a better view. (b) 3D view of segmented lumen+stent-graft and thrombus localized over a sagittal CT image faded in.

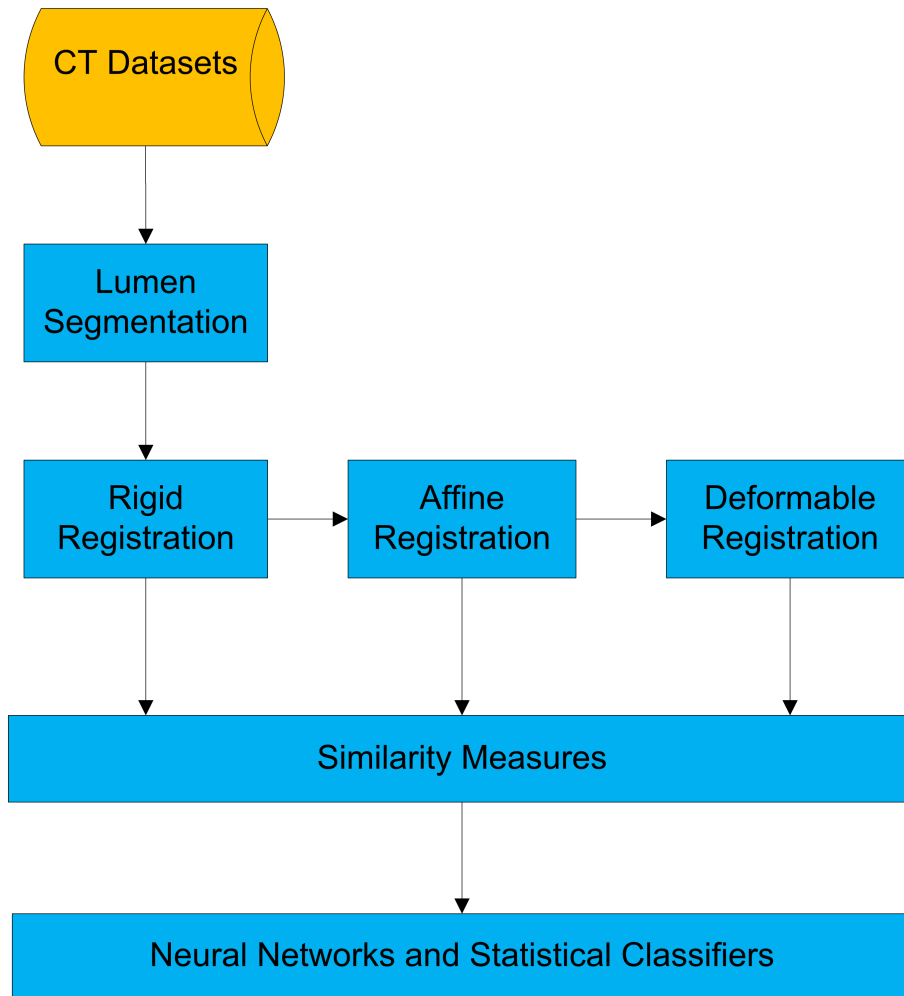


Figure 7.2.: Pipeline of the CAD system for EVAR evolution prediction from image data.

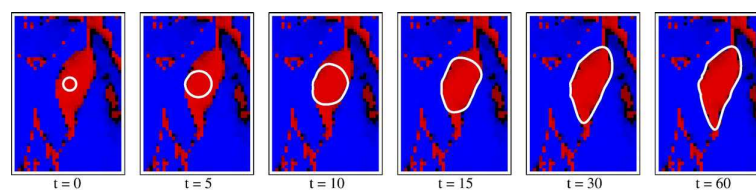


Figure 7.3.: Active contour evolution using the feature image based on region competition. The propagation force acts outwards over the “foreground” region (red) and inwards over the “background” region (blue), causing the active contour to reach equilibrium at the boundary of the regions.

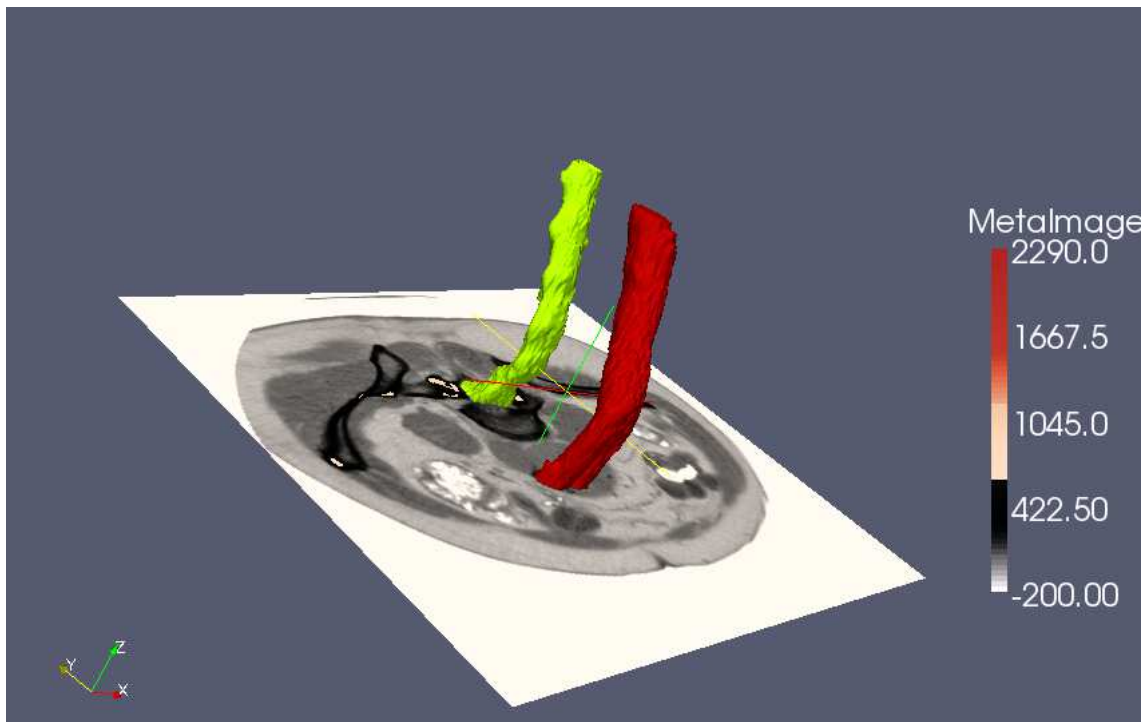
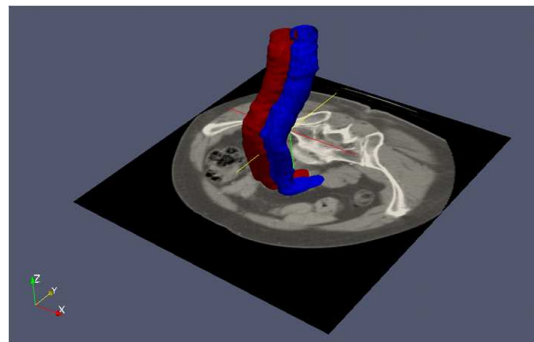
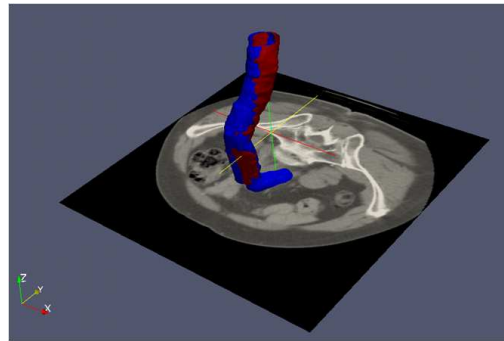


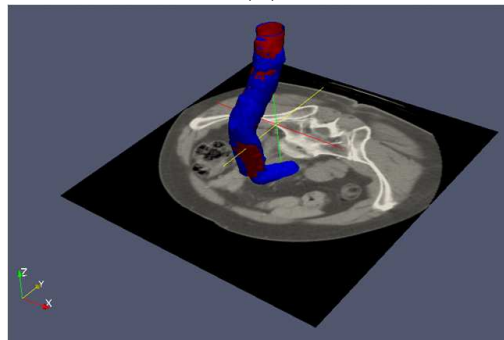
Figure 7.4.: Segmented spinal canal and lumen localized on a 3D CT slice.



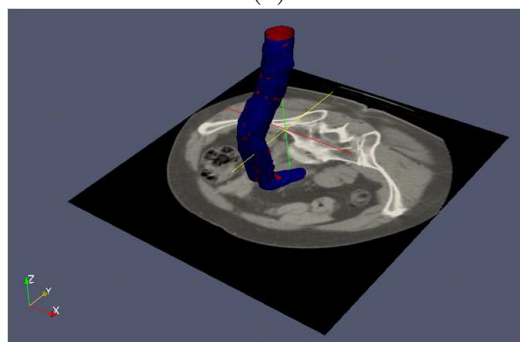
(a)



(b)



(c)



(d)

Figure 7.5.: Visualization of fixed and moving images of the lumen (a) before registration, (b) after rigid, (c) affine, and (d) deformable registration.

8. Conclusions and Future works

This chapter summarizes the conclusions of this Thesis and offers some lines for future works. The Thesis is focused in a specific application of medical imaging to a disease and treatment: the Abdominal Aortic Aneurysm (AAA) and its Endovascular Aneurysm Repair (EVAR). The motivation comes from the high prevalence of AAA in western population and the need to perform accurate follow-up of the treatment to prevent the associated risks. The collaboration with the clinicians actually treating the patients has been very positive, in the measure that they have provided real life data and some feedback on the results of the thesis, mainly about the visual assessment of thrombus evolution which has been found potentially useful at clinical practice level.

8.1. Conclusions

The Active Learning strategy for training classifiers performing the AAA's thrombus segmentation proposed in Chapter 5 has been validated on real life data obtaining high classification accuracy. As a measure of generalization capability, the classifier trained on the central slice of the CTA volume has been applied to the remaining slices. Generalization accuracy results are also remarkable. More extensive validation experiments are always desirable, needing recruitment of additional data from patients.

The longitudinal thrombus visualization procedure discussed in Chapter 6 has been demonstrated to the clinicians, with good acceptance, notwithstanding the lack of an easy-to-use tool to perform the pipeline process. The procedure has no critical parameters to tune, therefore is a robust procedure for daily used with little training requirements on the human operators.

The CAD system proposed in Chapter 7 has been validated on real clinical data, testing several state-of-the-art classifiers. Results are encouraging, the small sample size preventing to make claims of general applicability. However, as the process uses longitudinal data, it is quite possible that its application will be equally successful on new data.

8.2. Future works

The thrombus segmentation by Active Learning may be compared in terms of accuracy and usability with other state-of-the-art thrombus segmentation algorithms. The usability test involves the repeatability of results by several human operators, and the ease of use, sensitivity to the fine tuning of algorithm parameters, and other issues that affect the daily practice, so that a theoretically superior segmentation algorithm may be rather undesirable for clinical practice. Proposal of the technique for clinical practice implies the design and development of an appropriate visualization of classification uncertainty results as well as interaction means to explore the uncertainty 3D data.

In general, the segmentation of abdominal organs and tissues is an on-going research effort by many research teams. It poses many challenges: low contrast-to-noise ratio, anatomical variability, motion and other sources of noise, lack of a priori maps guiding the segmentation. Therefore, there is a wide open field to propose and test new algorithms and hybridization of the old ones. In this setting, Machine Learning approaches are getting increasingly relevant, providing sound methodology to validate proposals and compare results.

CAD approaches would ideally be desirable at the pre-operative imaging moment. That it, we would like to propose a tool helping the clinician to decide if the EVAR is the appropriate solution for a specific patient. That implies a large collection of data and experience gathered by the close collaboration with the clinicians. This CAD system must also be based on more general image features than the ones proposed in this Thesis, deriving from extensive *a priori* information possessed by the clinicians, but which is not easily quantified or expressed in computable terms.

A. Computer Tomography Datasets

In this appendix we describe the real life datasets used for the experimental works in this Thesis. Section section A.1 describes images provided by the Dr Mariano de Blas from the Hospital de Donostia. Section section A.2 describes the images provided by Dr. Joskowitz from Mount Sinai School of Medicine. Images are obtained after contrast injection, so that the blood flow appears as hiperintense voxel regions in the images.

A.1. Hospital Donostia Dataset

A.1.1. 16-row CT scanner

At the early stages of our research the medical research group working at the Hospital Donostia provided us with relatively low resolution images adquired with 16-row CT scanner. Each dataset is comprised between 50 and 100 axial slices that form a three dimensional image. The CT datasets were obtained from a Philips CT 7000 scanner (Philips Medical Systems) with 320x320 resolution and 1.094x1.094x3 mm. spatial resolution. The time elapsed between different studies of the same subject varies between 6 and 12 months. Figures Figure A.1(a) and Figure A.1(b) show an axial view and a coronal view of this dataset, respectively.

A.1.2. 64-row CT scanner

We have tested our methods with 15 datasets corresponding to 5 patients which have been subjected to EVAR with stent-graft devices. Each dataset is comprised between 300 and 500 axial slices that form a three dimensional image. The CT datasets were obtained from a LightSpeed VCT scanner (GE Medical Systems, Fairfield, CT, USA) with 512x512 pixel resolution per slice and 0.725x0.725x0.8 mm. spatial resolution. The time elapsed between different studies of the same subject varies between 6 and 12 months. Four datasets, corresponding to one patient, are validated by the doctors as having a favorable evolution and 11, corresponding to the remaining 4 patients, as unfavorable, according to aneurysm volume and surface measures, as well as blood leakages in the aneurysm sac. Figures Figure A.2(a) and Figure A.2(b) show an axial view and a coronal view of this dataset, respectively.

A.2. Mount Sinai School of Medicine (New York) Datasets

Patients were administered 100cc of non-iodinated contrast agent with a rapid injection aid at 3-4cc per sec. The CTAs consist of 512×512 pixels per slice with physical voxel sizes in the 0.7- 1.2mm range. The datasets included various sizes and locations of the thrombus. Some of them were acquired after stent placement, and thus include strong streaking artifacts. The datasets were acquired on a 64-row CT scanner (Brilliance 64 - Phillips Healthcare, Cleveland, OH) and were chosen randomly from the hospital archive to represent wide variety of patients with different ages. Figures Figure A.3(a) and Figure A.3(b) show an axial view and a coronal view of this dataset.

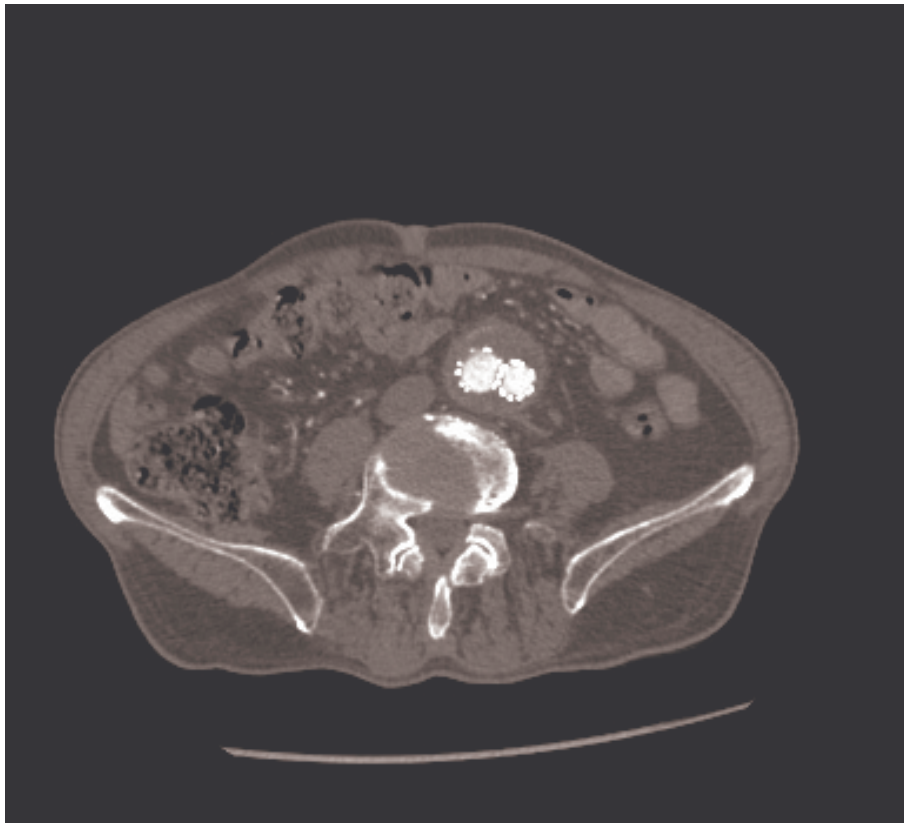


(a)

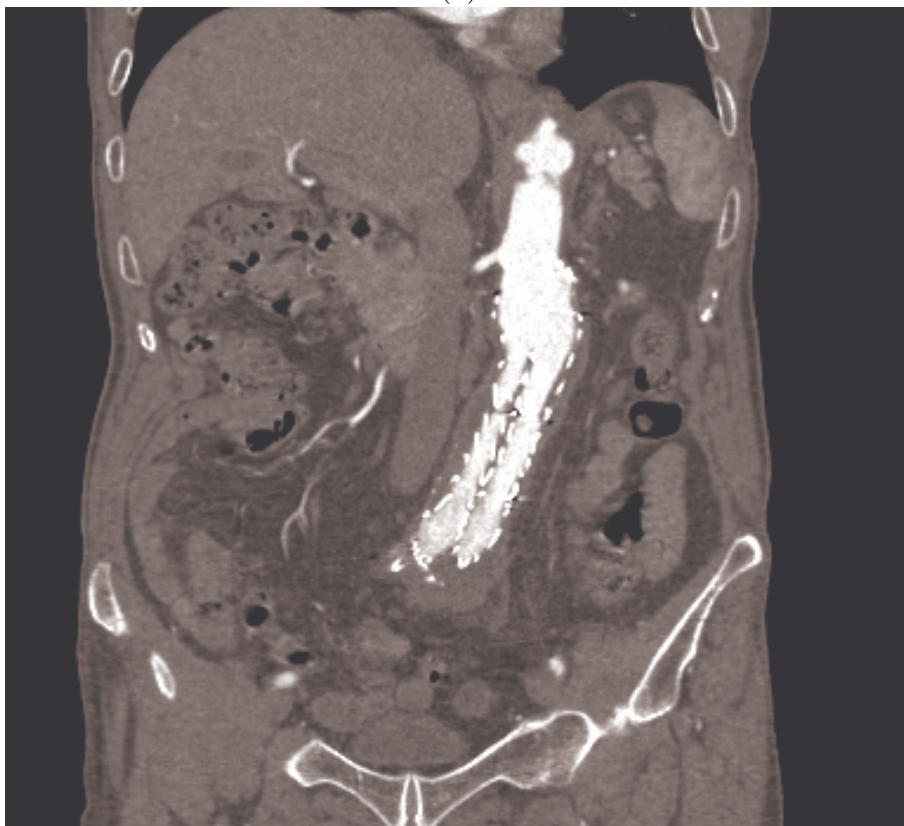


(b)

Figure A.1.: Low resolution CT image with contrast agent from Hospital Donostia.
(a) Axial view (b) Coronal view

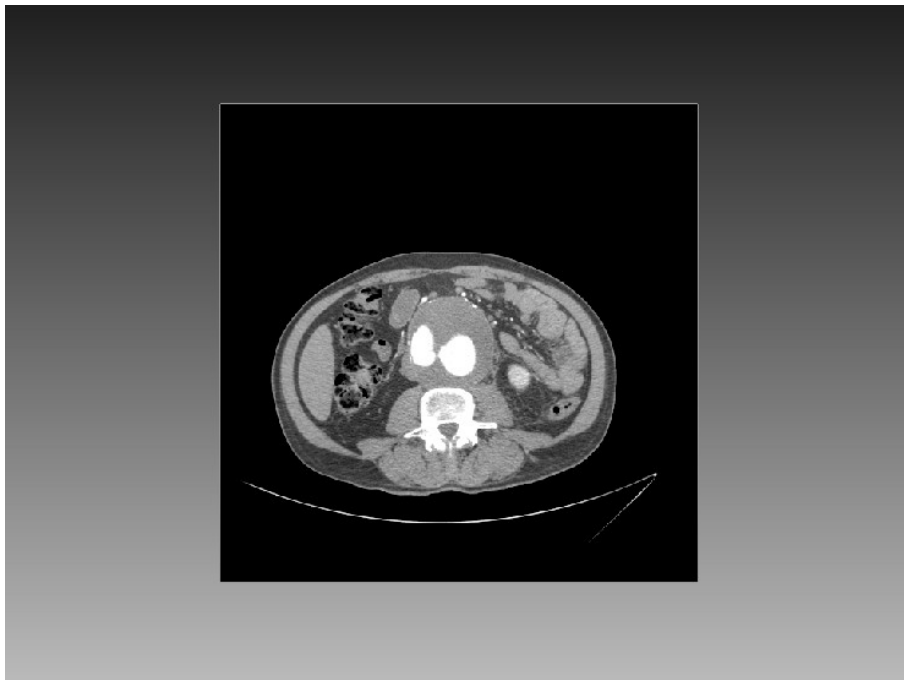


(a)

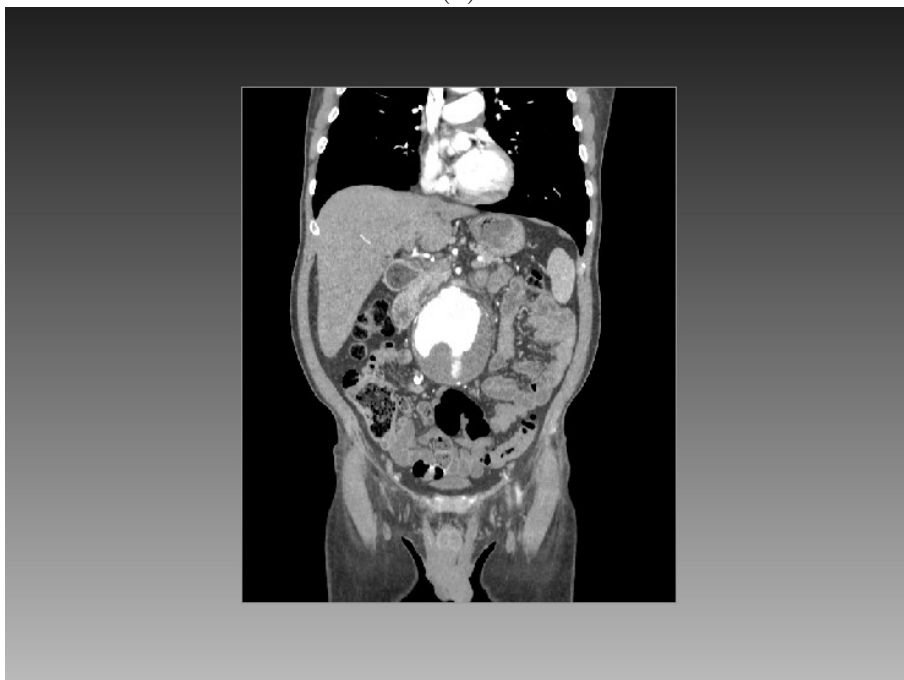


(b)

Figure A.2.: High resolution CT image with contrast agent from Hospital Donostia. (a) Axial view (b) Coronal view



(a)



(b)

Figure A.3.: Mount Sinai CT image with contrast agent. (a) Axial view (b) Coronal view

B. Insight Toolkit Software

B.1. Introduction

In this appendix we describe the software used for image processing, segmentation, and registration. Our applications are based in Insight Toolkit (ITK) open source software which can be downloaded without cost from <http://www.itk.org>. Through the ITK initiative from the National Library of Medicine (NLM), experts in the field of image processing have created a suite of state-of-the-art segmentation and registration algorithms ideally suited to volume visualization and analysis. Although it is large and complex, ITK is designed to be easy to use once you learn about its basic object-oriented implementation methodology.

B.2. Configuring ITK

This section describes the process for configuring ITK on our system. ITK is a toolkit, as such, once it is installed in our computer there will be no application to run. Rather, we will use ITK to build your own applications.

ITK is implemented in C++ and, has been developed and tested across different combinations of operating systems, compilers, and hardware platforms including MS-Windows, Linux on Intel-compatible hardware, Solaris, IRIX and recently the Mac. The toolkit is organised in a data-flow architecture: process objects (eg. filters) consume data objects (eg. images). We have installed it in MS-Windows hardware platform and compiled it with Visual Studio 2010.

The challenge of supporting ITK across platforms has been solved through the use of CMake, a cross-platform, opensource build system. CMake is used to control the software compilation process using simple platform and compiler independent configuration files. CMake generates native makefiles and workspaces that can be used in the compiler environment of your choice. CMake generates Visual Studio workspaces. The information used by CMake is provided by CMakeLists.txt files that are present in every directory of the ITK source tree. These files contain information that the user provides to CMake at configuration time. Typical information includes paths to utilities in the system and the selection of software options specified by the user. CMake can be downloaded at no cost from <http://www.cmake.org>.

B.3. ITK Modules

B.3.1. Data representation

The most common classes used by ITK for representing data are the Image, the Mesh and the Point Set class.

Image

ITK supports images with any pixel type and any spatial dimension. In ITK, images exist in combination with one or more *regions*. A region is a subset of the image and indicates a portion of the image that may be processed by other classes in the system.

The starting point of the image is defined by an Index class that is an n-dimensional array where each component is an integer indicating the grid coordinates of the initial pixel of the image. The region size is represented by an array of the same dimension of the image (using the Size class). The components of the array are unsigned integers indicating the extent in pixels of the image along every dimension.

Point Set

The Point Set class is a basic class intended to represent geometry in the form of a set of points in n-dimensional space. It is the base class for the Mesh class providing the methods necessary to manipulate sets of point. Points can have values associated with them.

Mesh

The Mesh class is intended to represent shapes in space. It derives from the Point Set class and hence inherits all the functionality related to points and access to the pixel-data associated with the points. The mesh class is also n-dimensional which allows a great flexibility in its use.

In practice a Mesh class can be seen as a Point Set to which cells (also known as elements) of many different dimensions and shapes have been added.

B.3.2. Filters

In this section we describe the most commonly used filters found in the toolkit. Most of these filters are meant to process images. They will accept one or more images as input and will produce one or more images as output. ITK is based on a data pipeline architecture in which the output of one filter is passed as input to another filter.

Thresholding

The thresholding operation is used to change or identify pixel values based on specifying one or more values (called the threshold value).

Edge Detection

The filter included in ITK for this purpose is the Canny Edge Detection. This filter is widely used since it is the optimal solution satisfying the constraints of good sensitivity, localization and noise robustness.

Casting and Intensity Mapping

Casting is used to convert one pixel type to another, while intensity mappings also take into account the different intensity ranges of the pixel types.

Gradients

Computation of gradients is a fairly common operation in image processing. The term “gradient” may refer in some contexts to the gradient vectors and in others to the magnitude of the gradient vectors. ITK filters attempt to reduce this ambiguity by including the magnitude term when appropriate. ITK provides filters for computing both the image of gradient vectors and the image of magnitudes

Second Order Derivatives: Laplacian Filters

In ITK we find the Laplacian Filter Recursive Gaussian. This filter applies the approximation of the convolution along a single dimension. It is therefore necessary to concatenate several of these filters to produce smoothing in all directions.

Neighborhood Filters

The concept of locality is frequently encountered in image processing in the form of filters that compute every output pixel using information from a small region in the neighborhood of the input pixel.

The Insight toolkit implements an elegant approach to neighborhood-based image filtering. The input image is processed using a special iterator. This iterator is capable of moving over all the pixels in an image and, for each position, it can address the pixels in a local neighborhood. Operators are defined so as to applying an algorithmic operation in the neighborhood of the input pixel they produce a value for the output pixel.

ITK implements some of the more commonly used neighborhood filters like mean and median filters along with mathematical morphology filters.

Smoothing Filters

Real image data has a level of uncertainty that is manifested in the variability of measures assigned to pixels. This uncertainty is usually interpreted as noise and considered an undesirable component of the image data. ITK implements several methods that can be applied to reduce noise on images, like gaussian blurring and anisotropic diffusion edge preserving smoothing.

Distance Map

ITK implements a filter that generates a distance map from the input image using the algorithm developed by Danielsson. As secondary outputs, a Voronoi partition of the input elements is produced, as well as a vector image with the components of the distance vector to the closest point. The input to the map is assumed to be a set of points on the input image. Each point/pixel is considered to be a separate entity even if they share the same gray level value.

Geometric Transformations: Resample Image Filter

Resampling an image is a very important task in image analysis. It is especially important in the frame of image registration. ITK implements image resampling through the use of geometric transformations. The inputs expected by this filter are an image, a transform and an interpolator. The space coordinates of the image are mapped through the transform in order to generate a new image. The extent and spacing of the resulting image are selected by the user. Resampling is performed in space coordinates, not pixel/grid coordinates.

Frequency Domain

ITK provides a base abstract class that implements the Fast Fourier Transform filter (FFT) for processing an image in the spectral domain.

One of the most common image processing operations performed in the Fourier Domain is the masking of the spectrum in order to eliminate a range of spatial frequencies from the input image. This operation is typically performed by taking the input image, computing its Fourier transform using a FFT filter, masking the resulting image in the Fourier domain with a mask, and finally taking the result of the masking and computing its inverse Fourier transform.

Extracting Surfaces

Probably the most widely known method of surface extraction is the Marching Cubes algorithm. ITK performs surface extraction using an algorithm similar to Marching Cubes.

B.3.3. Reading and Writing Images

ITK does not enforce any particular file format, instead, it provides a structure supporting a variety of formats that can be easily extended by the user as new formats become available.

When reading and writing images, the pixel type of the image is not necessarily the same as the pixel type stored in the file. Your choice of the pixel type should be driven mainly by two considerations:

- It should be possible to cast the file pixel type in the file to the pixel type you select. This casting will be performed using the standard C-language rules, so you will have to make sure that the conversion does not result in information being lost.
- The pixel type in memory should be appropriate to the type of processing you intended to apply on the images.

It is still quite common to store 3D medical images in sets of files each one containing a single slice of a volume dataset. Those 2D files can be read as individual 2D images, or can be grouped together in order to reconstruct a 3D dataset. ITK provides functionalities for dealing with reading and writing series of images.

ITK also provides functionalities for reading and writing DICOM files. This is extremely important in the domain of medical imaging since most of the images that are acquired in a clinical setting are stored and transported using the DICOM standard.

B.3.4. Segmentation Methods

The most effective segmentation algorithms are obtained by carefully customizing combinations of components. The parameters of these components are tuned for the characteristics of the image modality used as input and the features of the anatomical structure to be segmented. The Insight Toolkit provides a basic set of algorithms that can be used to develop and customize a full segmentation application. Some of the most commonly used segmentation components are described here.

Region Growing

Region growing algorithms have proven to be an effective approach for image segmentation. Several implementations of region growing are available in ITK. These are the most popular:

- **Connected Threshold:** A simple criterion for including pixels in a growing region is to evaluate intensity value inside a specific interval.
- **Otsu Segmentation:** Another criterion for classifying pixels is to minimize the error of misclassification. The goal is to find a threshold that classifies the image into two clusters such that we minimize the area under the histogram for one cluster that lies on the other cluster's side of the threshold. This is equivalent to minimizing the within class variance or equivalently maximizing the between class variance.
- **Neighborhood Connected:** this algorithm will only accept a pixel if *all* its neighbors have intensities that fit in the interval. The size of the neighborhood to be considered around each pixel is defined by a user-provided integer radius.
- **Confidence Connected:** The criterion used is based on simple statistics of the current region. First, the algorithm computes the mean and standard deviation of intensity values for all the pixels currently included in the region. A user-provided factor is used to multiply the standard deviation and define a range around the mean. Neighbor pixels whose intensity values fall inside the range are accepted and included in the region. When no more neighbor pixels are found that satisfy the criterion, the algorithm is considered to have finished its first iteration. At that point, the mean and standard deviation of the intensity levels are recomputed using all the pixels currently included in the region. This mean and standard deviation defines a new intensity range that is used to visit current region neighbors and evaluate whether their intensity falls inside the range. This iterative process is repeated until no more pixels are added or the maximum number of iterations is reached.

Watershed Segmentation

Watershed segmentation classifies pixels into regions using gradient descent on image features and analysis of weak points along region boundaries.

The filter implemented in ITK is actually a collection of smaller filters that modularize the several steps of the algorithm in a mini-pipeline. The segmenter object creates the initial segmentation via steepest descent from each pixel to local minima. Shallow background regions are removed (flattened) before segmentation using a simple minimum value threshold (this helps to minimize oversegmentation of the image). The initial segmentation is passed to a second sub-filter that generates a hierarchy of basins to a user-specified maximum watershed depth. The relabeler

object at the end of the mini-pipeline uses the hierarchy and the initial segmentation to produce an output image at any scale below the user-specified maximum. Data objects are cached in the mini-pipeline so that changing watershed depths only requires a (fast) relabeling of the basic segmentation.

Level-Set Methods

Level sets can be used for image segmentation by using image-based features such as mean intensity, gradient and edges in the governing differential equation. In a typical approach, a contour is initialized by a user and is then evolved until it fits the form of an anatomical structure in the image. Many different implementations and variants of this basic concept have been published in the literature.

These are some of the main level set segmentation methods available in ITK:

- **Fast Marching Segmentation:** when the differential equation governing the level set evolution has a very simple form, a fast evolution algorithm called fast marching can be used. The mapping should be done in such a way that the propagation speed of the front will be very low close to high image gradients while it will move rather fast in low gradient areas. This arrangement will make the contour propagate until it reaches the edges of anatomical structures in the image and then slow down in front of those edges.
- **Shape Detection Segmentation:** The implementation of this filter in ITK is based on the paper by Malladi et al. In this implementation, the governing differential equation has an additional curvature-based term. This term acts as a smoothing term where areas of high curvature, assumed to be due to noise, are smoothed out. Scaling parameters are used to control the tradeoff between the expansion term and the smoothing term. One consequence of this additional curvature term is that the fast marching algorithm is no longer applicable, because the contour is no longer guaranteed to always be expanding. Instead, the level set function is updated iteratively.
- **Geodesic Active Contours Segmentation:** The implementation of this filter in ITK is based on the paper by Caselles. This implementation extends the functionality of the *Shape Detection Segmentation* filter by the addition of a third advection term which attracts the level set to the object boundaries.

B.3.5. Registration Framework

In ITK, registration is performed within a framework of pluggable components that can easily be interchanged. This flexibility means that a combinatorial variety of registration methods can be created, allowing users to pick and choose the right tools for their specific application.

The typical elements involved in solving an image registration problem within the Insight registration framework are: two input Images, a Transform, a Metric, an Interpolator and an Optimizer. Some of these components are parametrized by the image type for which the registration is intended. ITK provides header files for common types of these components.

Monitoring

Given the numerous parameters involved in tuning a registration method for a particular application it is common to be faced with a registration process that runs for several minutes and ends up with a useless result. In order to avoid this situation it is quite helpful to track the evolution of the registration as it progresses. ITK provides mechanisms for monitoring the activity of the registration method class.

Transform

ITK provides a variety of transforms from simple translation, rotation and scaling to general affine and kernel transforms.

Interpolator

During the registration process, a metric typically compares the intensity values in the fixed image with the corresponding values in the transformed moving image. When a point is mapped from one image space to another, it will generally be mapped to a non-grid position. Thus, an interpolation method is needed to obtain a intensity value for the mapped point using the information from the neighboring grid positions. Three of the most popular interpolation methods: nearest-neighbor, linear and B-spline are available in ITK.

Metric

In ITK, image metric objects measure quantitatively how well the transformed moving image fits the fixed image by comparing the gray-scale intensity of the images. The metrics available in ITK are: Mean Squares Metric, Normalized Correlation Metric, Mean Reciprocal Square Differences, Mutual Information Metric.

Optimizer

The role of the optimizer component is to optimize the qualitative measure provided by the metric with respect to the parameters of the transform component. A variety of optimizer objects are provided by ITK: Amoeba, Conjugate Gradient, Gradient Descent, Quaternion Rigid Transform Gradient Descent, LBFGS, Regular Step Gradient Descent, LevenbergMarquard among others.

Deformable Registration

The finite element (FEM) library within the Insight Toolkit can be used to solve deformable image registration problems.

For the problem of intra-modality deformable registration, the Insight Toolkit provides an implementation of Thirion's "demons" algorithm. In this implementation, each image is viewed as a set of iso-intensity contours. The main idea is that a regular grid of forces deform an image by pushing the contours in the normal direction.

However, the most widely used algorithm for this purpose in ITK is the one based in BSpline transform. The major difference is that this algorithm can manage a large number of degrees of freedom.

B.4. Process Pipeline

Next we show the computational pipeline designed for the segmentation and registration process of the aortic lumen.

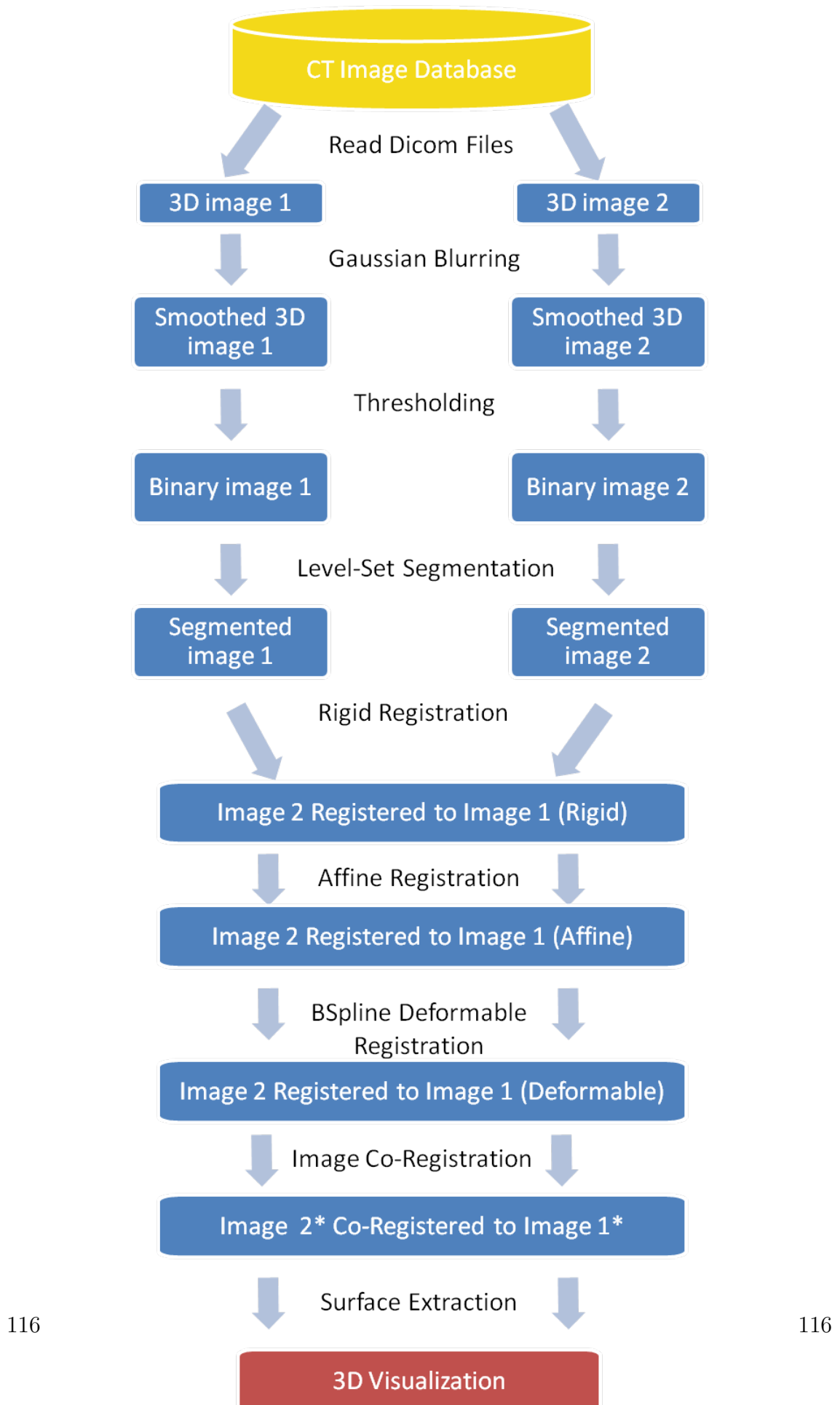


Figure B.1.: Pipeline of the processes involved in the segmentation and registration process. (Image 1: Lumen in the 1st study, Image 2: Lumen in the 2nd study, Image 2*: Image 2 after registration to Image 1, Image 1*: Image 1 after registration to Image 2)

Bibliography

- [1] Elsevier inc.: Introduction to ct physics, 2004.
- [2] K. Abdel-Malek, DP McGowan, VK Goel, D. Kowalski, and SB Smith. Bone registration method for robot assisted surgery: pedicle screw insertion. *Proceedings of the Institution of Mechanical Engineers, Part H: Journal of Engineering in Medicine*, 211(3):221–233, 1997.
- [3] R. Adams and L. Bischof. Seeded region growing. *IEEE Transactions on Pattern Analysis and Machine Intelligence*, 16(6):641–647, 1994.
- [4] S. S. Ahn, R. B. Rutherford, K. W. Johnston, J. May, F. J. Veith, J. D. Baker, C. B. Ernst, and W. S. Moore. Reporting standards for infrarenal endovascular abdominal aortic aneurysm repair. *Journal of Vascular Surgery*, 25(2):405–410, 1997.
- [5] A. Ali and A. Farag. Automatic lung segmentation of volumetric low-dose ct scans using graph cuts. *Advances in Visual Computing*, pages 258–267, 2008.
- [6] J Alirezaie, ME Jernigan, and C Nahmias. Neural network-based segmentation of magnetic resonance images of the brain. *IEEE Transactions On Nuclear Science*, 44(2):194–198, APR 1997.
- [7] E. Alpaydin. *Introduction to machine learning*. The MIT Press, 2004.
- [8] Y. Amit and D. Geman. Shape quantization and recognition with randomized trees. *Neural computation*, 9(7):1545–1588, 1997.
- [9] D. Angluin. Queries and concept learning. *Machine learning*, 2(4):319–342, 1988.
- [10] R. Bansal, L. Staib, Z. Chen, A. Rangarajan, J. Knisely, R. Nath, and J. Duncan. Entropy-based, dual-portal-to-3DCT registration incorporating pixel correlation. *IEEE Trans. Med. Imaging*, 22(1):29–49, 2003.
- [11] R. Bansal, L. H. Staib, and B. S. Peterson. Correcting nonuniformities in MRI intensities using entropy minimization based on an elastic model. In C. Barillot, D. R. Haynor, and P. Hellier, editors, *Medical Image Computing and Computer-Assisted Intervention (MICCAI)*, page 78. Part I, LNCS 3216, Springer, 2004.
- [12] Iñigo Barandiaran, Celine Paloc, and Manuel Graña. Real-time optical markerless tracking for augmented reality applications. *Journal of Real-Time Image Processing*, 5:129–138, 2010.

-
- [13] R. Battiti. First-and second-order methods for learning: between steepest descent and newton's method. *Neural computation*, 4(2):141–166, 1992.
- [14] Craig A. Beam, Elizabeth A. Krupinski, Harold L. Kundel, Edward A. Sickles, and Robert F. Wagner. The place of medical image perception in 21st-century health care. *Journal of the American College of Radiology*, 3(6):409 – 412, 2006. <ce:title>Special Issue: Image Perception</ce:title> <xocs:full-name>Special Issue: Image Perception</xocs:full-name>.
- [15] Hugh G Beebe and Boonprasit Kritpracha. Computed tomography scanning for endograft planning: evolving toward three-dimensional, single source imaging. *Semin Vasc Surg*, 17(2):126–134, Jun 2004.
- [16] S Beucher. Watershed, hierarchical segmentation and waterfall algorithm. In Serra, J and Soille, P, editor, *Mathematical Morphology And Its Applications To Image Processing*, volume 2 of *Computational Imaging And Vision*, pages 69–76, 1994.
- [17] C.M. Bishop. *Pattern recognition and machine learning*, volume 4. springer New York, 2006.
- [18] F. Bookstein. Thin-plate splines and the atlas problem for biomedical images. In *Information Processing in Medical Imaging*, pages 326–342. Springer, 1991.
- [19] Y. Boykov and M.P. Jolly. Interactive organ segmentation using graph cuts. In *Medical Image Computing and Computer-Assisted Intervention–MICCAI 2000*, pages 147–175. Springer, 2000.
- [20] L. Breiman. Bagging predictors. *Machine learning*, 24(2):123–140, 1996.
- [21] L. Breiman. Random forests. *Machine learning*, 45(1):5–32, 2001.
- [22] I. A. Broeders and J. D. Blankensteijn. A simple technique to improve the accuracy of proximal aaa endograft deployment. *J Endovasc Ther*, 7(5):389–393, Oct 2000.
- [23] D.S. Broomhead and D. Lowe. Multivariable functional interpolation and adaptive networks. *Complex Systems*, 2:321–355, 1998.
- [24] C. Burges. A tutorial on Support Vector Machines for pattern recognition. *Data Mining and Knowledge Discovery*, 2(2):121–167, 1998.
- [25] Christopher J. C. Burges. A tutorial on support vector machines for pattern recognition, 1998.
- [26] W. Cai, S. Chen, and D. Zhang. Fast and robust fuzzyc-means clustering algorithms incorporating local information for image segmentation. *Pattern Recognition*, 40:825–838, 2007.
- [27] C. Campbell, N. Cristianini, and A. Smola. Query learning with large margin classifiers. In *Machine Learning -International Workshop Then Conference-*, pages 111–118, 2000.

- [28] J Canny. A computational approach to edge-detection. *Ieee transactions on pattern analysis and machine intelligence*, 8(6):679–698, Nov 1986.
- [29] V Caselles, R Kimmel, and G Sapiro. Geodesic active contours. *International Journal Of Computer Vision*, 22(1):61–79, FEB-MAR 1997.
- [30] E. L. Chaikof, J. D. Blankensteijn, P. L. Harris, G. H. White, C. K. Zarins, V. M. Bernhard, J. S. Matsumura, J. May, F. J. Veith, M. F. Fillinger, R. B. Rutherford, and K. C. Kent. Reporting standards for endovascular aortic aneurysm repair. *Journal of Vascular Surgery*, 35(5):1048–1060, 2002.
- [31] A. Chakraborty, L. H. Staib, and J. S. Duncan. Deformable boundary finding influenced by region homogeneity. In *Proc. Comp. Vision Pattern Recog.*, pages 624–627, 1994.
- [32] A. Chakraborty, L. H. Staib, and J. S. Duncan. Deformable boundary finding in medical images by integrating gradient and region information. *IEEE Trans. Med. Imaging*, 15(6):859–870, 1996.
- [33] S. Chen, C.F.N. Cowan, and P.M. Grant. Orthogonal Least Squares Learning algorithm for Radial Basis Function Networks. *Neural Networks, IEEE Transactions on*, pages 302–309, 1991.
- [34] KS Cheng, JS Lin, and CW Mao. The application of competitive Hopfield neural network to medical image segmentation. *IEEE Transactions On Medical Imaging*, 15(4):560–567, AUG 1996.
- [35] D. Chillet, J. Jomier, D. Cool, and S. Aylward. Vascular atlas formation using a vessel-to-image affine registration method. *Medical Image Computing and Computer-Assisted Intervention-MICCAI 2003*, pages 335–342, 2003.
- [36] D.A. Cohn, Z. Ghahramani, and M.I. Jordan. Active learning with statistical models. *arXiv preprint cs/9603104*, 1996.
- [37] David Cohn, Les Atlas, and Richard Ladner. Improving generalization with active learning. *Machine Learning*, 15:201–221, 1994.
- [38] P. Comon. Independent component analysis, a new concept? *Signal processing*, 36(3):287–314, 1994.
- [39] TF Cootes, GJ Edwards, and CJ Taylor. Active appearance models. *IEEE Transactions On Pattern Analysis And Machine Intelligence*, 23(6):681–685, JUN 2001.
- [40] T.F. Cootes, C.J. Taylor, D.H. Cooper, J. Graham, et al. Active shape models—their training and application. *Computer vision and image understanding*, 61(1):38–59, 1995.
- [41] A. Criminisi, J. Shotton, and S. Bucciarelli. Decision forests with long-range spatial context for organ localization in ct volumes. In *MICCAI Workshop on Probabilistic Models for Medical Image Analysis*, 2009.

- [42] A. Criminisi, J. Shotton, D. Robertson, and E. Konukoglu. Regression forests for efficient anatomy detection and localization in ct studies. *Medical Computer Vision. Recognition Techniques and Applications in Medical Imaging*, pages 106–117, 2011.
- [43] I. Dagan and S.P. Engelson. Committee-based sampling for training probabilistic classifiers. In *Machine Learning -International Workshop Then Conference-*, pages 150–157. MORGAN KAUFMANN PUBLISHERS, INC., 1995.
- [44] J. B. Dattilo, D. C. Brewster, C. M. Fan, S. C. Geller, R. P. Cambria, G. M. LaMuraglia, A. J. Greenfield, S. R. Lauterbach, and W. M. Abbott. Clinical failures of endovascular abdominal aortic aneurysm repair: Incidence, causes, and management. *Journal of Vascular Surgery*, 35(6):1137–1144, 2002.
- [45] Marleen de Bruijne, Bram van Ginneken, Max A Viergever, and Wiro J Niessen. Interactive segmentation of abdominal aortic aneurysms in cta images. *Med Image Anal*, 8(2):127–138, Jun 2004.
- [46] S. Demirci, F. Manstad-Hulaas, and N. Navab. Quantification of abdominal aortic deformation after evar. In *Proceedings of SPIE*, volume 7261, page 72611U, 2009.
- [47] E.R.E. Denton, L.I. Sonoda, D. Rueckert, S.C. Rankin, C. Hayes, M.O. Leach, D.L.G. Hill, and D.J. Hawkes. Comparison and evaluation of rigid, affine, and nonrigid registration of breast mr images. *Journal of computer assisted tomography*, 23(5):800–805, 1999.
- [48] Maxime Descoteaux, D. Louis Collins, and Kaleem Siddiqi. A geometric flow for segmenting vasculature in proton-density weighted mri. *Medical Image Analysis*, 12(4):497 – 513, 2008.
- [49] K. Doi. Computer-aided diagnosis in medical imaging: historical review, current status and future potential. *Computerized medical imaging and graphics: the official journal of the Computerized Medical Imaging Society*, 31(4-5):198, 2007.
- [50] P. Domingos and M. Pazzani. On the optimality of the simple bayesian classifier under zero-one loss. *Machine learning*, 29(2):103–130, 1997.
- [51] RO Duda, PE Hart, and DG Stork. Pattern classification, nonparametric techniques, 2000.
- [52] J. Duncan, X. Papademetris, J. Yang, M. Jackowski, X. Zeng, and L. H. Staib. Geometric strategies for neuroanatomical analysis from MRI. 23:S34–S45, 2004. <http://dx.doi.org/10.1016/j.neuroimage.2004.07.027>.
- [53] J.S. Duncan and L.H. Staib. Image processing and analysis at ipag. *IEEE Trans. Med. Imaging*, 22(12):1505–1518, 2003.
- [54] J. Feldmar and N. Ayache. Rigid, affine and locally affine registration of free-form surfaces. *International journal of computer vision*, 18(2):99–119, 1996.

- [55] Matthieu Ferrant, Arya Nabavi, Benoît Macq, P. M. Black, Ferenc A Jolesz, Ron Kikinis, and Simon K Warfield. Serial registration of intraoperative mr images of the brain. *Med Image Anal*, 6(4):337–359, Dec 2002.
- [56] M. F. Fillinger. Imaging of the thoracic and thoracoabdominal aorta. *Semin Vasc Surg*, 13(4):247–263, Dec 2000.
- [57] Moti Freiman, Steven J. Esses, Leo Joskowicz, and Jacob Sosna. An Iterative Model-Constraint Graph-cut Algorithm for Abdominal Aortic Aneurysm Thrombus Segmentation. In *Proc. of the 2010 IEEE Int. Symp. on Biomedical Imaging: From Nano to Macro (ISBI'10)*, pages 672–675, Rotterdam, The Netherlands, April 2010. IEEE.
- [58] T. Fukushima, T. Matsuzawa, and T. Homma. Visualization and finite-element analysis of pulsatile flow in models of the abdominal aortic-aneurysm. *Biorheology*, 26(2):109–130, 1989.
- [59] Y. Gao, R. Sandhu, G. Fichtinger, and A.R. Tannenbaum. A coupled global registration and segmentation framework with application to magnetic resonance prostate imagery. *Medical Imaging, IEEE Transactions on*, 29(10):1781–1794, 2010.
- [60] D. Garcia-Lorenzo, J. Lecoœur, D. Arnold, D. Collins, and C. Barillot. Multiple sclerosis lesion segmentation using an automatic multimodal graph cuts. *Medical Image Computing and Computer-Assisted Intervention–MICCAI 2009*, pages 584–591, 2009.
- [61] C. Georg, V. Welker, H. Eidam, and H. Alfkel. Aortic stentgraft movement detection using digital roentgen stereophotogrammetric analysis on plane film radiographs - initial results of a phantom study. *Rofo-Fortschritte Auf dem Gebiet der Rontgenstrahlen und der Bildgebenden Verfahren*, 177(3):321–325, 2005.
- [62] E. Geremia, B. Menze, O. Clatz, E. Konukoglu, A. Criminisi, and N. Ayache. Spatial decision forests for ms lesion segmentation in multi-channel mr images. *Medical Image Computing and Computer-Assisted Intervention–MICCAI 2010*, pages 111–118, 2010.
- [63] D.E. Goldberg and J.H. Holland. Genetic algorithms and machine learning. *Machine Learning*, 3(2):95–99, 1988.
- [64] E. Haber and J. Modersitzki. Intensity gradient based registration and fusion of multi-modal images. *Medical Image Computing and Computer-Assisted Intervention–MICCAI 2006*, pages 726–733, 2006.
- [65] M.T. Hagan, H.B. Demuth, M.H. Beale, et al. *Neural network design*. PWS Boston, MA, 1996.
- [66] J. V. Hajnal, D. J. Hawkes, and D. L. G. Hill. *Medical image registration*. CRC, 2001.

- [67] Mark Hall, Eibe Frank, Geoffrey Holmes, Bernhard Pfahringer, Peter Reutemann, and Ian H. Witten. The WEKA data mining software. *ACM SIGKDD Explorations Newsletter*, 11:10, November 2009.
- [68] Heinz Handels, René Werner, Rainer Schmidt, Thorsten Frenzel, Wei Lu, Daniel Low, and Jan Ehrhardt. 4d medical image computing and visualization of lung tumor mobility in spatio-temporal ct image data. *International Journal of Medical Informatics*, 76, Supplement 3(0):S433 – S439, 2007. <ce:title>Ubiquity: Technologies for Better Health in Aging Societies - MIE 2006</ce:title>.
- [69] P Harris, J Brennan, J Martin, D Gould, A Bakran, G Gilling-Smith, J Buth, E Gevers, and D White. Longitudinal aneurysm shrinkage following endovascular aortic aneurysm repair: A source of intermediate and late complications. *Journal Of Endovascular Surgery*, 6(1):11–16, FEB 1999.
- [70] P. L. Harris, S. R. Vallabhaneni, P. Desgranges, J. P. Bacquemin, C. van Marrewijk, and R. J. F. Laheij. *Incidence and risk factors of late rupture, conversion, and death after endovascular repair of infrarenal aortic aneurysms: The Eurostar experience*, volume 32. 2000.
- [71] T. Hastie, R. Tibshirani, and J. Friedman. High-dimensional problems: p n. *The elements of statistical learning*, pages 1–50, 2009.
- [72] S. Haykin. *Neural Networks: a comprehensive foundation (2nd edition)*. Prentice Hall, 2 edition, 1998.
- [73] S. Haykin. *Neural networks: a comprehensive foundation*. Prentice hall, 1999.
- [74] K. Held, E.R. Kops, B.J. Krause, W.M. Wells III, R. Kikinis, and H.W. Muller-Gartner. Markov random field segmentation of brain mr images. *Medical Imaging, IEEE Transactions on*, 16(6):878–886, 1997.
- [75] Pierre Hellier and Christian Barillot. Coupling dense and landmark-based approaches for nonrigid registration. *IEEE Trans Med Imaging*, 22(2):217–227, Feb 2003.
- [76] D. L. Hill, P. G. Batchelor, M. Holden, and D. J. Hawkes. Medical image registration. *Phys Med Biol*, 46(3):R1–45, Mar 2001.
- [77] T.K. Ho. The random subspace method for constructing decision forests. *Pattern Analysis and Machine Intelligence, IEEE Transactions on*, 20(8):832–844, 1998.
- [78] J. Huang, D. Abendschein, V.G. Davila-Roman, and A.A. Amini. Spatio-temporal tracking of myocardial deformations with a 4-d b-spline model from tagged mri. *Medical Imaging, IEEE Transactions on*, 18(10):957–972, 1999.
- [79] L. Ibanez, L. Ng, J. Gee, and S. Aylward. *Registration patterns: The generic framework for image registration of the insight toolkit*. 2002 IEEE International Symposium on Biomedical Imaging, Proceedings. 2002.

- [80] J.Cronenwett, W.Krupski, and R.Rutherford. Abdominal aortic and iliac aneurysm, 2000.
- [81] Chris R. Johnson and Xavier Tricoche. Chapter 6 - biomedical visualization. In Pascal Verdonck, editor, *Advances in Biomedical Engineering*, pages 211 – 273. Elsevier, Amsterdam, 2009.
- [82] I.T. Jolliffe and MyiLibrary. *Principal component analysis*, volume 2. Wiley Online Library, 2002.
- [83] M Kass, A Witkin, and D Terzopoulos. Snakes - Active Contour Models. *International Journal Of Computer Vision*, 1(4):321–331, 1987.
- [84] G. Kedenburg, C. Cocosco, U. Köthe, W. Niessen, E. Vonken, and M. Viergever. Automatic cardiac mri myocardium segmentation using graph-cut. In *Proceedings of SPIE*, volume 6144, page 61440A. Citeseer, 2006.
- [85] Gabriel Kiss, Stylianos Drisis, Didier Bielen, Frederik Maes, Johan Van Cleyenbreugel, Guy Marchal, and Paul Suetens. Computer-aided detection of colonic polyps using low-dose ct acquisitions. *Academic Radiology*, 13(9):1062 – 1071, 2006.
- [86] G.J. Klein, RW Reutter, and R.H. Huesman. Four-dimensional affine registration models for respiratory-gated pet. *Nuclear Science, IEEE Transactions on*, 48(3):756–760, 2001.
- [87] R. Knowlton. Clinical applications of image registration. *Handbook of Medical Imaging*, pages 613–621, 2000.
- [88] T. Kohonen. *Self-Organization and Associative Memory*. Information Sciences. Springer, 1989.
- [89] I. Kononenko. Machine learning for medical diagnosis: history, state of the art and perspective. *Artificial Intelligence in medicine*, 23(1):89–109, 2001.
- [90] J Kybic and M Unser. Multidimensional elastic registration of images using splines. In *2000 International Conference on Image Processing, Vol II, Proceedings*, pages 455–458. IEEE, Signal Processing Soc, IEEE, 2000.
- [91] L. Ladicky, P. Sturges, C. Russell, S. Sengupta, Y. Bastanlar, W. Clocksin, and P.H.S. Torr. Joint optimization for object class segmentation and dense stereo reconstruction. *International Journal of Computer Vision*, pages 1–12, 2011.
- [92] N. Landwehr, M. Hall, and E. Frank. Logistic model trees. *Machine Learning*, 59(1):161–205, 2005.
- [93] V. Lempitsky, M. Verhoek, J. Noble, and A. Blake. Random forest classification for automatic delineation of myocardium in real-time 3d echocardiography. *Functional Imaging and Modeling of the Heart*, pages 447–456, 2009.

-
- [94] David Lesage, Elsa D. Angelini, Isabelle Bloch, and Gareth Funka-Lea. A review of 3d vessel lumen segmentation techniques: Models, features and extraction schemes. *Medical Image Analysis*, 13(6):819 – 845, 2009.
- [95] D.D. Lewis and W.A. Gale. A sequential algorithm for training text classifiers. In *Proceedings of the 17th annual international ACM SIGIR conference on Research and development in information retrieval*, pages 3–12. Springer-Verlag New York, Inc., 1994.
- [96] Z. Li and C. Kleinstreuer. Analysis of biomechanical factors affecting stent-graft migration in an abdominal aortic aneurysm model. *Journal of Biomechanics*, 39(12):2264–2273, 2006.
- [97] Z. Li, C. Kleinstreuer, and M. Farber. Computational analysis of biomechanical contributors to endovascular graft failure. *Biomechanics and Modeling in Mechanobiology*, 4(4):221–234, 2005.
- [98] C.P. Lim, R.F. Harrison, and R.L. Kennedy. Application of autonomous neural network systems to medical pattern classification tasks. *Artificial intelligence in medicine*, 11(3):215, 1997.
- [99] Y. Liu. Active learning with support vector machine applied to gene expression data for cancer classification. *Journal of chemical information and computer sciences*, 44(6):1936–1941, 2004.
- [100] H. Livyatan, Z. Yaniv, and L. Joskowicz. Gradient-based 2-d/3-d rigid registration of fluoroscopic x-ray to ct. *Medical Imaging, IEEE Transactions on*, 22(11):1395–1406, 2003.
- [101] H.T. Luebbbers, P. Messmer, J.A. Obwegeser, R.A. Zwahlen, R. Kikinis, K.W. Graetz, and F. Matthews. Comparison of different registration methods for surgical navigation in cranio-maxillofacial surgery. *Journal of Cranio-Maxillofacial Surgery*, 36(2):109–116, 2008.
- [102] A. M. Lutz, J. K. Willmann, T. Pfammatter, M. Lachat, S. Wildermuth, B. Marincek, and D. Weishaupt. Evaluation of aortoiliac aneurysm before endovascular repair: Comparison of contrast-enhanced magnetic resonance angiography with multidetector row computed tomographic angiography with an automated analysis software tool. *Journal of Vascular Surgery*, 37(3):619–627, 2003.
- [103] B. Ma and R. Ellis. Surface-based registration with a particle filter. *Medical Image Computing and Computer-Assisted Intervention–MICCAI 2004*, pages 566–573, 2004.
- [104] I. Macia, M. Grana, J. Maiora, C. Paloc, and M. de Blas. Detection of type ii endoleaks in abdominal aortic aneurysms after endovascular repair. *Computers in Biology and Medicine*, 41(10):871–880, 2011.
- [105] I Macia, M. Graña, and C. Paloc. Knowledge management in image-based

- analysis of blood vessel structures. *Knowledge and Information Systems*, 30(2):457–491, 2012.
- [106] Ivan Macia, Jon Hartz Legarreta, Celine Paloc, Manuel Grana, Josu Maiora, Guillermo Garcia, and Mariano de Blas. Segmentation of Abdominal Aortic Aneurysms in CT Images Using a Radial Model Approach. In Corchado, E and Yin, H, editor, *Intelligent Data Engineering and Automated Learning, Proceedings*, volume 5788 of *Lecture Notes in Computer Science*, pages 664–671. Springer-Verlag Berlin, 2009.
- [107] D.J.C. MacKay. Information-based objective functions for active data selection. *Neural computation*, 4(4):590–604, 1992.
- [108] Josu Maiora, Guillermo Garcia, Arantxa Tapia, Ivan Macia, Jon Hartz Legarreta, Celine Paloc, Mariano De Blas, and Manuel Grana. Thrombus change detection after endovascular abdominal aortic aneurysm repair. In *International Journal of Computer Assisted Radiology and Surgery*, volume 5 (Suppl 1), page S15, Berlin, Heidelberg, 2010. Springer-Verlag.
- [109] R Malladi, Ja Sethian, and Bc Vemuri. Shape Modeling with Front Propagation - A Level Set Approach. *IEEE Transactions On Pattern Analysis And Machine Intelligence*, 17(2):158–175, FEB 1995.
- [110] P. Markelj, D. Tomazevic, F. Pernus, and B. Likar. Robust gradient-based 3-d/2-d registration of ct and mr to x-ray images. *Medical Imaging, IEEE Transactions on*, 27(12):1704–1714, 2008.
- [111] G.K. Matsopoulos, N.A. Mouravliansky, K.K. Delibasis, and K.S. Nikita. Automatic retinal image registration scheme using global optimization techniques. *Information Technology in Biomedicine, IEEE Transactions on*, 3(1):47–60, 1999.
- [112] J Mattes, I Steingruber, M Netzer, K Fritscher, H Kopf, W Jaschke, and R Schubert. Spatio-temporal changes and migration of stent grafts after endovascular aortic aneurysm repair. In Lemke, HU and Inamura, K and Doi, K and Vannier, MW and Farman, AG, editor, *CARS 2005: Computer Assisted Radiology and Surgery*, volume 1281 of *International Congress Series*, pages 393–397, 2005.
- [113] Julian Mattes, Iris Steingruber, Michael Netzer, Karl Fritscher, Helmut Kopf, Werner Jaschke, and Rainer Schubert. Quantification of the migration and deformation of abdominal aortic aneurysm stent grafts. volume 6144, page 61440V. SPIE, 2006.
- [114] T. McInerney and D. Terzopoulos. Deformable models in medical image analysis. In *Mathematical Methods in Biomedical Image Analysis, 1996., Proceedings of the Workshop on*, pages 171–180. IEEE, 1996.
- [115] DS Meier and CRG Guttman. Time-series analysis of mri intensity patterns in multiple sclerosis. *Neuroimage*, 20(2):1193–1209, OCT 2003.

- [116] M. Moghari and P. Abolmaesumi. A novel incremental technique for ultrasound to ct bone surface registration using unscented kalman filtering. *Medical Image Computing and Computer-Assisted Intervention–MICCAI 2005*, pages 197–204, 2005.
- [117] A. Mohamed, E.I. Zacharaki, D. Shen, C. Davatzikos, et al. Deformable registration of brain tumor images via a statistical model of tumor-induced deformation. *Medical image analysis*, 10(5):752–763, 2006.
- [118] NA Mohamed, MN Ahmed, and A Farag. Modified fuzzy c-mean in medical image segmentation. In Chang, HK and Zhang, YT, editor, *Proceedings of The 20th Annual International Conference of The IEEE Engineering In Medicine And Biology Society, Vol 20, Pts 1-6 - Biomedical Engineering Towards The Year 2000 And Beyond*, volume 20, pages 1377–1380, 1998.
- [119] K. Murphy, B. van Ginneken, S. Klein, M. Staring, B.J. de Hoop, M.A. Viergever, and J.P.W. Pluim. Semi-automatic construction of reference standards for evaluation of image registration. *Medical Image Analysis*, 15(1):71 – 84, 2011.
- [120] H. P. Ng, S. Huang, S. H. Ong, K. C. Foong, P. S. Goh, and W. L. Nowinski. Medical image segmentation using watershed segmentation with texture-based region merging. *Conf Proc IEEE Eng Med Biol Soc*, 2008:4039–4042, 2008.
- [121] Toshiyuki Okada, Ryuji Shimada, Masatoshi Hori, Masahiko Nakamoto, Yen-Wei Chen, Hironobu Nakamura, and Yoshinobu Sato. Automated segmentation of the liver from 3d ct images using probabilistic atlas and multilevel statistical shape model. *Academic Radiology*, 15(11):1390 – 1403, 2008.
- [122] SD Olabarriaga, JM Rouet, M Fradkin, M Breeuwer, and WJ Niessen. Segmentation of thrombus in abdominal aortic aneurysms from CTA with non-parametric statistical grey level appearance modeling. *IEEE Transactions On Medical Imaging*, 24(4):477–485, APR 2005.
- [123] J. Orban de Xivry, G. Janssens, G. Bosmans, M. De Craene, A. Dekker, J. Buijsen, A. van Baardwijk, D. De Ruysscher, B. Macq, and P. Lambin. Tumour delineation and cumulative dose computation in radiotherapy based on deformable registration of respiratory correlated ct images of lung cancer patients. *Radiotherapy and Oncology*, 85(2):232–238, 2007.
- [124] S Osher and Ja Sethian. Fronts Propagating With Curvature-dependent Speed - Algorithms Based On Hamilton-Jacobi Formulations. *Journal Of Computational Physics*, 79(1):12–49, NOV 1988.
- [125] R. L. Owen, L. H. Staib, P. Anandan, and J. S. Duncan. Measurement of left ventricular wall motion from contour shape deformation. In J. Llacer and D. Ortendahl, editors, *Information Proc. Med. Imaging*. Wiley-Liss, New York, 1989.
- [126] X. Papademetris, A. P. Jackowski, R. T. Schultz, L. H Staib, and J. S. Duncan. Computing 3D non-rigid brain registration using extended robust point

- matching for composite multisubject fMRI analysis. In *Medical Image Computing and Computer-Assisted Intervention (MICCAI)*, volume Lecture Notes in Computer Science, 2003.
- [127] J. C. Parodi, J. C. Palmaz, and H. D. Barone. Transfemoral intraluminal graft implantation for abdominal aortic aneurysms. *Ann Vasc Surg*, 5(6):491–499, Nov 1991.
- [128] Ca Pelizzari, Gty Chen, Dr Spelbring, Rr Weichselbaum, and Ct Chen. Accurate 3-dimensional Registration Of CT, PET, And Or MR Images Of The Brain. *Journal Of Computer Assisted Tomography*, 13(1):20–26, JAN-FEB 1989.
- [129] F. Pereira, T. Mitchell, and M. Botvinick. Machine learning classifiers and fmri: a tutorial overview. *Neuroimage*, 45(1 Suppl):S199, 2009.
- [130] J.P.W. Pluim, J.B.A. Maintz, and M.A. Viergever. Mutual-information-based registration of medical images: a survey. *Medical Imaging, IEEE Transactions on*, 22(8):986–1004, 2003.
- [131] A Pommert and K.H Höhne. Validation of medical volume visualization: a literature review. *International Congress Series*, 1256(0):571 – 576, 2003. <ce:title>CARS 2003. Computer Assisted Radiology and Surgery. Proceedings of the 17th International Congress and Exhibition</ce:title>.
- [132] W.H. Press, S.A. Teukolsky, W.T. Vetterling, and B.P. Flannery. Numerical recipes in c: the art of scientific computing. 2. *Cambridge: CUP*, 1992.
- [133] N. Ritter, R. Owens, J. Cooper, R.H. Eikelboom, and P.P. Van Saarloos. Registration of stereo and temporal images of the retina. *Medical Imaging, IEEE Transactions on*, 18(5):404–418, 1999.
- [134] A. Roche, X. Pennec, G. Malandain, and N. Ayache. Rigid registration of 3-d ultrasound with mr images: a new approach combining intensity and gradient information. *Medical Imaging, IEEE Transactions on*, 20(10):1038–1049, 2001.
- [135] K. Rohr. *Landmark-based image analysis: using geometric and intensity models*. Springer Netherlands, 2001.
- [136] J.M. Rouet, J.J. Jacq, and C. Roux. Genetic algorithms for a robust 3-d mr-ct registration. *Information Technology in Biomedicine, IEEE Transactions on*, 4(2):126–136, 2000.
- [137] N. Roy and A. McCallum. Toward optimal active learning through monte carlo estimation of error reduction. *ICML, Williamstown*, 2001.
- [138] D.W. Ruck, S.K. Rogers, M. Kabrisky, P.S. Maybeck, and M.E. Oxley. Comparative Analysis of Backpropagation and the Extended Kalman Filter for training Multilayer Perceptrons. *IEEE Trans. Pattern Anal. Mach. Intell.*, 14(6):686–691, 1992.

- [139] D. Rueckert, P. Aljabar, R. Heckemann, J. Hajnal, and A. Hammers. Diffeomorphic registration using b-splines. *Medical Image Computing and Computer-Assisted Intervention–MICCAI 2006*, pages 702–709, 2006.
- [140] DE Rumelhart and GE Hinton. Williams. rj (1986) learning representations by backpropagating errors. *Nature*, pages 533–536, 1986.
- [141] D.E. Rumelhart, G.E. Hinton, and R.J. Williams. Learning internal representations by error propagation. *Parallel distributed processing: explorations in the microstructure of cognition*, 1: foundations:318–362, 1986.
- [142] D.E. Rumelhart, J.L. McClelland, and the PDP Research Group. *Parallel distributed processing*, volume 1: Foundations. Cambridge, MA: MIT Press, 1986.
- [143] R. B. Rutherford and W. C. Krupski. Current status of open versus endovascular stent-graft repair of abdominal aortic aneurysm. *Journal of Vascular Surgery*, 39(5):1129–1139, 2004.
- [144] J. Rydberg, K. K. Kopecky, S. G. Lalka, M. S. Johnson, M. C. Dalsing, and S. A. Persohn. Stent grafting of abdominal aortic aneurysms: pre-and postoperative evaluation with multislice helical ct. *J Comput Assist Tomogr*, 25(4):580–586, 2001.
- [145] D. Salas Gonzalez, JM Gorriz, J. Ramirez, A. Lassl, and CG Puntonet. Improved gauss-newton optimisation methods in affine registration of spect brain images. *Electronics Letters*, 44(22):1291–1292, 2008.
- [146] A.P. Santhanam, Y. Min, S.P. Mudur, A. Rastogi, B.H. Ruddy, A. Shah, E. Divo, A. Kassab, J.P. Rolland, and P. Kupelian. An inverse hyper-spherical harmonics-based formulation for reconstructing 3d volumetric lung deformations. *Comptes Rendus Mecanique*, 338(7-8):461–473, 2010.
- [147] U.J. Schoepf and P. Costello. Ct angiography for diagnosis of pulmonary embolism: State of the art1. *Radiology*, 230(2):329–337, 2004.
- [148] B. Settles. Active learning literature survey. *SciencesNew York*, 15(2), 2010.
- [149] H.S. Seung, M. Opper, and H. Sompolinsky. Query by committee. In *Proceedings of the fifth annual workshop on Computational learning theory*, pages 287–294. ACM, 1992.
- [150] Reuben R. Shamir and Leo Joskowicz. Geometrical analysis of registration errors in point-based rigid-body registration using invariants. *Medical Image Analysis*, 15(1):85 – 95, 2011.
- [151] C.E. Shannon, W. Weaver, R.E. Blahut, and B. Hajek. *The mathematical theory of communication*, volume 117. University of Illinois press Urbana, 1949.
- [152] D. G. Shen. Image registration by local histogram matching. *Pattern Recognition*, 40(4):1161–1172, 2007. Shen, Dinggang 35 PERGAMON-ELSEVIER SCIENCE LTD.

- [153] J. Shi and J. Malik. Normalized cuts and image segmentation. *Pattern Analysis and Machine Intelligence, IEEE Transactions on*, 22(8):888–905, 2000.
- [154] D. B. Smith, M. S. Sacks, D. A. Vorp, and M. Thornton. Surface geometric analysis of anatomic structures using biquintic finite element interpolation. *Annals of Biomedical Engineering*, 28(6):598–611, 2000.
- [155] Pierre Soille. *Morphological Image Analysis: Principles and Applications*. Springer-Verlag New York, Inc., Secaucus, NJ, USA, 2 edition, 2003.
- [156] P. Somervuo and T. Kohonen. Self-Organizing Maps and Learning Vector Quantization for feature sequences. *Neural Process. Lett.*, 10(2):151–159, 1999.
- [157] COS Sorzano, P Thevenaz, and M Unser. Elastic registration of biological images using vector-spline regularization. *IEEE Transactions On Biomedical Engineering*, 52(4):652–663, APR 2005.
- [158] L. R. Sprouse, G. H. Meier, F. N. Parent, R. J. Demasi, G. K. Stokes, C. J. Lesar, M. J. Marcinczyk, and B. Mendoza. Is three-dimensional computed tomography reconstruction justified before endovascular aortic aneurysm repair? *Journal of Vascular Surgery*, 40(3):443–447, 2004.
- [159] L. H. Staib and X. Lei. Intermodality 3D medical image registration with global search. In *Proc. IEEE Workshop Biomedical Image Anal.*, pages 225–234, 1994.
- [160] L. H. Staib, X. Zeng, A. Chakraborty, R. T. Schultz, and J. S. Duncan. Shape constraints in deformable models. In I. Bankman, editor, *Handbook of Medical Imaging: Processing and Analysis*. Academic Press, San Diego, 2000.
- [161] M. Subasic, S. Loncaric, and E. Sorantin. 3-d image analysis of abdominal aortic aneurysm. *Stud Health Technol Inform*, 77:1195–1200, 2000.
- [162] M. Subasic, S. Loncaric, and E. Sorantin. Region-based deformable model for aortic wall segmentation. In *Proc. 3rd Int. Symp. Image and Signal Processing and Analysis ISPA 2003*, volume 2, pages 731–735, 2003.
- [163] B. Suman and P. Kumar. A survey of simulated annealing as a tool for single and multiobjective optimization. *Journal of the operational research society*, 57(10):1143–1160, 2005.
- [164] S.J. Swensen, J.R. Jett, T.E. Hartman, D.E. Midthun, J.A. Sloan, A.M. Sykes, G.L. Aughenbaugh, and M.A. Clemens. Lung cancer screening with ct: Mayo clinic experience1. *Radiology*, 226(3):756–761, 2003.
- [165] D. Tao, X. Tang, X. Li, and X. Wu. Asymmetric bagging and random subspace for Support Vector Machines-based relevance feedback in image retrieval. *IEEE Trans. Pattern Anal. Mach. Intell.*, 28(7):1088–1099, 2006.
- [166] C.A. Thompson, M.E. Califf, and R.J. Mooney. Active learning for natural language parsing and information extraction. In *Machine Learning -International Workshop Then Conference-*, pages 406–414. Citeseer, 1999.

- [167] P. M. Thompson, J. N. Gledd, R. P. Woods, D. MacDonald, A. C. Evans, and A. W. Toga. Growth patterns in the developing brain detected by using continuum mechanical tensor maps. *Nature*, 404(6774):190–193, 2000.
- [168] S. Tong and E. Chang. Support vector machine active learning for image retrieval. In *Proceedings of the ninth ACM international conference on Multimedia*, pages 107–118. ACM, 2001.
- [169] D. Tuia, E. Pasolli, and W.J. Emery. Using active learning to adapt remote sensing image classifiers. *Remote Sensing of Environment*, 2011.
- [170] V. Vapnik. *Statistical learning theory*. Wiley-Interscience, 1998.
- [171] T. Vercauteren, X. Pennec, A. Perchant, and N. Ayache. Non-parametric diffeomorphic image registration with the demons algorithm. *Medical Image Computing and Computer-Assisted Intervention–MICCAI 2007*, pages 319–326, 2007.
- [172] T. Vercauteren, X. Pennec, A. Perchant, N. Ayache, et al. Diffeomorphic demons: Efficient non-parametric image registration. *NeuroImage*, 45(1), 2008.
- [173] P Viola and WM Wells. Alignment by maximization of mutual information. *International Journal Of Computer Vision*, 24(2):137–154, SEP 1997.
- [174] S. R. Walker, J. Macierewicz, N. M. Elmarasy, R. H. S. Gregson, S. C. Whitaker, and B. R. Hopkinson. A prospective study to assess changes in proximal aortic neck dimensions after endovascular repair of abdominal aortic aneurysms. *Journal of Vascular Surgery*, 29(4):625–630, 1999.
- [175] H. Wang, L. Dong, M.F. Lii, A.L. Lee, R. de Crevoisier, R. Mohan, J.D. Cox, D.A. Kuban, R. Cheung, et al. Implementation and validation of a three-dimensional deformable registration algorithm for targeted prostate cancer radiotherapy. *International journal of radiation oncology, biology, physics*, 61(3):725, 2005.
- [176] S. Wang, J. Yao, N. Petrick, and R.M. Summers. Combining statistical and geometric features for colonic polyp detection in ctc based on multiple kernel learning. *International journal of computational intelligence and applications*, 9(1):1, 2010.
- [177] S Wang, WY Zhu, and ZP Liang. Shape deformation: SVM regression and application to medical image segmentation. In *Eighth IEEE International Conference On Computer Vision, Vol II, Proceedings*, pages 209–216. IEEE Computer Soc, 2001.
- [178] J et al. West. Comparison and evaluation of retrospective intermodality brain image registration techniques. *Journal Of Computer Assisted Tomography*, 21(4):554–566, JUL-AUG 1997.
- [179] J. J. Wever, J. D. Blankensteijn, and B. C. Eikelboom. Secondary endoleak or missed endoleak? *Eur J Vasc Endovasc Surg*, 18(5):458–460, Nov 1999.

- [180] J. J. Wever, J. D. Blankensteijn, W. P. Th M Mali, and B. C. Eikelboom. Maximal aneurysm diameter follow-up is inadequate after endovascular abdominal aortic aneurysm repair. *Eur J Vasc Endovasc Surg*, 20(2):177–182, Aug 2000.
- [181] J. J. Wever, J. D. Blankensteijn, J. C. van Rijn, I. A. M. J. Broeders, B. C. Eikelboom, and W. P. T. M. Mali. Inter- and intraobserver variability of ct measurements obtained after endovascular repair of abdominal aortic aneurysms. *American Journal of Roentgenology*, 175(5):1279–1282, 2000.
- [182] G. H. White, J. May, R. C. Waugh, X. Chaufour, and W. Yu. Type iii and type iv endoleak: toward a complete definition of blood flow in the sac after endoluminal aaa repair. *J Endovasc Surg*, 5(4):305–309, Nov 1998.
- [183] G. H. White, W. Yu, J. May, X. Chaufour, and M. S. Stephen. Endoleak as a complication of endoluminal grafting of abdominal aortic aneurysms: classification, incidence, diagnosis, and management. *J Endovasc Surg*, 4(2):152–168, May 1997.
- [184] R. A. White, I. Walot, C. E. Donayre, J. Woody, and G. E. Kopchok. Failed aaa endograft exclusion due to type ii endoleak: explant analysis. *J Endovasc Ther*, 8(3):254–261, Jun 2001.
- [185] S. Winter, B. Brendel, I. Pechlivanis, K. Schmieder, and C. Igel. Registration of ct and intraoperative 3-d ultrasound images of the spine using evolutionary and gradient-based methods. *Evolutionary Computation, IEEE Transactions on*, 12(3):284–296, 2008.
- [186] R. P. Woods, S. T. Grafton, J. D. Watson, N. L. Sicotte, and J. C. Mazzotta. Automated image registration: Ii. intersubject validation of linear and nonlinear models. *J Comput Assist Tomogr*, 22(1):153–165, 1998.
- [187] D. Yang, S.R. Chaudhari, S.M. Goddu, D. Pratt, D. Khullar, J.O. Deasy, and I. El Naqa. Deformable registration of abdominal kilovoltage treatment planning ct and tomotherapy daily megavoltage ct for treatment adaptation. *Medical physics*, 36:329, 2009.
- [188] J. Yang, X. Papademetris, R. T. Schultz, L. H. Staib, and J. S. Duncan. Functional brain image analysis using joint function-structure priors. In C. Barillot, D. R. Haynor, and P. Hellier, editors, *Medical Image Computing and Computer-Assisted Intervention (MICCAI)*. Part I, LNCS 3216, Springer, 2004.
- [189] I. Yanovsky, A. D. Leow, S. Lee, S. J. Osher, and P. M. Thompson. Comparing registration methods for mapping brain change using tensor-based morphometry. *Medical Image Analysis*, 13(5):679–700, 2009.
- [190] M. Yaqub, M. Javaid, C. Cooper, and J. Noble. Improving the classification accuracy of the classic rf method by intelligent feature selection and weighted voting of trees with application to medical image segmentation. *Machine Learning in Medical Imaging*, pages 184–192, 2011.

- [191] Z. Yi, A. Criminisi, J. Shotton, and A. Blake. Discriminative, semantic segmentation of brain tissue in mr images. *Medical Image Computing and Computer-Assisted Intervention–MICCAI 2009*, pages 558–565, 2009.
- [192] H. Yu. Svm selective sampling for ranking with application to data retrieval. In *Proceedings of the eleventh ACM SIGKDD international conference on Knowledge discovery in data mining*, pages 354–363. ACM, 2005.
- [193] Kun-Chang Yu, Erik L. Ritman, and William E. Higgins. System for the analysis and visualization of large 3d anatomical trees. *Computers in Biology and Medicine*, 37(12):1802 – 1820, 2007.
- [194] Paul A. Yushkevich, Joseph Piven, Heather Cody Hazlett, Rachel Gimpel Smith, Sean Ho, James C. Gee, and Guido Gerig. User-guided 3D active contour segmentation of anatomical structures: Significantly improved efficiency and reliability. *Neuroimage*, 31(3):1116–1128, 2006.
- [195] C. K. Zarins, D. A. Bloch, T. Crabtree, A. H. Matsumoto, R. A. White, and T. J. Fogarty. Stent graft migration after endovascular aneurysm repair: Importance of proximal fixation. *Journal of Vascular Surgery*, 38(6):1264–1272, 2003.
- [196] Christopher K Zarins, Tami Crabtree, Daniel A Bloch, Frank R Arko, Kenneth Ouriel, and Rodney A White. Endovascular aneurysm repair at 5 years: Does aneurysm diameter predict outcome? *J Vasc Surg*, 44(5):920–29; discussion 929–31, Nov 2006.
- [197] C. Zhang and T. Chen. An active learning framework for content-based information retrieval. *Multimedia, IEEE Transactions on*, 4(2):260–268, 2002.
- [198] Y. Zhang, M. Brady, and S. Smith. Segmentation of brain MR images through a Hidden Markov Random Field model and the Expectation-Maximization algorithm. *IEEE Trans. Med. Imaging*, 20(1):45–57, Jan 2001.
- [199] SC Zhu and A Yuille. Region competition: Unifying snakes, region growing, and Bayes/MDL for multiband image segmentation. *IEEE Transactions On Pattern Analysis And Machine Intelligence*, 18(9):884–900, SEP 1996.
- [200] X. Zhu. Semi-supervised learning literature survey. 2005.
- [201] Yang-Ming Zhu and Steven M. Cochoff. An object-oriented framework for medical image registration, fusion, and visualization. *Computer Methods and Programs in Biomedicine*, 82(3):258 – 267, 2006.
- [202] F. Zhuge, G. D. Rubin, S. H. Sun, and S. Napel. An abdominal aortic aneurysm segmentation method: Level set with region and statistical information. *Medical Physics*, 33(5):1440–1453, 2006.
- [203] M.H. Zweig and G. Campbell. Receiver-operating characteristic (roc) plots: a fundamental evaluation tool in clinical medicine. *Clinical chemistry*, 39(4):561–577, 1993.